

**DEVELOPMENT OF FLEXIBLE  
PIEZOELECTRIC NANOGENERATORS  
FROM ELECTROSPUN NANOFABRICS OF  
POLY(VINYLDENE  
FLUORIDE)/NANOSHEETS COMPOSITES**

Thesis

Submitted in partial fulfillment of the requirements for the degree of

DOCTOR OF PHILOSOPHY

By

**SAWAN SHETTY**



DEPARTMENT OF METALLURGICAL AND MATERIALS  
ENGINEERING  
NATIONAL INSTITUTE OF TECHNOLOGY KARNATAKA,  
SURATHKAL, MANGALURU – 575025

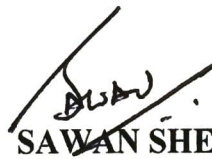
December, 2021



## DECLARATION

*By the Ph.D. Research Scholar*

I hereby *declare* that the Research Thesis titled “**Development of Flexible Piezoelectric Nanogenerators from Electrospun Nanofabrics of Poly(vinylidene fluoride)/Nanosheets Composites**”, which is being submitted to the **National Institute of Technology Karnataka, Surathkal** in partial fulfillment of the requirements for the award of the Degree of **Doctor of Philosophy in Metallurgical and Materials Engineering** is a *bonafide report of the research work carried out by me*. The material contained in this Research Thesis has not been submitted to any University or Institution for the award of any degree.



**SAWAN SHETTY**

Register number: 165023MT16F06

Department of Metallurgical and Materials Engineering  
National Institute of Technology Karnataka, Surathkal

Place: NITK-Surathkal

Date: 03/01/2022

## CERTIFICATE

This is to *certify* that the Research Thesis titled “**Development of Flexible Piezoelectric Nanogenerators from Electrospun Nanofabrics of Poly(vinylidene fluoride)/Nanosheets Composites**”, submitted by **Sawan Shetty** (Register No: **165023MT16F06**) as the record of the research work carried out by him, is *accepted as the Research Thesis submission* in partial fulfillment of the requirements for the award of degree of **Doctor of Philosophy**.



**Prof. S. ANANDHAN, PhD, FIE**  
Department of Metallurgical & Materials Engineering  
National Institute of Technology Karnataka, Surathkal  
Post Srinivasnagar, Mangaluru - 575 025, KA, India

*S. Anandhan*  
03/01/2022

**Prof. S. Anandhan**

Research guide

(Signature with date and seal)

*K. Narayan Prabhu*

**Prof. K. Narayan Prabhu**

Chairman-DRPC

(Signature with date and seal)

Chairman - DRPC  
Dept. of Metallurgical and Materials Engineering  
National Institute of Technology Karnataka, Surathkal  
Post Srinivasnagar, Mangaluru - 575 025  
Karnataka, India

*Dedicated to my beloved parents, my caring wife, and my  
adorable son.*



## ACKNOWLEDGEMENT

---

I am genuinely grateful to my mentor, my guru Prof. Anandhan Srinivasan, Department of Metallurgical and Materials Engineering, NITK, for accepting me as his student and providing me the opportunity to pursue my doctoral studies. Completing this work would not have been possible without his invaluable advice, patience, constant support, and encouragement throughout the research work. His zeal for research with conviction has always encouraged me to widen my research perspectives. I sincerely thank him for his blessings and well wishes and shall be indebted to him for a lifetime. My gratitude also extends to his family members for their affection and well wishes.

I sincerely thank my Research Progress Assessment Committee members, Dr. Saumen Mandal, Department of Metallurgical and Materials Engineering, NITK, and Dr. Mritunjay Doddamani, Department of Mechanical Engineering, NITK, for their valuable time, insightful comments, and encouragement throughout the research work.

I am pleased to thank Dr. Arunjunairaj Mahendran, Kompetenzzentrum Holz GmbH, Austria, Prof. A. M. Shanmugharaj (VISTAS, Chennai), Dr. M. Selvakumar, Department of Metallurgical and Materials Engineering, NITK, Prof. M. N. Satyanarayan, Department of Physics, NITK, Prof. Gangadharan K V, Department of Mechanical Engineering, NITK, Prof. K. N. Prabhu, Prof. Udaya Bhat, and Dr. M. R. Rahman, Department of Metallurgical and Materials Engineering, NITK, for their valuable aid in the different stages of my research work. I also thank the Department of Metallurgical and Materials Engineering faculty for their direct/indirect support throughout my research work.

I thank Mrs. U. Rashmi, Mr. Prajwal, Mr. Achyutha K, Mr. Susheel Kumar N, Mr. Praveen Shenoy, Mr. Nandana M, Mr. Augustine S, and Mr. Vijay Mistari for their kind assistance in various characterization techniques. I would also appreciate and thank Central Instrumentation Facility-MIT Manipal, SOLVE: The virtual lab at NITK Surathkal, CeNSE IISc Bangalore, KONSPEC-Mangaluru, BIO-AFM (BSBE) - IRCC BIO Atomic Force Microscopy (BIO-AFM) Central Facility of I.I.T. Bombay, Central Research Facility at NITK Surathkal and Pneumatics lab-Department of

Mechatronics Engineering, MIT Manipal for providing with the assistance and facility for various characterization techniques.

I also appreciate and thank the technicians and non-teaching staff in the Department of Metallurgical and Materials Engineering, NITK, for their kind support, particularly Mrs. Sharmila Dinesh, Mrs. Vinaya D, and Mr. Sundara Shettigar.

I extend heartfelt gratitude to my fellow labmates, Dr. B. Sachin Kumar, Dr. Mohammed Khalifa, Dr. Shamitha C, Mr. Govind Ekbote, Mr. Anuj Ashok, and Mr. Harsha Patil for their assistance, encouragement, and cooperation during my research work.

Special thanks are due to Late. Prof. Rammohan Pai, former Head, Department of Aero and Automobile Engineering, MIT Manipal, and Dr. Ramjee, former Director, Manipal University-Dubai campus, for their constant support and encouragement.

I sincerely thank and acknowledge my friends for their overwhelmed support during the hard times: Mr. Laxmikant G Keni, Dr. Chethan K N, Mr. Sampath Suranjan Salins, Mr. Kevin Amith Mathias, Dr. Abdul Khader, Ms. Ashritha Salian, and Mr. Prajwal K.

Finally, I thank from the bottom of my heart to my family: my parents, my sisters, and my in-laws, for their continued encouragement, moral support, and valuable prayers. I am thankful to my wife, Nisha, and my son, Master Samay, for all their selfless sacrifices, love, and care that kept me going through this entire research journey.

**SAWAN SHETTY**



## ABSTRACT

---

Poly(vinylidene fluoride) (PVDF) is a versatile polymer due to its dielectric, piezoelectric and ferroelectric properties. However, a range of processing routes and/or additives is often necessary to enhance such properties. In this study, PVDF nanocomposite based electrospun nanofabrics were synthesized for piezoelectric energy-harvesting applications. Functional nanofillers such as organically modified Ni-Co layered double hydroxide (OLDH), talc nanosheets, and carboxyl functionalized graphene nanosheets (FGNS) were used to tune the electroactive  $\beta$ -phase of PVDF. Morphology, crystallinity, polymorphism, dielectric, and piezoelectric properties of these nanofabrics were studied in detail. The presence of these nanofillers in PVDF nanofabrics led to the enhancement of the polar  $\beta$ -phase in PVDF, which was corroborated from the results of Fourier transform infrared spectroscopy and X-ray diffraction. A nanogenerator, that was custom made from the OLDH/PVDF nanofabrics exhibited a maximum output voltage of 6.9 V and power density of  $0.92 \mu\text{W}/\text{cm}^2$  under human finger tapping mode. The synergistic effect of OLDH and electrospinning contributed to the enhancement of the  $\beta$ -phase content, thereby the piezoelectric response of the OLDH/PVDF composite nanofabrics. The electromechanical response of talc nanosheets/PVDF composite nanofibers was studied using piezoresponse force microscopy and accordingly exhibited well-defined ferroelectric characteristics with an enhanced piezoelectric coefficient ( $d_{33}$ ) of  $\sim 43.3$  pm/V compared to 10 pm/V measured for the pristine PVDF nanofibers. It was observed that the piezoelectric coefficient values strongly depended on the morphology and electroactive phase fraction of the ensuing composite nanofiber. Also, these talc nanosheets/PVDF composite nanofabrics recorded a maximum piezoelectric response of 9.1 V. Finally, the developed talc nanosheets/FGNS/PVDF hybrid composite nanofabrics resulted in an enhanced piezoelectric response of 12.9 V and  $\sim 61$  pm/V, respectively. The advantage of a high aspect ratio, surface charges, and electrically conductive network offered by nanofillers alongside the electrospinning augmented the composite nanofibers' piezoelectric response. Improved flexibility, mechanical robustness, and enhanced piezoelectric

responsiveness of these PVDF based composite nanofabrics could possibly pave the way to their use in flexible energy-harvesting devices.

**Keywords:** Electrospinning; poly(vinylidene fluoride); piezoelectric; composite; energy-harvesting.

# CONTENTS

---

|  |           |
|--|-----------|
| <b>CONTENTS</b>  |           |
| <b>LIST OF FIGURES</b>   | i         |
| <b>LIST OF TABLES</b>  | vii       |
| <b>NOMENCLATURE</b>  | ix        |
| <b>CHAPTER 1: INTRODUCTION AND LITERATURE REVIEW</b>                   | <b>1</b>  |
| 1.1 INTRODUCTION   | 1         |
| 1.1.1 Overview to Nanofibers   | 4         |
| 1.1.2 Polymorphism of PVDF   | 6         |
| 1.1.3 Electrospinning method and PVDF nanofabrics                      | 10        |
| 1.1.4 Electrospinning of PVDF based composite nanofabrics              | 15        |
| 1.1.4.1 Piezoelectric fillers  | 16        |
| 1.1.4.2 Conducting fillers   | 18        |
| 1.1.4.3 Non-conducting fillers   | 20        |
| 1.1.4.4 Hybrid fillers   | 21        |
| 1.2 PROBLEM IDENTIFICATION   | 27        |
| 1.3 SCOPE AND OBJECTIVES OF THE PRESENT WORK                           | 27        |
| 1.3.1 Scope  | 27        |
| 1.3.2 Objectives   | 27        |
| <b>CHAPTER 2: MATERIALS AND METHODS</b>                                | <b>31</b> |
| 2.1 MATERIALS  | 31        |
| 2.2 METHODS  | 31        |
| 2.2.1 Synthesis of organically modified Ni-Co layered double hydroxide | 31        |
| 2.2.2 Electrospinning of OLDH/PVDF composite nanofabrics               | 32        |
| 2.2.3 Electrospinning of talc nanosheets/PVDF composite nanofabrics    | 32        |
| 2.2.4 Synthesis of graphene oxide and reduced graphene oxide           | 33        |
| 2.2.5 Synthesis of carboxyl functionalized graphene nanosheets         | 33        |
| 2.2.6 Electrospinning of PVDF and 0.50 wt% talc                        | 34        |

|   |           |
|---|-----------|
| nanosheets/FGNS/PVDF (TGP)-based composite nanofabrics  |           |
| 2.3 MEASUREMENT AND CHARACTERIZATION  | 35        |
| 2.3.1 Setups and methodology used for piezoelectric performance evaluation of PVDF-based composite nanofabrics  | 37        |
| <b>CHAPTER 3: ORGANO-MODIFIED Ni-Co LDH: ON THE POLYMORPHISM, DIELECTRIC, AND PIEZOELECTRIC RESPONSE OF ELECTROSPUN POLY(VINYLIDENE FLUORIDE) NANOFABRICS</b> | <b>41</b> |
| 3.1 RESULTS AND DISCUSSION  | 41        |
| 3.1.1 Characterization of OLDH  | 41        |
| 3.1.2 Characterization of OLDH/PVDF composite nanofabrics   | 43        |
| 3.1.2.1 SEM, EDS and TEM results  | 43        |
| 3.1.2.2 XRD results   | 45        |
| 3.1.2.3 DSC results   | 46        |
| 3.1.2.4 FTIR spectroscopy   | 48        |
| 3.1.2.5 Dielectric properties   | 50        |
| 3.1.2.6 Piezoelectric performance   | 51        |
| 3.2 SUMMARY AND CONCLUSIONS   | 53        |
| <b>CHAPTER 4: DEVELOPMENT OF A NEW FLEXIBLE NANOGENERATOR FROM ELECTROSPUN NANOFABRIC BASED ON PVDF/TALC NANOSHEET COMPOSITES</b>                             | <b>55</b> |
| 4.1 RESULTS AND DISCUSSION  | 55        |
| 4.1.1 Morphology  | 55        |
| 4.1.2 XRD analysis  | 58        |
| 4.1.3 FTIR analysis   | 59        |
| 4.1.4 TGA analysis  | 61        |
| 4.1.5 DSC analysis  | 62        |
| 4.1.6 Tensile properties  | 63        |
| 4.1.7 Piezoelectric evaluation  | 64        |
| 4.2 SUMMARY AND CONCLUSIONS   | 67        |

|   |            |
|---|------------|
| <b>CHAPTER 5: NANOSCALE MAPPING OF DOMAIN SWITCHING AND PIEZOELECTRIC COEFFICIENT OF TALC NANOSHEETS INCORPORATED PVDF NANOFIBERS BY PIEZORESPONSE FORCE MICROSCOPY</b> | <b>69</b>  |
| 5.1 RESULTS AND DISCUSSION  | 69         |
| 5.1.1 PFM analysis  | 69         |
| 5.2 SUMMARY AND CONCLUSIONS   | 73         |
| <b>CHAPTER 6: PIEZOELECTRIC EVALUATION OF FLEXIBLE NANOGENERATOR BASED ON ELECTROSPUN PVDF/FUNCTIONALIZED GRAPHENE/TALC NANOSHEETS HYBRID NANOCOMPOSITES</b>            | <b>77</b>  |
| 6.1 RESULTS AND DISCUSSION  | 77         |
| 6.1.1 Characterization of carboxyl functionalized graphene nanosheets   | 77         |
| 6.1.2 Characterization of TGP-based hybrid composite nanofabrics  | 82         |
| 6.1.2.1 FESEM results   | 82         |
| 6.1.2.2 XRD results   | 84         |
| 6.1.2.3 FTIR results  | 85         |
| 6.1.2.4 DSC results   | 88         |
| 6.1.2.5 Tensile testing results   | 89         |
| 6.1.2.6 Piezoelectric measurements  | 90         |
| 6.1.2.7 PFM results   | 93         |
| 6.2 SUMMARY AND CONCLUSIONS   | 96         |
| <b>CHAPTER 7: SUMMARY AND CONCLUSIONS</b>   | <b>99</b>  |
| <b>SCOPE FOR FURTHER STUDY</b>  | <b>101</b> |
| <b>APPENDIX-I</b>   | <b>103</b> |
| <b>REFERENCES</b>   | <b>111</b> |
| <b>BIO-DATA</b>   | <b>133</b> |
| List of Publications Based on PhD Research Work   | 135        |



## LIST OF FIGURES

---

| <b>Figure No.</b> | <b>Captions</b>   | <b>Page No.</b> |
|-------------------|---|-----------------|
| 1.1               | Orientation of dipoles; a) before, b) during, and c) after the poling process.  | 3               |
| 1.2               | Piezoelectric material configurations in $d_{31}$ -mode and $d_{33}$ -mode.   | 3               |
| 1.3               | Applications of nanofiber technology.   | 5               |
| 1.4               | Graphical representations of primary polymorphs of PVDF: $\alpha$ -phase, $\beta$ -phase, and $\gamma$ -phase.  | 8               |
| 1.5               | Schematic illustration of the process used to produce electroactive PVDF films.   | 10              |
| 1.6               | Schematic illustration of the electrospinning setup with an SEM image of the nanofibrous mat.   | 11              |
| 1.7               | Plausible interaction mechanism between various fillers and PVDF matrix, thereby facilitating the $\beta$ -phase conformation in electrospun PVDF composite nanofabrics.                            | 23              |
| 2.1               | Schematic depicting the synthesis of GO, RGO, and FGNS.   | 34              |
| 2.2               | Schematic demonstrating the construction, and photographic image of the nanogenerator.  | 38              |
| 2.3               | Illustration of piezoelectric evaluation of E-PVDF and talc/PVDF fabrics based nanogenerator by frequency modulated-shaker mode; (a) Schematic, and (b) Photographic image of the set-up.           | 39              |
| 2.4               | Schematic of piezoelectric response evaluation for electrospun nanofabrics based nanogenerator by pneumatic-actuator mode.  | 40              |
| 3.1               | XRD pattern of: a) LDH, and b) OLDH; c) FTIR spectra of LDH and OLDH.   | 42              |
| 3.2               | SEM micrograph of: a) LDH, and b) OLDH; c) TEM micrograph of OLDH.  | 43              |
| 3.3               | SEM micrographs of electrospun OLDH/PVDF nanofabrics with varying OLDH content: (a) 0%, (b) 1%, (c) 3%, (d) 5%, (e) 7% and (f) distribution of fiber diameters of E-PVDF and OLDH/PVDF nanofabrics. | 44              |

## LIST OF FIGURES

|      |  |    |
|------|--|----|
| 3.4  | SEM-EDS elemental mapping of Ni and Co in 3wt% OLDH/PVDF nanofabrics.  | 45 |
| 3.5  | TEM images of single nanofiber of: a) E-PVDF, and b) 3 wt% OLDH/PVDF composite.  | 45 |
| 3.6  | XRD patterns of PVDF powder, E-PVDF and OLDH/PVDF nanofabrics.   | 46 |
| 3.7  | DSC traces of E-PVDF and OLDH/PVDF nanofabrics.  | 47 |
| 3.8  | FTIR spectra of PVDF powder, E-PVDF, and OLDH/PVDF nanofabrics.  | 48 |
| 3.9  | FTIR spectra of electrospun PVDF and 3 wt% OLDH/PVDF nanofabrics.  | 49 |
| 3.10 | Schematic illustration of probable interactions between OLDH and PVDF in the composite nanofabrics.  | 50 |
| 3.11 | Frequency-dependent a) dielectric constant, and b) dielectric loss of E-PVDF and OLDH/PVDF nanofabrics.  | 51 |
| 3.12 | a) Variation of the piezoelectric response of E-PVDF and OLDH/PVDF nanofabrics based NG; b) The output voltage as a function of OLDH content in OLDH/PVDF nanofabrics.   | 52 |
| 3.13 | Switching polarity evaluation for 3 wt% OLDH/PVDF nanofabrics a) forward connection, and b) reverse connection.  | 52 |
| 3.14 | a) The output voltage and current, and b) calculated power density of 3 wt% OLDH/PVDF nanofabrics based NG across the different load resistance.   | 53 |
| 4.1  | SEM micrographs of the electrospun talc/PVDF composite nanofabrics: (a) without, (b) with 0.25 wt.%, (c) with 0.50 wt.% , (d) with 0.75 wt%, and (e) with 1 wt% addition of talc in PVDF matrix ; (f) SEM micrograph of talc nanoparticles, with yellow arrows indicating the talc layers. | 56 |
| 4.2  | (a) TEM image of 0.50 wt% talc/PVDF single nanofiber; (b) magnified TEM image of talc nanoparticle with d-value, and (c) SAED pattern of the 0.50 wt% talc/PVDF single nanofiber.  | 57 |
| 4.3  | SEM micrograph and EDS elemental mapping of 0.50 wt% talc/PVDF composite nanofabrics demonstrating the distribution of carbon (C), oxygen (O), silicon (Si), fluorine (F), and magnesium (Mg) elements in the PVDF matrix.   | 57 |



## LIST OF FIGURES

|      |   |    |
|------|---|----|
| 4.4  | XRD patterns corresponding to (a) E-PVDF, (b) 0.25 wt% talc/PVDF, (c) 0.50 wt% talc/PVDF, (d) 0.75 wt% talc/PVDF, and (e) 1 wt% talc/PVDF composite nanofabrics.  | 58 |
| 4.5  | FTIR spectra of E-PVDF and talc/PVDF composite nanofabrics.   | 59 |
| 4.6  | FTIR spectra of E-PVDF, talc, and 0.50 wt% talc/PVDF composite nanofabrics with yellow shades indicating the possible interactions between talc and PVDF chains.  | 60 |
| 4.7  | Proposed interacting mechanism in the talc/PVDF composite nanofabric.   | 61 |
| 4.8  | (a) TGA traces; and (b) DTG plots of E-PVDF and talc/PVDF composite nanofabrics.  | 62 |
| 4.9  | DSC traces of E-PVDF and talc/PVDF composite nanofabrics: (a) first cooling cycle, (b) second heating cycle.  | 63 |
| 4.10 | (a) Tensile stress-strain curve; and (b) Tensile strength, and Young's modulus as a function of talc loading in the PVDF matrix.  | 64 |
| 4.11 | The output voltage of nanogenerator under repetitive finger imparting: (a) E-PVDF and talc/PVDF composite nanofabrics, and (b) maximum output voltage as function of talc loading in the composite nanofabrics; (c) power density of 0.50 wt% talc/PVDF fabrics across varying load resistance. | 66 |
| 4.12 | The output voltage: (a) 0.50 wt% talc/PVDF based nanogenerator at varying vibrating frequency; (b) E-PVDF and talc/PVDF composite based nanogenerator at 30 Hz vibrating frequency.   | 67 |
| 5.1  | PFM images of pristine PVDF nanofiber: (a) 3-D topography image, (b) 2-D topography with the height cross-section profile, (c) amplitude image, (d) phase-1 image (trace), and (e) phase-2 image (retrace).   | 70 |
| 5.2  | PFM images of talc nanosheets/PVDF-0.50 nanofiber: (a) 3-D topography image, (b) 2-D topography with the height cross-section profile, (c) amplitude image, (d) phase-1 image (trace), and (e) phase-2 image (retrace).   | 70 |
| 5.3  | Amplitude and phase hysteresis loops of (a) PVDF nanofiber and (b) talc nanosheets/PVDF-0.50 nanofiber.   | 71 |
| 5.4  | PFM amplitude loops of (a) talc nanosheets/PVDF-0.25, (b) talc  | 73 |

## LIST OF FIGURES

|      |   |    |
|------|---|----|
|      | nanosheets/PVDF-0.75, and (c) talc nanosheets/PVDF-1 nanofibers.  |    |
| 6.1  | FTIR spectra of GO, RGO, and FGNS.  | 78 |
| 6.2  | XRD patterns of GO, RGO, and FGNS.  | 79 |
| 6.3  | Raman spectra of RGO, and FGNS.   | 80 |
| 6.4  | FESEM images: a) RGO and b) FGNS.   | 81 |
| 6.5  | Microstructure analysis of FGNS : (a, b) TEM images with yellow arrows indicating the wrinkled structure, (c) SAED pattern, and (d) d-space value from TEM image.   | 81 |
| 6.6  | FESEM micrographs of electrospun nanofabrics: a) E-PVDF; b) TGP-0.05; c) TGP-0.10; d) TGP-0.15; e) TGP-0.20; f) high magnification FESEM image of TGP-0.20.   | 83 |
| 6.7  | EDS elemental mapping of TGP-0.10 nanofabrics: (a) overlay distributions of elements, (b) distribution of carbon, (c) distribution of oxygen, (d) distribution of fluorine, (e) distribution of magnesium, and (f) distribution of silicon.   | 83 |
| 6.8  | XRD patterns of E-PVDF and TGP-based nanofabrics.   | 84 |
| 6.9  | FTIR spectra of E-PVDF and TGP-based nanofabrics in the wavenumber range of a) 2000-650 $\text{cm}^{-1}$ , b) 920-800 $\text{cm}^{-1}$ , c) 1250-1080 $\text{cm}^{-1}$ , and d) 3100-2900 $\text{cm}^{-1}$ .                                  | 86 |
| 6.10 | Schematic illustration of plausible interactions between hybrid fillers and PVDF.   | 87 |
| 6.11 | DSC traces of E-PVDF and TGP-based fabrics: (a) Cooling cycle; and (b) Heating cycle.   | 88 |
| 6.12 | Tensile stress-strain plots of E-PVDF and TGP-based nanofabrics.  | 90 |
| 6.13 | a) The output voltage generated from E-PVDF and TGP-based nanofabrics under impact by pneumatic actuator mode, b) switching polarity sequence test of TGP-0.10 nanofabrics with inset displaying magnified impacting and releasing responses. | 91 |
| 6.14 | a) Working mechanism of the nanogenerator under impact and release mode; b) generated output voltage and power density as a function of varying load resistance from a TGP-0.10 based nanogenerator.  | 92 |

## LIST OF FIGURES

- 6.15 PFM analysis of TGP-0.10: (a) topography image, (b) amplitude image, (c) 94  
phase image, (d) amplitude loop, and (e) phase loop.
- 6.16 PFM amplitude loops of a) TGP-0.05, b) TGP-0.15, and c) TGP-0.20 94  
based nanofibers.

## LIST OF FIGURES

## LIST OF TABLES

---

| <b>Table No.</b> | <b>Captions</b>  | <b>Page No.</b> |
|------------------|--|-----------------|
| 1.1              | Piezoelectric coefficients of various piezoelectric materials.   | 4               |
| 1.2              | Comparison of various nanofiber fabrication techniques.  | 6               |
| 1.3              | Influence of various fillers/additives on the piezoelectric performance of electrospun PVDF based composite nanofabrics.   | 24              |
| 3.1              | MFD and SD of OLDH/PVDF nanofabrics with different contents of OLDH.   | 44              |
| 3.2              | Melting temperature, melting enthalpy, and crystallinity of E-PVDF and OLDH/PVDF nanofabrics.  | 47              |
| 3.3              | FTIR results of OLDH/PVDF nanofabrics with different content of OLDH.  | 49              |
| 4.1              | % $\beta$ -phase content, crystallization temperatures, and melting temperatures of E-PVDF and talc/PVDF composite nanofabrics.  | 63              |
| 6.1              | $\beta$ -phase fraction, crystallization temperature, melting temperature, degree of crystallinity, tensile strength, and Young's modulus of the E-PVDF and TGP-based nanofabrics. | 90              |



## NOMENCLATURE

---

|                                    |   |
|------------------------------------|---|
| $\theta$                           | Theta                                       |
| $\lambda$                          | Wavelength                                  |
| %                                  | Percentage                                  |
| $\chi_c$                           | Degree of crystallinity                     |
| °                                  | Degree                                      |
| °C                                 | Degree Celsius                              |
| Å                                  | Angstrom                                    |
| AFM                                | Atomic force microscopy                     |
| AC                                 | Alternating current                         |
| Ag                                 | Silver                                      |
| Au                                 | Gold  |
| BaTiO <sub>3</sub>                 | Barium titanate                             |
| cm                                 | Centimeter                                  |
| CNT                                | Carbon nanotube                             |
| CuK <sub><math>\alpha</math></sub> | Copper k-alpha                              |
| D                                  | Dimensional                                 |
| DC                                 | Direct current                              |
| DDAC                               | Diocetadecyl dimethyl ammonium chloride     |
| DMAc                               | Dimethylacetamide                           |
| DMF                                | N,N-dimethylformamide                       |
| DMSO                               | Dimethyl sulfoxide                          |
| DSC                                | Differential scanning calorimetry           |
| DTG                                | Derivative Thermogravimetric analysis       |
| EHS                                | Energy harvesting systems                   |
| EDS                                | Energy dispersive x-ray spectroscopy        |
| eV                                 | Electron volt                               |
| FGNS                               | Carboxyl functionalized graphene nanosheets |
| FESEM                              | Field Emission Scanning Electron Microscopy |
| FTIR                               | Fourier transform infrared spectroscopy     |

## NOMENCLATURE

|             |   |
|-------------|---|
| g           | Gram  |
| GO          | Graphene oxide                                      |
| h           | Hour  |
| HNT         | Halloysite nanotubes                                |
| ICDD        | International Centre for Diffraction Data           |
| KNN         | Potassium sodium niobate                            |
| KOH         | Potassium hydroxide                                 |
| kV          | Kilovolt  |
| kHz         | Kilo hertz  |
| LDH         | Layered double hydroxide                            |
| LiCl        | Lithium chloride                                    |
| MWCNT       | Multi-walled carbon nanotubes                       |
| MPa         | Megapascal  |
| MFD         | Mean Fiber Diameter                                 |
| m           | Meter   |
| mmol        | Millimole   |
| $\bar{M}_w$ | Weight average molecular weight                     |
| min         | Minute  |
| mL          | Milliliter  |
| mm          | Millimeter  |
| mV          | Millivolt   |
| mW          | Milliwatt   |
| NaOH        | Sodium hydroxide                                    |
| nm          | Nanometer   |
| N           | Newton  |
| OMMT        | Montmorillonite                                     |
| OLDH        | Organically modified Ni-Co layered double hydroxide |
| PZT         | Lead zirconate titanate                             |
| pC/N        | Picocoulombs per newton                             |
| pm/V        | Picometer per volt                                  |



## NOMENCLATURE

|         |                                    |
|---------|------------------------------------|
| PE      | Poly(ethylene)                     |
| PTFE    | Poly(tetrafluoroethylene)          |
| PMMA    | Poly(methyl methacrylate)          |
| PVA     | Poly(vinyl alcohol)                |
| PANi    | Poly(aniline)                      |
| PBO     | Poly(benzoxazole)                  |
| PVDF    | Poly(vinylidene fluoride)          |
| Pt      | Platinum                           |
| RGO     | Reduced graphene oxide             |
| rpm     | Revolutions per minute             |
| s       | Second                             |
| SAED    | Selected area electron diffraction |
| SD      | Standard deviation                 |
| SDBS    | Sodium dodecyl benzene sulphonate  |
| SEM     | Scanning Electron Microscopy       |
| $T_c$   | Crystallization temperature        |
| TEM     | Transmission Electron Microscopy   |
| $TiO_2$ | Titanium dioxide                   |
| TGA     | Thermogravimetric analysis         |
| $T_m$   | Melting temperature                |
| THF     | Tetrahydrofuran                    |
| V       | Volt                               |
| wt%     | Weight percentage                  |
| wt/v%   | Weight by volume percent           |
| W       | Watt                               |
| XRD     | X-ray diffraction                  |
| ZnO     | Zinc oxide                         |
| $ZrO_2$ | Zirconium dioxide                  |



# CHAPTER 1

---

The contents of this chapter have been published in *Nano Tools & Devices for Enhanced Renewable Energy*, Ch.10, ISBN: 9780128217092, Elsevier, UK, 2021.



# CHAPTER I

## INTRODUCTION AND LITERATURE REVIEW

---

*This chapter briefly introduces poly(vinylidene fluoride)(PVDF) based composite nanofabrics and their applicability as a piezoelectric energy harvester. An overview of piezoelectric materials, nanofibers, electrospinning process, and PVDF has been presented. A brief literature review focusing on flexible piezoelectric energy harvesting system based on PVDF composite nanofabrics, with emphasis on tuning the electroactive properties of the composite nanofabrics is explored. Finally, the problem identification, scope, and objectives of the present work are discussed.*

### 1.1 INTRODUCTION

The alarming energy crisis and its adverse pollution effects have led to the focus on the dependence of a cleaner source of energy (green energy). Various renewable energies such as solar, wind, tidal, and geothermal have been exploited to meet the energy demands of human civilization to some extent. However, with the rapid development of science and technology, especially with the advent of the internet of things (IOT), energy harvesting systems (EHS) have been gaining popularity in recent times. EHS produce a relatively low level of power in the range of nano-watt to milli-watts catering to the demands of low powered sensors, actuators, and wireless transmitters [Wan and Bowen 2017; Zi and Wang 2017]. EHS derive their energy from various ambient sources such as thermal, chemical, biological, and mechanical. In particular, the energy derived from ambient mechanical source has been an attractive choice owing to its abundant availability in the surrounding environment, including human motions (walking, running, heartbeat, etc.), vibrations (machines, vehicle motions), and fluid flows [Yan et al. 2019]. Amongst the piezoelectric, electromagnetic, and electrostatic transduction mechanisms, the EHS based on the piezoelectric effect have gained popularity due to their higher energy density and simpler architecture with the ease of integrating with flexible micro/nanodevices [Li

et al. 2014; Liu et al. 2018]. A piezoelectric material generates electric polarization via an external mechanical stress/strain, termed as the direct piezoelectric effect, and finds its relevance in the functioning of sensor and energy transducer. Piezoelectric materials also undergo mechanical deformation under an external electric field, constituting to the converse piezoelectric effect [Kim et al. 2011]. The operation of actuators is based on the converse effect. The constitutive equations governing direct and converse piezoelectric effects are as follows.

$$S = s_{ij}^E T_j + d_{ki} E_k \quad (1)$$

$$D_i = d_{ij} T_j + \varepsilon_{ik}^T E_k \quad (2)$$

Where  $S$  and  $T$  are strain and stress, respectively;  $D$ ,  $E$ ,  $s$ ,  $d$ , and  $\varepsilon$  represent the electric displacement, electric field, elastic compliance, piezoelectric coefficient, and dielectric permittivity components, respectively; the superscripts  $E$  and  $T$  indicate the relevant constants measured at the constant electric field and constant stress, respectively; and the subscripts  $i$ ,  $j$ , and  $k$  refer to three spatial dimensions [Qi and McAlpine 2010].

The piezoelectric effect is usually displayed by non-centrosymmetric crystals due to displacement of ions leading to polarization [Troler-McKinstry et al. 2018]. In ferroelectric materials, which are a subset of piezoelectric, a process called poling (orientation of electrical dipoles) is induced below a critical temperature (Curie temperature) to make them piezo-active materials [Caliò et al. 2014]. Fig.1.1 shows the poling process of polycrystalline material, and the initial unpoled state consists of polar domains with random orientation (Fig.1.1a). A strong electric field just below the Curie temperature is provided to facilitate the orientation of polar domains with the external electric field (Fig.1.1b). Further, on cooling to ambient temperature following the removal of the external field, the material continues to maintain the orientation of polar domains (Fig.1.1c). In consequence, the material retains net polarization and hence exhibits the piezoelectric effect. In ferroelectric polymers such as Poly(vinylidene fluoride (PVDF) and its copolymers, the poling process is assisted with mechanical stretching of the polymer, thereby enhancing the molecular dipole alignment with the applied electric field. Thus, the piezoelectric effect is exhibited by

poled ferroelectric ceramics (barium titanate ( $\text{BaTiO}_3$ ), lead zirconate titanate (PZT)), and polymers [Mishra et al. 2019].

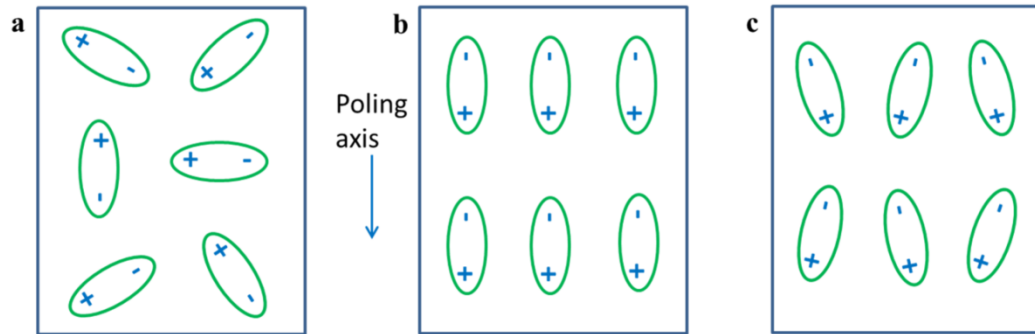


Fig.1.1 Orientation of dipoles; a) before, b) during, and c) after the poling process.

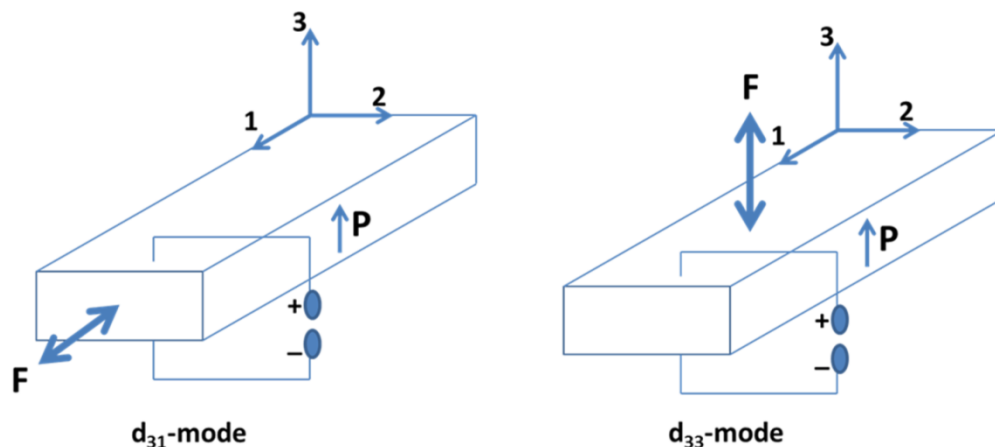


Fig.1.2 Piezoelectric material configurations in  $d_{31}$ -mode and  $d_{33}$ -mode.

The piezoelectric materials for EHS indicate a definite polar axis (3-direction/z-direction), and the representation of applied stress with reference to the polar axis resulting in two modes of configurations, namely  $d_{31}$ -mode and  $d_{33}$ -mode as shown in Fig.1.2. In  $d_{31}$ -mode, the polarization direction '3' is perpendicular to the direction of the applied stress/strain '1'. And in the  $d_{33}$ -mode, the polarization and application of stress/strain are in the same direction [Yang et al. 2018]. The piezoelectric coefficient ( $d_{3i}$ ) quantifies the piezoelectric performance of the material, i.e., the electric charge generated per unit applied force (unit of C/N). Amid the various piezoelectric materials in Table 1.1, PVDF and its copolymers have been the

choice for EHS in recent times. The notable flexibility, reduced density, eases of processing into fibers or films offered by PVDF, and its copolymers endow their benefits over the other piezoelectric materials with relatively higher  $d_{33}$  [Egusa et al. 2010; Kim et al. 2019].

Table 1.1 Piezoelectric coefficients of various piezoelectric materials.

| Material                             | $d_{33}$ (pC/N) | $d_{31}$ (pC/N) | References                 |
|--------------------------------------|-----------------|-----------------|----------------------------|
| Barium titanate ( $\text{BaTiO}_3$ ) | 350 to 500      | -185            | [Acosta et al. 2017]       |
| Lead zirconate titanate (PZT)        | 410             | -175            | [Schlaberg and Duffy 1994] |
| Zinc oxide (ZnO)                     | 12.4            | 5               | [Denishev 2016]            |
| Potassium sodium niobate (KNN)       | 80 to 120       | -32 to -43.4    | [Pavlič et al. 2014]       |
| PVDF                                 | -24 to -34      | 8 to 22         | [Mishra et al. 2019]       |

### 1.1.1 Overview to Nanofibers

Nanofibers are one-dimensional materials having a diameter less than 100 nm. Generally, fibers with a diameter below 1  $\mu\text{m}$  (1000 nm) and aspect ratio (length/diameter) larger than 100:1 are considered nanofibers. The word *fiber* comes from Latin *fibra*, and the prefix *nano* originates from the Greek word *nanos* or *nannos*, referring to “dwarf.” Nanometer measures billionth of a meter abbreviated as nm (1 nm =  $10^{-9}$  m). Nanotechnology deals with the study of occurrence and functions of matter ranging within the dimension 0.1-100 nm. The nanomaterials based on dimensions are classified as zero dimensional (0-D), having three directions of nanosymmetry ex:- quantum dots and nanoparticles; one-dimensional (1-D) having two directions of nanosymmetry, ex:-nanowires, nanorods, nanotubes, and nanofibers; and two-dimensional (2-D) have a platelet or sheet structure with a thickness of less than 100 nm ex:- nanoclays and graphene.

Nanofibers are produced from different materials such as natural and synthetic polymers, carbon-based, and composite nanomaterials. Due to the high specific



surface area, flexibility, and excellent directional strength, nanofibers are preferred for many potential applications, including energy generation and storage, water and environmental treatment, and healthcare and biomedical engineering (Fig. 1.3). Nanofibers can be fabricated by several techniques such as drawing, template synthesis, phase-separation, self-assembly, melt blowing, and electrospinning. A comparison of various nanofiber fabrication techniques is highlighted in Table 1.2.

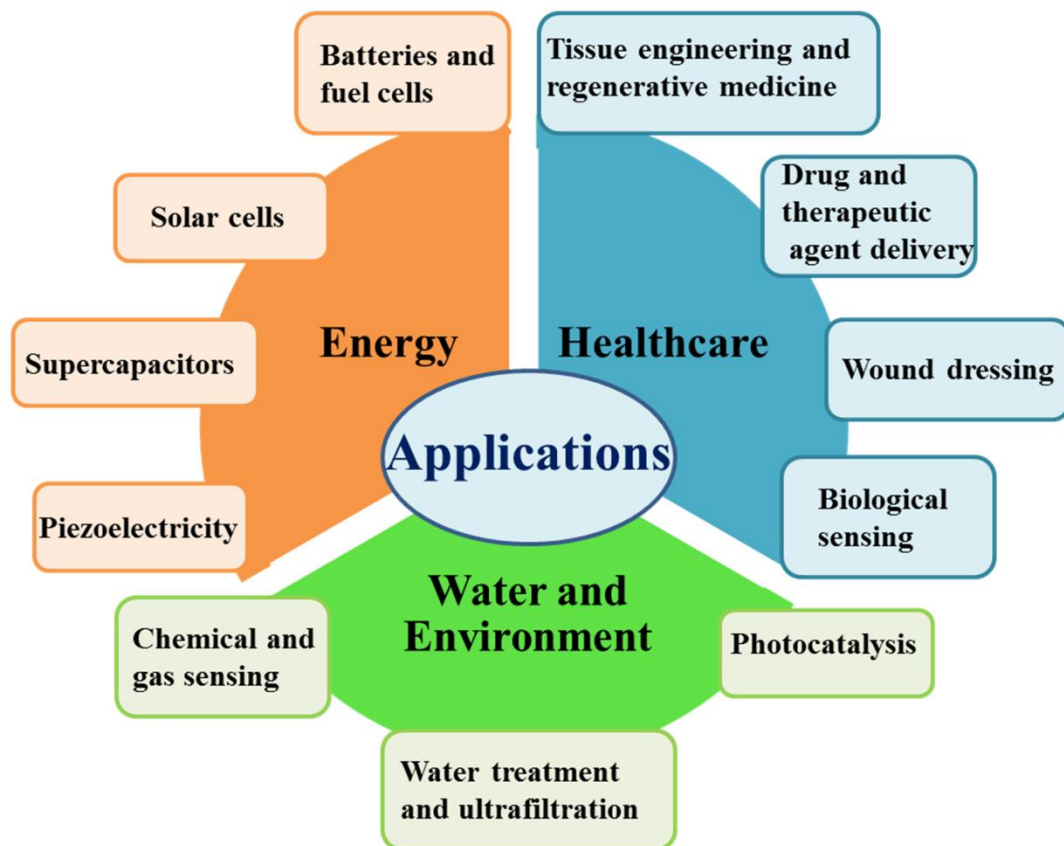


Fig.1.3 Applications of nanofiber technology (Kenry and Lim 2017).

Table 1.2 Comparison of various nanofiber fabrication techniques (Nayak et al. 2012).

| <b>Manufacturing process</b> | <b>Scope for scaling-up</b> | <b>Repeatability</b> | <b>Control on fiber dimension</b> | <b>Advantages</b>  | <b>Disadvantages</b>  |
|------------------------------|-----------------------------|----------------------|-----------------------------------|--|---|
| Drawing                      | No                          | Yes                  | No                                | Simple process   | Discontinuous process                                       |
| Template synthesis           | No                          | Yes                  | Yes                               | Easy to change diameter by using different templates                             | Complex process   |
| Phase separation             | No                          | Yes                  | No                                | Simple equipments required   | Only work with selective polymers                           |
| Self-assembly                | No                          | Yes                  | No                                | Easy to get smaller nanofibers   | Complex process   |
| Melt blowing                 | Yes                         | Yes                  | Yes                               | Long and continuous fibers, high productivity, free from solvent recovery issues | Polymer limitations, thermal degradation of polymers        |
| Forcespinning                | Yes                         | Yes                  | Yes                               | Free from very high voltage, eco-friendly  | Requirement of high temperature at times                    |
| Electrospinning              | Yes                         | Yes                  | Yes                               | Long and continuous fibers   | Thermal degradation of polymers, electric discharge problem |

### 1.1.2 Polymorphism of PVDF

The discovery of piezoelectric effect in ferroelectric polymers of the PVDF family triggered their importance as piezoelectric material for EHS. PVDF is a semi-crystalline fluoropolymer synthesized by polymerization of vinylidene fluoride. The

molecular structure of PVDF has repeating units of  $[-\text{CH}_2-\text{CF}_2-]$  and contains 59.4 wt% fluorine and 3 wt% hydrogen. The chemical structure of PVDF is intermediate of polyethylene (PE) ( $[-\text{CH}_2-\text{CH}_2-]_n-$ ) and polytetrafluoroethylene (PTFE) ( $[-\text{CF}_2-\text{CF}_2-]_n-$ ), thus displays high flexibility (near to PE) and thermal stability (comparable to PTFE). Due to these structural characteristics, PVDF can take different crystal forms depending on the sample preparation conditions.

PVDF has crystallinity of approximately 50% and exhibits well-defined polymorphs;  $\alpha$ ,  $\beta$ ,  $\gamma$ ,  $\delta$ , and  $\epsilon$  based on the chain conformation of *trans* (T) and *gauche* (G) linkages (Fig.1.4). The  $\alpha$ -phase is the dominant and stable one of PVDF, exhibiting distorted TGTG' conformation [Lovinger 1981; Lovinger 1982; Lovinger 1983]. The antiparallel arrangement of dipoles within the unit cell of  $\alpha$ -phase renders it nonpolar. The polymer chain in  $\beta$ -phase has all-trans (TTT) planar zigzag conformation with the dipole moments orientated in the same direction. Thus, the  $\beta$ -phase is polar in nature with the highest polarization per unit cell ( $8 \times 10^{-30}$  C m) [Martins et al. 2014]. The  $\gamma$ -phase has monoclinic unit cell with polar chain conformation of TTTGTTG', whilst the  $\delta$ -phase has polar TGTG' due to the inversion of dipole moments. The  $\epsilon$ -phase has a similar unit cell as that of the  $\gamma$ -phase with a chain conformation of TTTGTTG' with molecular chain packed in antiparallel, nonpolar crystal. Thus, to ensure higher piezoelectric response of PVDF, presence, and promotion of the polar  $\beta$ -phase is vital. Additionally, mechanical stretching and electrical poling are essential for immobilizing the polar phase. The polar  $\beta$ -phase formation in PVDF is favored by different techniques such as stretching of nonpolar  $\alpha$ -phase [Salimi and Yousefi 2003; Sencadas et al. 2009], solution casting [Karan et al. 2015], high voltage poling [Jiang et al. 2007; Lund and Hagström 2011], spin coating [Ramasundaram et al. 2008], electrospinning [Cozza et al. 2013; Jiyong et al. 2017], and by blending with fillers [Yu et al. 2009; Kar et al. 2015; Gong et al. 2018].

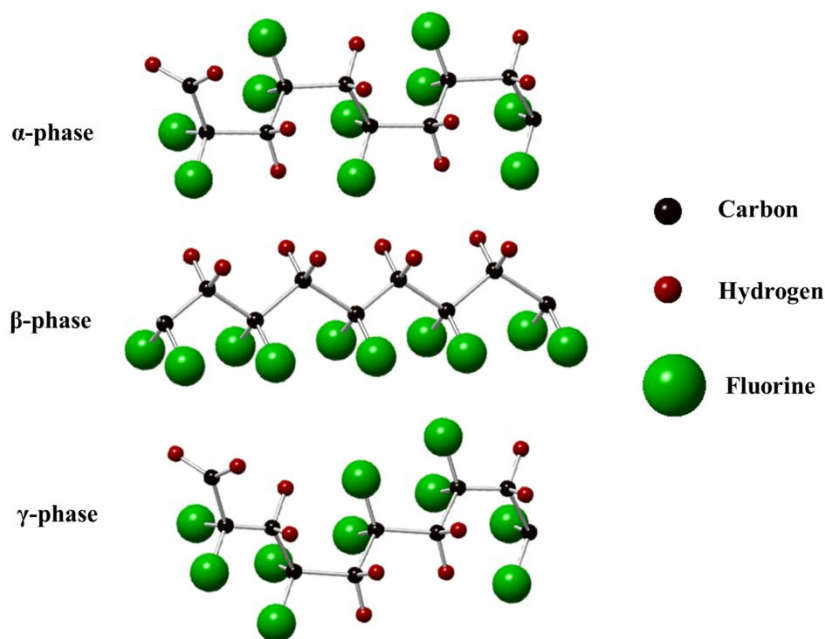


Figure 1.4 Graphical representations of primary polymorphs of PVDF:  $\alpha$ -phase,  $\beta$ -phase, and  $\gamma$ -phase.

The foremost common polymorph created amid crystallization from the melt is the  $\alpha$ -phase; it is the sole crystalline phase formed at all temperatures up to 150 °C. During crystallization from melt, the temperature and pressure are governing parameters that determine the final polymorphic phase of PVDF. A crystallization temperature in the range of 153 to 160 °C results in the transformation of  $\alpha$ - to  $\gamma$ -phase. However, the nucleation rate of  $\gamma$ -phase is lower than that of the  $\alpha$ -phase, and hence the latter phase dominates [Lovinger 1980]. Further, the  $\alpha$ -spherulites annealed above  $\sim 160$  °C favored the transformation to  $\gamma$ -phase, and the presence of block-copolymer surfactant further assisted the  $\gamma$ -phase formation [Prest and Luca 1978]. At 4 kbar, high-pressure annealing led to the  $\alpha$ - to  $\beta$ -phase transformation. This was attributed to the melting of  $\alpha$ -crystals (around 286 °C) that later recrystallizes to the  $\beta$ -phase of PVDF [Matsushige and Takemura 1978; Matsushige and Takemura 1980]. The solvent properties and evaporation temperature also contribute to the formation of different crystalline phases of PVDF. The crystallization of PVDF from polar solvents (DMF/DMSO/DMAc) always results in the formation of  $\beta$ -phase, provided the evaporation temperature is maintained  $< 70$  °C. However, temperature above 100 °C and 160 °C induces the formation of  $\alpha$ - and  $\gamma$ -phase, respectively [Gregorio, Jr. and

Cestari 1994; Yang et al. 2014]. The uniaxial or biaxial drawing of PVDF films at a lower temperature (below 90 °C) produces a molecularly orientated  $\beta$ -phase, while mechanical drawing at the temperature range of 140 °C to 150 °C retains the  $\alpha$ -phase conformation in the PVDF films due to the mobility of polymer chains at higher temperatures [McGrath and Ward 1980; Lovinger 1983]. The  $\alpha$ - to  $\beta$ -phase transformation is initiated moment the necking is observed in the stretched PVDF films. The necking indicates the transformation from a spherulitic structure to a micro-fibrillar one [Salimi and Yousefi 2003].

High electric fields can induce PVDF dipoles to orient along the applied field direction and thus facilitate the transformation of  $\alpha$ -phase to  $\beta$ - or  $\gamma$ -phase of PVDF. A higher electric field of the order of 4 MV/cm is essential for the  $\alpha$ - to  $\beta$ -phase transformation of PVDF, while the  $\gamma$ -phase transition occurs at lower electric field strengths [Davis et al. 1978; Naegele et al. 1978; Newman and Scheinbeim 1983]. The  $\alpha$ - to  $\beta$ -phase transformation induced by mechanical stretching of PVDF films can be further improved by the post electrical poling method (Fig.1.5) [Lovinger 1983; Sencadas et al. 2009]. Electrical poling also enhances the mechanical strength of PVDF films along the longitudinal direction due to the improved electromechanical coupling effect [Costa et al. 2008]. High energy irradiation has been able to induce crystal phase transformation in PVDF. Kosmynin and Gal'perin (1973) demonstrated the  $\alpha$ - to  $\beta$ -phase transition of PVDF using  $\gamma$ -irradiation  $\geq 500$  Mrad. Lately, the electrospinning process has been able to control the polymorphism of PVDF. The high voltage and stretching ratio experienced by electrospinning jet favor the nucleation of  $\beta$ -crystals. Also, the lower crystallization temperature arising from ambient operating conditions and faster evaporation of the solvent could promote the  $\beta$ -phase of PVDF [Zheng et al. 2007]. The spin-coating process has been demonstrated to produce PVDF thin films with an enhanced  $\beta$ -crystalline phase. The shear stress-induced elongation forces exerted on the polymer chains during the spin-coating process facilitate the all-trans conformation of the  $\beta$ -phase PVDF [Ramasundaram et al. 2008]. Further, the spin coating of PVDF solution containing hydrate salts boosted the electroactive  $\beta$ -phase content. This enhancement was attributed to the hydrogen bond formation between the water molecules of the salt and

fluorine atoms of PVDF [Benz et al. 2002; He and Yao 2006]. The high electric dipole moment of PVDF makes it miscible with several polar polymers. Thus PMMA and PVA have favored PVDF with enhanced  $\beta$ -phase owing to the dipole/dipole and hydrogen bond interactions between the PVDF matrix and blended polymer [Li et al. 2012; Na et al. 2012]. Also, polymorphism of PVDF can be controlled by the addition of fillers such as BaTiO<sub>3</sub> [Ye et al. 2013], Clay [Patro et al. 2008], metal salts CuO [Dutta et al. 2015], ZrO<sub>2</sub> [Li et al. 2010], Fe<sub>3</sub>O<sub>4</sub> [Jayakumar et al. 2013], metal nanoparticles such as Ag [Lopes et al. 2013], Au [Wang et al. 2011], Pt [Ghosh et al. 2015] and carbon nanotubes [Yu et al. 2009]. The nucleating effect of fillers on PVDF structure strongly relies on the morphology (shape, size), surface charges, dispersion, interfacial interactions, and processing conditions.

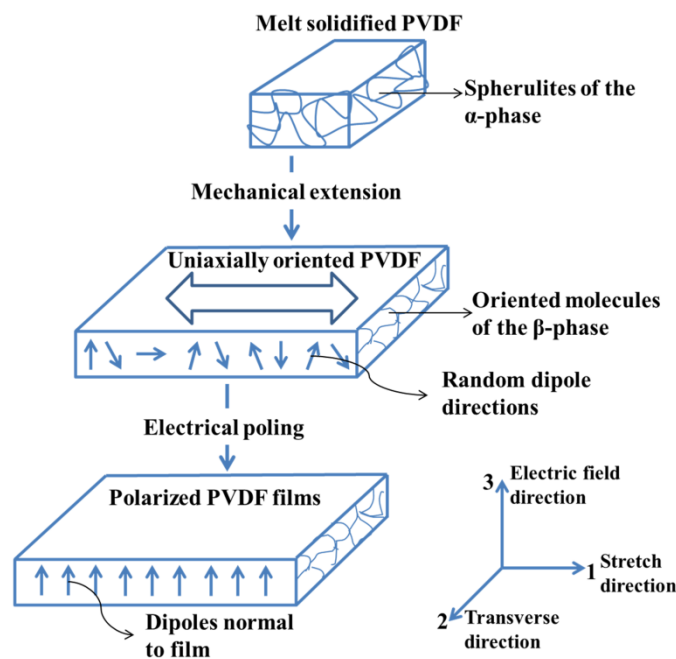


Fig.1.5 Schematic illustration of the process used to produce electroactive PVDF films [Lovinger 1983].

### 1.1.3 Electrospinning method and PVDF nanofabrics

Electrospinning is a simple and efficient method to fabricate one-dimensional nanomaterials from polymers, inorganic materials, and composites. This method uses electrostatic forces to produce ultrafine fibers with diameters ranging from a few tens of nanometers to micrometers. Electrospinning was first patented to produce fibers

from a polymer solution by Cooley and Morton in 1902 [Andrady 2009]. This process produces continuous fibers via an electrically charged jet of polymer solution/melt [Frenot and Chronakis 2003; Mirjalili and Zohoori 2016]. The electrospinning setup consists of three major components: a high voltage power supply, a spinneret, and a grounded metallic collector (flat plate/rotating drum type). The illustration of the electrospinning setup is shown in Fig.1.6.

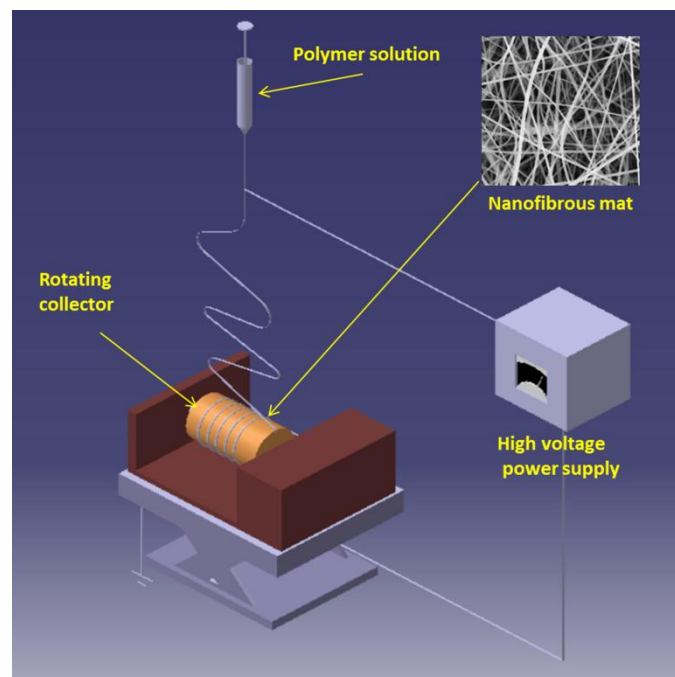


Fig.1.6 Schematic illustration of the electrospinning setup with an SEM image of the nanofibrous mat.

Nanofiber formation by electrospinning process is initiated when a polymer solution is introduced with a high electric field via a metallic needle of the spinneret. This induces free charges in the polymer solution and thereby forces it towards the grounded collector in response to the applied electric field. However, the surface tension resists the expulsion of polymer droplet at the spinneret tip, thereby leading to the elongation of the droplet in a conical shape, called Taylor cone [Taylor 1969]. At a critical voltage, the electrostatic force overcomes the surface tension of the polymer solution; thus, a jet of polymer ejected from the Taylor cone travels towards the collector. During its travel to the collector, the jet experiences rapid whipping and erratic motions resulting in ultrafine nanofibers. Moreover, as the jet travels, the

solvent evaporates, leaving behind the dry nanofibrous mat (Fig. 1.6, SEM image inset) on the collector.

Electrospun nanofibers with the desired diameter and bead-free morphology are achieved by controlling the governing parameters. These parameters are comprised of three parts: solution parameters (molecular weight, viscosity, conductivity, and surface tension), processing parameters (applied electric field, tip to collector distance and flow/feed rate), and ambient parameters (humidity and temperature).

Polymer concentration plays a significant role in deciding the electrospinnability of solution into nanofibers as it affects the chain entanglement. The spinning solution viscosity is directly proportional to the polymer concentration; thus, the solution viscosity increases with polymer concentration. Generally, at a low concentration, beads (electrospraying) are formed due to the influence of surface tension; while, higher concentration impedes fiber formation due to increased viscosity [Fong et al. 1999; Deitzel et al. 2001; Lin et al. 2010]. Above a particular critical entanglement concentration, the polymer chains prevent the breaking up of electrically driven jet initiated from the Taylor cone, thereby leading to bead-free uniform fiber morphology [McKee et al. 2004]. Notably, viscosity, polymer concentration, and molecular weight are related to each other. Electrical conductivity of the solution influences the charge carrying capacity of the electrospinning jet leading to subsequent stretching of the jet under the applied electric field. Thus, increasing the electrical conductivity of the solution contributes to the reduced fiber diameter of electrospun nanofibers [Bhardwaj and Kundu 2010; Angamma 2011].

The influence of applied voltage on the electrospun fiber diameter has varying effects. A few reports suggest a decrease in fiber diameter with increasing voltage, while others show the opposite trend [Zong et al. 2002; Yuan et al. 2004; Zhang et al. 2005]. However, the applied voltage influences the fiber diameter, but the level of significance varies with other governing parameters (e.g. solution concentration and tip to collector distance). The feed rate of the solution is another important parameter that influences electrospun fiber diameter and morphology. As the flow rate increases, beaded, thick nanofibers are formed due to insufficient drying time and low stretching



forces [Zuo et al. 2005]. Thus, a high voltage is preferred with a high flow rate to ensure; sufficient charge density and reduction in bead formation. The variation of a tip to collector distance directly influences the drying time and electric field strength. Whether shorter or longer, tip to collector distance results in thicker fibers with beaded morphology, due to the insufficient drying time and lesser stretching effect experienced by the nanofibers [Lee et al. 2004; Persano et al. 2013; Barua and Saha 2015]. Thus, an optimum tip to collector distance ensures desired fiber morphology. The type of collector influences the orientation of fibers; generally aligned fibers are obtained with rotating-type collector and randomly orientated fibers with a static-type collector [Matthews et al. 2002; Huang et al. 2003].

In addition, ambient conditions such as humidity and temperature also impact the diameter of electrospun nanofibers. An increase in temperature reduces the solution viscosity leading to reduced fiber diameter [Demir et al. 2002], while an increase in humidity leads to thicker fiber diameter due to polymer swelling [Rieger et al. 2013]. The electrospinning method offers distinctive properties such as larger surface area, higher aspect ratio, tunable porosity, simplicity, and a high degree of reproducibility. The aforementioned properties have led to its broader application in drug delivery, tissue engineering, wound healing, catalysis, filters, photoelectronics, magnetic devices, solar cells, etc. [Kenry and Lim 2017]. Recent studies demonstrate the one-step fabrication of piezoelectric fibers via electrospinning and its applicability in flexible energy harvesting devices. Additionally, the fibers can be incorporated with other functional materials to tune their specific property for applications ranging from sensors to advanced microelectronics [Mazinani et al. 2009].

In PVDF, the polar  $\beta$ -phase majorly contributes to its piezoelectric activity. Lately, the electrospinning technique has been reported to promote the formation of  $\beta$ -phase/ $\alpha$ - to  $\beta$ -phase transformation in PVDF nanofibers. The suggested mechanism favoring the  $\beta$ -phase is the one-step electrical poling and mechanical stretching effect induced by the electrospinning method. The electrospinning parameters, solvent type, and additives influence the  $\beta$ -phase content of PVDF nanofibers. For example, Ribeiro et al. (2010) investigated the influence of electrospinning parameters: flow rate, spinneret diameter, applied voltage, and rotating collector speed on the  $\beta$ -phase

content of PVDF nanofibers. In their study, spinneret diameter and rotating speed had a strong influence on the  $\beta$ -phase formation. This was attributed to the higher stretching of the jet or straining of the fibrils during the collection, thus, facilitating the ordering of polymer chains in the all-trans conformation. In most cases, dimethylformamide (DMF) and dimethylacetamide (DMAc) are the preferred solvents for electrospinning of PVDF. The evaporation rate of the solvent assists the elongation of the fibers, thereby straining the polymer chains to align in the all-trans polar  $\beta$ -phase conformation. In addition, acetone is also used to improve the evaporation rate of the solvent due to its volatile characteristics. Besides the solvent evaporation rate, the solvent polarity also plays a vital role in the crystal structure formation of the polymer. Evidently, the solvents with different polarities will influence the piezoelectricity of PVDF nanofibers. Shao et al. (2015) systematically investigated the electrospinning parameters on the fiber diameter,  $\beta$ -phase content, and mechanical to electrical energy conversion characteristics of PVDF nanofibers. It was observed that uniform nanofibers with smaller diameter exhibited higher  $\beta$ -phase content that led to their improved energy harvesting abilities. This is ascribed to the intensive stretching effect favoring the molecular conformation of the  $\beta$ -phase and, evaporation of the solvent ensures its retention in solidified fibers. Xue et al. (2017) studied the impact of dioctadecyl dimethyl ammonium chloride (DDAC) on the fiber morphology and  $\beta$ -phase content of PVDF nanofibers. The addition of DDAC improved the uniformity of nanofiber and enhanced the  $\beta$ -phase of nanofibers. This is attributed to the ionization and lubrication of DDAC that strengthened the stretching effect of fibers during electrospinning. The cooperative influence of DDAC and electrospinning led to the elimination of the  $\alpha$ -phase and subsequent enhancement in the  $\beta$ -phase fraction of PVDF nanofibers. Thus, electrospinning is an effective method to achieve  $\beta$ -phase of PVDF.

The piezoelectric property of PVDF relies on its electroactive phases, and the quantification of the same is vital for the application prospects. Therefore, scientific tools and characterization techniques are used to identify and evaluate the piezoelectric response of PVDF based nanofibers. X-ray diffraction (XRD), Fourier

transform infrared spectroscopy (FTIR), differential scanning calorimetry (DSC), and piezoresponse force microscopy (PFM) have been used.

PFM is a particular function in atomic force microscopy (AFM) that is designed to detect the piezoelectric response of the material. The principle of PFM is based on the converse piezoelectric effect, i.e., mechanical strain induced by the external electric field. The obtained PFM data reveals the phase angle, amplitude, ferroelectric polarization, and domain structure of the test sample. The measured amplitude is proportional to the piezoelectric coefficient, which quantifies the performance of the piezoelectric material. The phase angle represents the polarization direction, where  $0^\circ$  corresponds parallel (in-phase) and  $180^\circ$  antiparallel (out of phase) orientation of polarization to the PFM bias voltage. PFM is mostly suited for the analysis of single fiber in contrast to other characterization methods because it permits local piezoelectric measurements. For example, Baji et al. (2011) investigated the voltage induced deformation of PVDF fiber, and the results showed well defined piezoelectric and ferroelectric response of the fibers. PFM amplitude-voltage and phase-voltage loops displayed a characteristic butterfly loop and symmetric square-shape loop, which is associated with ferro/piezoelectric materials. The domain phase loop shows a  $180^\circ$  domain switching characteristics under the polarity reversal of the applied electric field, thus displaying the ferroelectric property of the PVDF. The maximum PFM amplitude of 1.2 nm was observed for an un-poled PVDF fiber, with a bias voltage of 45 V. Thus, the enhanced polar  $\beta$ -phase induced by electrospinning was able to influence the ferro/piezoelectric response in PVDF fibers.

#### **1.1.4 Electrospinning of PVDF based composite nanofabrics**

Electrospinning generally induces partial transformation of nonpolar  $\alpha$ -phase to polar  $\beta$ -phase of PVDF nanofabrics, thereby limiting its piezoelectric performance. The  $\beta$ -phase content in the electrospun PVDF nanofabrics can be improved by the incorporation of appropriate fillers within the spinning solution. PVDF, despite its flexibility, has a lower  $d_{33}$  value in comparison with the inorganic based piezoelectric materials. This limits the piezoelectric performance of the former to some extent. Recent studies demonstrate that the inclusion of inorganic piezoelectric materials into the PVDF matrix could improve the flexibility and piezoelectric performance of the

device. In addition, impregnation of conducting and hybrid fillers has also been able to contribute to the enhanced piezoelectric properties of PVDF based composites. The size, surface charges, and morphology of fillers play a prominent role in influencing the piezoelectric characteristics of polymer composites. Synergistic effects of various fillers and electrospinning with their underlying mechanism in tuning the polar phase of PVDF is discussed in this section.

#### **1.1.4.1 Piezoelectric fillers**

Piezoelectric fillers play a decisive role in altering the piezoelectric characteristics of PVDF based composite nanofabrics by imparting extra piezoelectric effect and also assist in the crystalline phase enhancement of PVDF. For example, Lee et al. (2016) demonstrated the energy harvesting capabilities of uniaxially-aligned barium titanate ( $\text{BaTiO}_3$ )/PVDF composites fabricated by electrospinning. The piezo-response of the composite nanofibers increased with the concentration of  $\text{BaTiO}_3$  nanoparticles. A loading of 16 wt%  $\text{BaTiO}_3$  nanoparticles in PVDF composite nanofibers resulted in a piezoelectric output voltage that was 1.7 times greater than that of virgin PVDF nanofibers under similar deformation conditions. The presence of  $\text{BaTiO}_3$  nanoparticles strengthened the piezoelectric response of PVDF nanofibers.

In 2019, Li et al. prepared a piezoelectric nanogenerator consisting of zinc oxide ( $\text{ZnO}$ )/PVDF nanocomposite membrane. The nanofillers of  $\text{ZnO}$  nanoparticles and  $\text{ZnO}$  nanorods were used in PVDF based nanocomposite membranes via electrospinning. They showed that loading of 5 wt% of  $\text{ZnO}$  nanorods in PVDF led to a relative  $\beta$ -fraction of 87.5%, and 30 wt %  $\text{ZnO}$  nanoparticles in PVDF resulted in  $\beta$ -fraction of 90.7%, respectively. Subsequently, the nanocomposite with 5 wt% of  $\text{ZnO}$  nanorods delivered a high electrical output of 85 V and 2.2  $\mu\text{A}$ . The significant aspect ratio and flexible characteristics of  $\text{ZnO}$  nanorods contributed to the improved piezoelectric properties of the nanocomposites. Moreover, the  $\text{ZnO}$  nanorods provided a nucleation effect on the crystallization of  $\beta$ -phase. The synergistic effects between nanofiller and  $\beta$ -crystals of PVDF in the composites are essential for the construction of flexible piezoelectric nanogenerator. Yun et al. (2016) fabricated nano-lead zirconate titanate (PZT)/PVDF composite nanofibers via electrospinning. They demonstrated that 20 wt% PZT content in PZT/PVDF composite led to enhanced

mechanical and piezoelectric properties of 2,052.6 MPa (Young modulus), 2.64  $\mu\text{C}/\text{cm}^2$  (maximum polarization), and 0.24  $\mu\text{C}/\text{cm}^2$  (remnant polarization). The piezoelectric characteristics of PZT with its undisturbed perovskite structure in the polymer matrix helped in achieving a higher piezoelectric response in the PZT/PVDF nanofibers.

Piezoelectric composite nanofiber-based on titanium dioxide ( $\text{TiO}_2$ ) and PVDF was investigated by Alam et al. (2018), which was fabricated by electrospinning. The embedded  $\text{TiO}_2$  nanoparticles in PVDF nanofiber led to the enhanced polar  $\beta$ -phase content (93%) and mechanical properties (Young's modulus of 22  $\text{N}/\text{mm}^2$ ) of the composite nanofiber. Energy harvesting of  $\text{TiO}_2$ /PVDF based nanogenerator demonstrated a maximum output voltage of 11.5 V and current of 176 nA, respectively, under a load of  $\sim 5$  N in the vertical direction. In addition, the nanogenerator demonstrated an energy conversion efficiency of 61%. The reduced fiber diameter and surface charge dipole interactions contributed by the cooperative effect of  $\text{TiO}_2$  and electrospinning led to the enhanced piezoelectric performance of the composite nanofibers. Bairagi and Ali (2019) prepared a piezoelectric nanogenerator based on potassium sodium niobate (KNN) nanorods incorporated in electrospun PVDF nanofibrous webs. The piezoelectric characteristics exhibited by 3% (wt/wt.) KNN/PVDF composite webs had an optimum output voltage of 17.5 V and 0.522  $\mu\text{A}$  current, respectively, under repetitive finger tapping. The inherent piezoelectric property and high aspect ratio of the KNN nanorods contributed to the piezoelectric response of composite webs. Moreover, the in-situ poling of both the embedded KNN nanorods and PVDF chains during electrospinning adds up to the piezoelectric response alongside the former.

To study the synergistic role of electrospinning and methylammonium lead bromide ( $\text{CH}_3\text{NH}_3\text{PbBr}_3$ ) (MAPbBr) on the energy harvesting capability of PVDF, Sultana et al. (2018) fabricated MAPbBr/PVDF nanofiber mats via electrospinning. The inclusion of synthesized MAPbBr (1 wt%) in PVDF nanofiber dramatically enhanced the  $\beta$ -phase fraction (91%) and tensile strength. MAPbBr in PVDF matrix acted as nucleating agent favoring the transformation of local amorphous regions into the  $\beta$ -crystalline phase of PVDF. The piezoelectric nanogenerator composed of

MAPbBr/PVDF composite nanofibers exhibited an output voltage, current, and charge of 5 V, 60 nA, and 8 nC, respectively, under periodic finger touch motion (9.8 kPa). The enhancement in the piezoelectric property was attributed to the molecular orientation of PVDF via the collective effect of electrospinning and incorporated MAPbBr. Moreover, a MAPbBr/PVDF composite nanofiber was also used as acoustic energy harvester, demonstrating an acoustic sensitivity of 13.8 V/Pa, and an energy conversion efficiency of 58.5%, respectively.

#### 1.1.4.2 Conducting fillers

Conducting fillers provide electrically conductive network pathways for the mobility of charges in the polymer matrix, thereby could contribute to the polarization of the polymer composites. Owing to their high-aspect-ratio and surface functionalization capability, fillers such as CNT, graphene can attain percolation thresholds at low loadings. Wu et al. (2018) investigated the effects of carbon nanotubes (CNT) and electrospinning on the crystal structure and piezoelectric response of aligned CNT/PVDF nanofiber membranes. The CNT embedded in PVDF electrospun fibers exhibited  $\beta$ -phase fraction of 89%, and the piezoelectric coefficient of  $d_{33}=31.3$  pC/N, respectively. In contrast, the aligned PVDF electrospun fiber reached  $\beta$ -phase fraction of 88%, and  $d_{33}=27.4$  pC/N, respectively. Furthermore, the aligned CNT/PVDF membranes showed improved piezoelectric response under dynamic compression (2.26 mV/N), tension (4.29 mV/%), and bending (1.89 V) in comparison to randomly orientated/aligned-PVDF electrospun fibers. They concluded that the mechanical stretching provided by the rotating collector during electrospinning facilitates the crystallization of  $\beta$ -phase. Also, the added CNT induces charge accumulation at the material boundary, thereby supports the all-trans conformation of PVDF. Thus, the improved  $\beta$ -phase fraction led to the enhanced piezoelectric coefficient of aligned CNT/PVDF membranes and, thereby, its piezoelectric response.

Yu et al. (2013) fabricated piezoelectric nanogenerator based on multi-walled carbon nanotubes (MWCNT)/PVDF nanofiber mats by electrospinning. The relative  $\beta$ -phase content of electrospun PVDF nanofiber reached 54.8%, while with the addition of 5 wt% MWCNT it increased to 68.4 %. The inclusion of MWCNT in the PVDF initiates inductive surface charges during the electrospinning process. Thus,

MWCNT acts as nucleation sites for PVDF chains to crystallize into  $\beta$ -phase, thereby exhibiting a higher  $\beta$ -phase content compared to pure electrospun PVDF nanofibers. The nanogenerator with 5 wt% MWCNT/PVDF composite nanofiber generated a maximum open-circuit output voltage and power up to 6 V and 81.8 nW, which was 200% and 44.8%, respectively higher than pure electrospun PVDF mats. This improved piezoelectric performance was attributed to the enhanced surface conductivity induced by the preferential alignment of MWCNTs in the PVDF nanofiber mats. Issa et al. (2017) enhanced the piezoelectric characteristics of PVDF by utilizing silver nanoparticles (Ag-NPs). The Ag-NPs/PVDF composite mats containing different concentrations of Ag-NPs (0-1 wt%) were prepared by electrospinning. The piezoelectric response of Ag-NPs/PVDF composite mats with 0.4 wt% Ag-NPs loading and at a 30 Hz vibrating frequency displayed an output voltage of 2 V. However, at a higher Ag-NPs content of 0.6 wt% the output voltage dropped. This was correlated to the  $\beta$ -phase content in the sample, which was affirmed by FTIR and DSC results. Furthermore, the electrospinning oriented the  $\beta$ -crystals of the PVDF composites, and effective interactions between Ag-NPs and PVDF chains further promoted the all-trans conformation and thereby the piezoelectric property.

The piezoelectric characteristics of PVDF nanofibers comprising of graphene nanoplatelets was probed by Abolhasani et al. (2017). The inclusion of graphene (0.1 wt%) in PVDF nanofiber induced the maximum  $\beta$ -phase fraction (83%), while additional graphene content reduced the same. The graphene nanoplatelets facilitated the PVDF chains in all-trans conformation due to the nucleating effect, which is commonly displayed by carbonaceous nanomaterials. Due to the higher  $\beta$ -phase content, the nanogenerator based on 0.1 wt% graphene/PVDF nanofiber displayed a maximum open-circuit voltage and short-circuit current of 7.9 V and 4.5  $\mu$ A, respectively. In contrast, the PVDF nanofibers produced an output voltage and current of 3.8 V and 2  $\mu$ A, respectively. Moreover, the addition of graphene above 0.1 wt % in PVDF deteriorated the piezoelectric performance, which was ascribed to the reduced  $\beta$ -phase fraction and crystallinity of nanofiber mats.

### 1.1.4.3 Non-conducting fillers

The addition of non-conducting fillers, in particular, clay-based materials provide excellent reinforcement and barrier property to the polymer matrix. Additionally, the high aspect ratio of the filler induces epitaxial growth of the  $\beta$ -phase owing to its interfacial interactions with PVDF chains. Organically modified nanoclay was used to tune the electroactive phase of PVDF by Tiwari et al. (2019). They fabricated piezoelectric nanogenerator based on organically modified nanoclay/PVDF composite nanofiber by varying the content of nanoclay. The inclusion of 15 wt% nanoclay in PVDF nanofiber led to the significant enhancement in the electroactive phases ( $\beta+\gamma$ ) by 90 % as opposed to 66.1% in the case of pure PVDF nanofibers. An optimum loading of nanoclay (15 wt%) facilitates the effective interaction with PVDF matrix and thereby in the crystallization of  $\beta$ -phase on the modified silicate layers of nanoclay. Moreover, the presence of nanoclay in the polymer matrix tends to develop surface charges that interact with the dipoles of PVDF chains leading to the promotion of the all-trans conformation. The nanofiber-based nanogenerator with 15 wt%/PVDF composite delivered an output voltage of 70 V and 68  $\mu\text{W}/\text{cm}^2$  power density, compared with 20 V and 23.2  $\mu\text{W}/\text{cm}^2$  of virgin PVDF nanofibers under finger tapping mode.

Khalifa et al. (2016) fabricated uniaxially aligned nanofibers developed from halloysite nanotubes (HNT)/PVDF nanocomposites by electrospinning method. The inclusion of HNT into PVDF improved the charge density of the polymer jet during electrospinning, thus leading to the reduced fiber diameter with bead free morphology. The cooperative effect of electrospinning and HNT led to the enhanced  $\beta$ -phase of PVDF based nanocomposite webs. The  $-\text{CH}_2$  and  $-\text{CF}_2$  groups of PVDF interact with the surface charges of HNT, thereby facilitating the all-trans  $\beta$ -phase. The  $\beta$ -phase fraction attained a maximum value of 81.1% with 10 wt% HNT loading, while that in the pure electrospun PVDF nanofiber was 34.6%. A force sensor was used to evaluate the piezoelectric activity of the nanocomposite webs. The 10 wt% HNT/PVDF nanocomposite webs exhibited a maximum output voltage of 955 mV at a load of 100 g. The piezoelectric response of the nanocomposite webs correlates with their  $\beta$ -phase content.



#### 1.1.4.4 Hybrid fillers

Hybrid fillers may be a simple amalgamation of two different fillers or maybe a product of chemical synthesis, which leads to the decoration of filler surface with nanoparticles (another filler). The potential benefits of hybrid fillers incorporated in polymer composites rely on filler dispersion, filler content, and nature of filler surface. In the recent past, hybrid fillers have proven to enhance and impart multifunctional properties in PVDF composites, thereby could contribute to EHS. Shi et al. (2018) reported the piezoelectric characteristics of electrospun PVDF nanocomposite fiber mats reinforced with BaTiO<sub>3</sub> nanoparticles and graphene nanosheets. The cooperative effect of BaTiO<sub>3</sub> nanoparticles and graphene nanosheets effectively contributed to the piezoelectric response of nanocomposite fiber mats. The maximum  $\beta$ -phase content in the PVDF nanocomposite fiber incorporated with BaTiO<sub>3</sub> (15 wt%) and graphene (0.15 wt%) reached a value of 91.1%. The substantial increment in the  $\beta$ -phase is ascribed to the effective interaction between the PVDF dipoles and the electric field around the filler. The interfacial interaction of PVDF with BaTiO<sub>3</sub>/graphene assists the orientation of  $-\text{CH}_2/-\text{CF}_2-$  dipoles, thus promoting the  $\beta$ -phase in the nanocomposite fiber mats. The nanogenerator based on PVDF nanocomposite mats loaded with BaTiO<sub>3</sub> /graphene produced a maximum voltage of 11 V and power of 4.1  $\mu\text{W}$  under a mechanical strain of 4 mm at 2 Hz. Further, the piezo-response of nanogenerator impacted by finger press-release mode yielded a peak voltage of 112 V, which was able to power 15 light-emitting diodes and energize an electronic watch.

Hosseini and Yousefi (2017) fabricated a piezo-sensor built on PVDF nanocomposite integrated with different ratios of MWCNT and organically modified montmorillonite (OMMT) nanoclay via electrospinning method. The addition of MWCNT and OMMT into the PVDF matrix resulted in the finer fiber diameter, which was ascribed to the improved viscoelastic effect experienced by the polymer jet during electrospinning. The hybrid nanocomposite with 0.05 wt% MWCNT and 0.1 wt% OMMT displayed the highest  $\beta$ -phase content in comparison to the pure electrospun PVDF mats. This was due to the good interaction between the negatively charged surface of OMMT and positive  $-\text{CH}_2$  dipoles of PVDF, leading to the

improvement of electroactive  $\beta$ -phase. The piezo-sensor based on 0.05 wt% MWCNT /0.1 wt% OMMT/PVDF nanocomposite under the impact load of 6 N displayed the sensitivity of 10.9 mV/N relative to 8.25 mV/N for the pure electrospun PVDF mats. The improved piezoelectric sensitivity here is ascribed to the content and polarization of  $\beta$ -phase in the PVDF matrix. The influence of carboxyl functionalized multiwall carbon nanotubes (CNTs) and silver (Ag) nanoparticles on the piezo-response of electrospun PVDF nanofiber mats was systematically studied by Sharma et al. (2016). The Ag-CNTs embedded PVDF nanofibers led to the reduced fiber diameter in comparison to the pure PVDF nanofiber mats. Moreover, the  $\beta$ -phase content was also enhanced in the presence of Ag-CNTs in the PVDF nanofiber mats. This was due to the good interaction between the Ag-CNTs and PVDF that induced charge accumulation at the surface, thus facilitating the transformation of polymer chains to  $\beta$ -phase conformation. The piezoelectric coefficient of the Ag-CNTs/PVDF nanofibers was  $54 \pm 5$  pm/V compared to  $30 \pm 2$  pm/V for the pure electrospun PVDF nanofibers. The improved piezoelectric coefficient here is ascribed to the  $\beta$ -phase fraction and rearrangement of dipoles in the PVDF nanofibers.

Additionally, additives such as metal salts, ionic liquids, and a few polymers have also been demonstrated to enhance the electroactive phase of PVDF [Dhakras et al. 2012; Xing et al. 2014; Mokhtari et al. 2016; Pickford et al. 2019; Mahdavi Varposhti et al. 2020; Ünsal et al. 2020] due to their interfacial interactions with blended PVDF matrix. There are several reports on fillers tuning the piezoelectric properties of electrospun PVDF composites. However, Table 1.3 summarizes a few different types of fillers and their effect on the piezoelectric characteristics of the PVDF matrix.

Conclusively, the selection of filler plays a pivotal role in modifying, imparting, and enhancing the functional properties of PVDF based composites. Generally, the positively charged surface of the filler gets interacted with  $-\text{CF}_2$  groups of PVDF via H-bonding, while the negatively charged surface is attracted towards  $-\text{CH}_2$  groups of PVDF via ion-dipole interaction thereby promoting the  $\beta$ -phase. The functionalization of filler ensures its uniform dispersion and effective interactions with the polymer matrix. Moreover, the orientation of dipoles induced by

electrospinning facilitates the  $\beta$ -phase of PVDF. A possible interaction mechanism between fillers with different morphology and PVDF chains in electrospun PVDF based composite is illustrated in Fig.1.7.

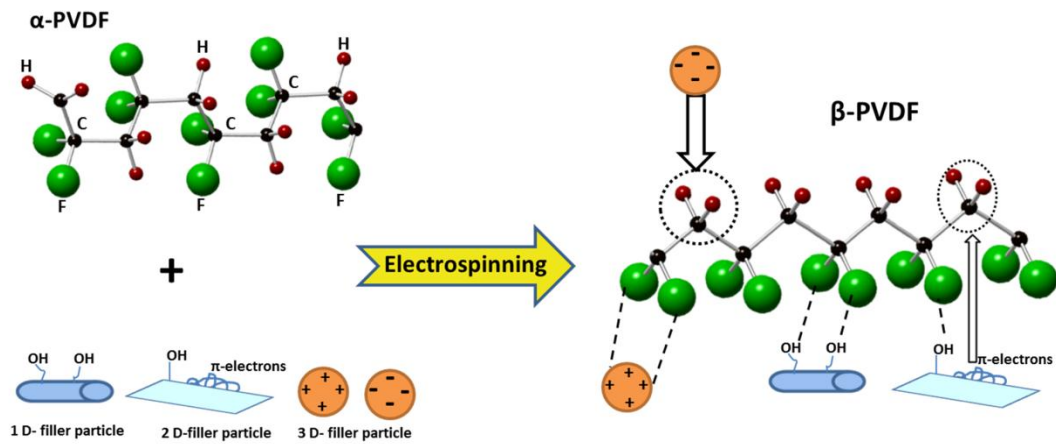


Fig.1.7 Plausible interaction mechanism between various fillers and PVDF matrix, thereby facilitating the  $\beta$ -phase conformation in electrospun PVDF composite nanofabrics.

Table 1.3 Influence of various fillers/additives on the piezoelectric performance of electrospun PVDF based composite nanofabrics.

| Fillers/Additives                    | Solvent                   | Diameter of fiber (nm) | Remarks  | References              |
|--------------------------------------|---------------------------|------------------------|--|-------------------------|
| Platinum (Pt)                        | DMF/Acetone               | ~600                   | High output voltage ~30 V, current ~ 6 mA/cm <sup>2</sup> , and power density ~22 $\mu$ W/cm <sup>2</sup> .  | [Ghosh and Mandal 2018] |
| ZnO                                  | DMF/Tetrahydrofuran (THF) | 200-1000               | Displayed a maximum output power of 32 nW/cm <sup>2</sup> over a load of 50 k $\Omega$ at 8 Hz   | [Mansouri et al. 2019]  |
| Nickel chloride hexahydrate          | DMF                       | 100-140                | Exhibited polar $\beta$ -phase of 92% and piezo-voltage of 0.762 V   | [Dhakras et al. 2012]   |
| Polybenzoxazole (PBO)/Graphene       | DMF/Acetone               | 30-130                 | The maximum voltage of 60 V was attained.  | [Barstugan et al. 2019] |
| Ca–Al layered double hydroxide (LDH) | DMF/Acetone               | ~282                   | Displayed an enhanced electroactive $\beta$ -phase of 82.79%. And an output voltage of 5.72 V.   | [Shamitha et al. 2020]  |
| Polyaniline (PANi)/HNT               | DMF/Acetone               | ~205                   | The $\beta$ -phase content of 84.1% with output voltage, current, and power density of 7.2 V, 0.75 $\mu$ A, and 0.25 $\mu$ W/cm <sup>2</sup> , respectively. | [Khalifa et al. 2019]   |

|  |             |      |   |                             |
|--|-------------|------|---|-----------------------------|
| Silane modified KNN (SM-KNN)                                     | DMF/Acetone | ~646 | The remarkable output voltage, current, current density, and power density of 21 V, 22 $\mu$ A, 5.5 $\mu$ A/cm <sup>2</sup> , and 115.5 $\mu$ W/cm <sup>2</sup> , respectively. | [Bairagi and Ali 2020]      |
| Reduced graphene oxide (RGO)/PANi                                | DMF/Acetone | ~470 | The maximum output voltage of 10.60 V was achieved.   | [Ünsal et al. 2020]         |
| Molybdenum Disulfide (MoS <sub>2</sub> )                         | DMF/Acetone | ~75  | The polar $\beta$ -phase of 95% and an output voltage of 14 V were achieved.  | [Maity et al. 2017]         |
| Lithium chloride (LiCl)  | DMF/Acetone | ~65  | The maximum output voltage of 8V with a voltage response sensitivity of 228.5 V/J.  | [Mokhtari et al. 2016]      |
| KNN  | DMF/Acetone | –    | The $\beta$ -phase of 68% and an output voltage of 1.9 V were achieved.   | [Teka et al. 2018]          |
| Iron oxide (Fe <sub>3</sub> O <sub>4</sub> )/graphene oxide (GO) | DMF/Acetone | ~117 | The piezoelectric sensitivity was 1.75 mV/N.  | [Samadi et al. 2018]        |
| TiO <sub>2</sub> /Fe <sub>3</sub> O <sub>4</sub> /MWCN T)        | DMF/Acetone | –    | Enhanced $\beta$ -phase and maximum piezoelectric sensitivity of 51.42 mV/N.  | [Samadi et al. 2019]        |
| PANi/graphitic   | DMF/Acetone | ~288 | Nanogenerator produced an output  | [Khalifa and Anandhan 2019] |

|  |                                   |               |  |                           |
|--|-----------------------------------|---------------|--|---------------------------|
| carbon nitride (g-C <sub>3</sub> N <sub>4</sub> )  |                                   |               | voltage of 30 V and a current of 3.7 $\mu$ A, respectively, with good stability and reproducibility.   |                           |
| Ce-Fe <sub>2</sub> O <sub>3</sub> (cerium-ferric oxide) and Ce-Co <sub>2</sub> O <sub>4</sub> (cerium-cobalt tetraoxide) | DMF/Acetone                       | ~205 and ~262 | Both exhibited output voltages of 20 V and 15 V, respectively, with corresponding currents of 0.010 $\mu$ A/cm <sup>2</sup> and 0.005 $\mu$ A/cm <sup>2</sup> under the load of 2.5 N. | [Parangusan et al. 2019]  |
| Fluorinated graphene oxide (GOF) and carboxylated graphene oxide (GOCOOH)  | Dimethylacetamide (DMAc) /Acetone | ~619 and ~622 | Both produced piezoelectric coefficients of 63 pm/V and 46 pm/V, respectively. Accordingly, the $\beta$ -phase was 79% and 89%.  | [Gebrekrstos et al. 2018] |

## **1.2 PROBLEM IDENTIFICATION**

Electroactive polymers, in particular PVDF, have tremendous advantage over ferroelectric and piezoelectric ceramics in terms of their ease of production at low temperature, better flexibility, high strains of failure and toughness. PVDF can be produced as large thin sheets and stamped into any desired shape, exhibiting increased mechanical strength and impact resistance. The electroactive polymers have a lower permittivity and lower piezoelectric coefficients compared to ferroelectric ceramics. This can be surmounted by the cooperative effects of nanofillers and electrospinning, contributing in promoting polar electroactive phase in the PVDF matrix. Based on these facts, the present study explores tailoring of the structural and piezoelectric properties of electrospun PVDF nanofabrics by strategic incorporation of chosen nanofillers and the prospective applications of the resultant composite nanofabrics.

## **1.3 SCOPE AND OBJECTIVES OF THE PRESENT WORK**

### **1.3.1 Scope**

PVDF has been extensively studied polymer due to its appealing piezoelectric, pyroelectric and ferroelectric properties. In recent years, extensive research has been carried to produce efficient ceramic-polymer hybrid composite material, possessing improved mechanical properties and better piezoelectric charge coefficients for energy harvesting systems. The inclusion of nanofillers such as clay, graphene and carbon nanotubes promotes the polar phases in PVDF. Electrospinning is a one-step process to produce electroactive phases in PVDF without any further post treatments. The piezoelectric properties of PVDF have been employed in the production of sensors, energy harvesters, artificial muscles and mechanical actuators. The overall aim of this research is to develop an electrospun PVDF-based composite nanofabrics with improved mechanical, dielectric and piezoelectric characteristics by the inclusion of functional 2D-nanosheet based fillers.

### **1.3.2 Objectives**

- Synthesis of organically modified Ni-Co LDH/PVDF composite nanofabrics under optimized electrospinning conditions.

- Synthesis of talc nanosheets/PVDF composite nanofabrics under optimized electrospinning conditions.
- Synthesis of talc nanosheets/carboxyl functionalized graphene nanosheets/PVDF hybrid composite nanofabrics under optimized electrospinning conditions.
- Characterization of the aforementioned nanofabrics through X-ray diffraction (XRD), scanning electron microscopy (SEM), energy dispersive X-ray spectroscopy (EDS), Fourier transform infrared (FTIR) spectroscopy, thermogravimetric analysis (TGA), differential scanning calorimetry (DSC), transmission electron microscopy (TEM), and piezoresponse force microscopy (PFM).
- Investigation on the suitability of the synthesised PVDF-based composite nanofabrics in piezoelectric applications.



# **CHAPTER 2**



## CHAPTER 2

### MATERIALS AND METHODS

---

*This chapter discusses the materials used in the fabrication of PVDF-based composite nanofabrics and the physico-chemical characterization and evaluation of these nanofabrics for piezoelectric applications. The synthesis of nanofillers such as organically modified Ni-Co layered double hydroxide (OLDH) and carboxyl functionalized graphene nanosheets (FGNS), with detailed characterization techniques adopted in this study, has been discussed.*

#### 2.1 MATERIALS

PVDF powder (Solef® 1015,  $\overline{M}_W = 575,000$ , Belgium) was obtained from Prakash Chemicals Pvt.Ltd, Vadodara, India. Nickel nitrate hexahydrate ( $\text{Ni}(\text{NO}_3)_2 \cdot 6\text{H}_2\text{O}$ ), cobalt nitrate hexahydrate ( $\text{Co}(\text{NO}_3)_2 \cdot 6\text{H}_2\text{O}$ ), urea, ethylene glycol, and acetone were purchased from Merck, India. Sodium dodecylbenzene sulfonate (SDBS) was purchased from Sigma Aldrich, India. Talc nanoparticles (Celina-80<sup>®</sup>, Nanoshel, USA, Purity: 99.9%, Average particle size ; < 100nm) were obtained from Intelligent Materials Pvt. Ltd., Punjab, India. Natural graphite flakes, sodium nitrate, potassium permanganate, hydrogen peroxide, sulphuric acid, hydrochloric acid, para-aminobenzoic acid were procured from Sigma Aldrich, Korea. *N, N'*-dimethylformamide (DMF) and acetone were purchased from Molychem, India. All the chemicals were of analytical grade (purity > 99%) and used without further purification.

#### 2.2 METHODS

##### 2.2.1 Synthesis of organically modified Ni-Co layered double hydroxide (OLDH)

The OLDH was prepared by the one-step route as follows: 2.5 mmol of  $\text{Ni}(\text{NO}_3)_2 \cdot 6\text{H}_2\text{O}$  and 5 mmol of  $\text{Co}(\text{NO}_3)_2 \cdot 6\text{H}_2\text{O}$  (Ni: Co = 1:2) was added to the

solution mixture of 37.5 mL ethylene glycol and 15 mL deionized water. Once the precursors dissolved, 37.5 mmol of urea was added slowly and stirred, until a clear solution was formed. The resulting metal salt solution mixture was then transferred into a three-neck round-bottom flask. To this, 0.2 M solution of sodium dodecylbenzene sulfonate in 25 mL of deionized water was introduced under reflux for 6 h at 90 °C. Then, the precipitates were separated by filtration and washed with demineralized water several times and then dried at 60 °C. Unmodified Ni-Co LDH was also prepared by the procedure mentioned previously [Li et al. 2016], which is denoted as LDH.

### **2.2.2 Electrospinning of OLDH/PVDF composite nanofabrics**

Electrospinning solution of PVDF with different loadings of OLDH (0, 1, 3, 5 and 7 wt%, based on the weight of PVDF) was prepared in a mixture of DMF/acetone (9/1 v/v) at room temperature. Firstly, the desired percentage of OLDH was ultrasonicated in the solvent mixture for 2 h at 28 °C, and then PVDF (13.5 w/v%) was added to this dispersion and the mixture was continuously stirred for 8 h. The resultant mixture was then loaded into a 10 mL syringe having a 22-gauge stainless steel needle with a bevelled edge, and the solution flow rate was regulated at 0.8 mL h<sup>-1</sup>. Electrospinning was carried out using a single spinneret vertical electrospinning setup (ESPIN-NANO model V1, Physical equipments Co., Chennai, India) under the following optimized conditions: relative humidity: 55±2 %; drum collector speed: 1200 rpm; temperature: 30 °C; voltage: 16 kV; spinneret tip to collector distance: 15 cm.

### **2.2.3 Electrospinning of talc/PVDF composite nanofabrics**

The dispersion of talc was prepared by dispersing the desired quantity of talc nanoparticles (0.25, 0.50, 0.75, and 1 wt%) in the solvent (blend ratio 9:1 v/v) of DMF/acetone by ultrasonication for 1 h at 28 °C. To this dispersion, PVDF powder (13.5 wt/v%) was introduced and the resultant mixture was magnetically stirred for at least 10 h to ensure homogeneity. The resultant as-prepared solution was transferred to a 10 mL dispovan syringe with 22 gauge needle (0.5 mm diameter) and loaded to a vertical electrospinning instrument (ESPIN-NANO model V1, Physical equipments Co., Chennai, India). Electrospinning was performed at room temperature (28 ± 2 °C)

under a relative humidity of  $50 \pm 2\%$ . The electrospun fabrics were collected on an aluminum foil that was wrapped on the rotating drum collector (1400 rpm) and placed at a distance of 16 cm from the needle tip of the syringe. The flow rate and voltage were maintained at  $0.6 \text{ mL h}^{-1}$  and 18 kV, respectively.

#### **2.2.4 Synthesis of graphene oxide (GO) and reduced graphene oxide (RGO)**

GO was prepared from purified natural graphite according to modified Hummer's method [Hummers and Offeman 1958; Ryu et al. 2014]. Typically, 1 g of graphite flakes was dispersed in 100 mL of sulphuric acid by sonication for 30 min, followed by addition of 1g of sodium nitrate. To the resultant mixture, 6 g of potassium permanganate was gently added under the ice-cold condition. This mixture was stirred for 2 h maintaining the water bath temperature at  $35 \text{ }^\circ\text{C}$ . Next, 40 mL of de-ionized water ( $70 \text{ }^\circ\text{C}$ ) was added drop-wise to the solution, and the temperature of the solution was elevated to  $90 \text{ }^\circ\text{C}$ . At last, 140 mL of de-ionized water ( $70 \text{ }^\circ\text{C}$ ) followed by 20 mL of hydrogen peroxide (30 wt%) was added so as to terminate the reaction. The as-prepared GO dispersion was purified via the dialysis route to remove any residual salts and acids. Finally, the resultant GO was dried overnight in a vacuum oven at  $60 \text{ }^\circ\text{C}$ .

For the preparation of RGO, above synthesized GO was subjected to a temperature of  $400 \text{ }^\circ\text{C}$  in a muffle furnace under a nitrogen atmosphere for 3 h.[López Guerra et al. 2013]

#### **2.2.5 Synthesis of carboxyl functionalized graphene nanosheets (FGNS)**

The chemical functionalization of RGO was done via a diazonium coupling reaction using aminobenzoic acid [Athanasakou et al. 2019]. Briefly, 960 mg of para-aminobenzoic acid was added to 80 mL deionized water. To this solution, 526 mg (7.6 mmol) sodium nitrate was introduced slowly via a dropper, while the solution was maintained in an ice bath and stirred till the solution became clear. Next, 6 mL HCl (20 v/v%) solution was quickly added and stirred for another 45 min till the solution turned yellow. The resultant diazonium salt solution was added to an aqueous solution of RGO (250 mg), maintained at  $5 \text{ }^\circ\text{C}$ , and stirred for 6 h. After this, the reaction mixture was further stirred for 8 h under ambient conditions. Finally, the

obtained products were filtered and washed repeatedly with de-ionized water and later dried overnight in vacuum at 60 °C to obtain FGNS. The schematic illustration of the synthesis method was displayed in Fig.2.1.

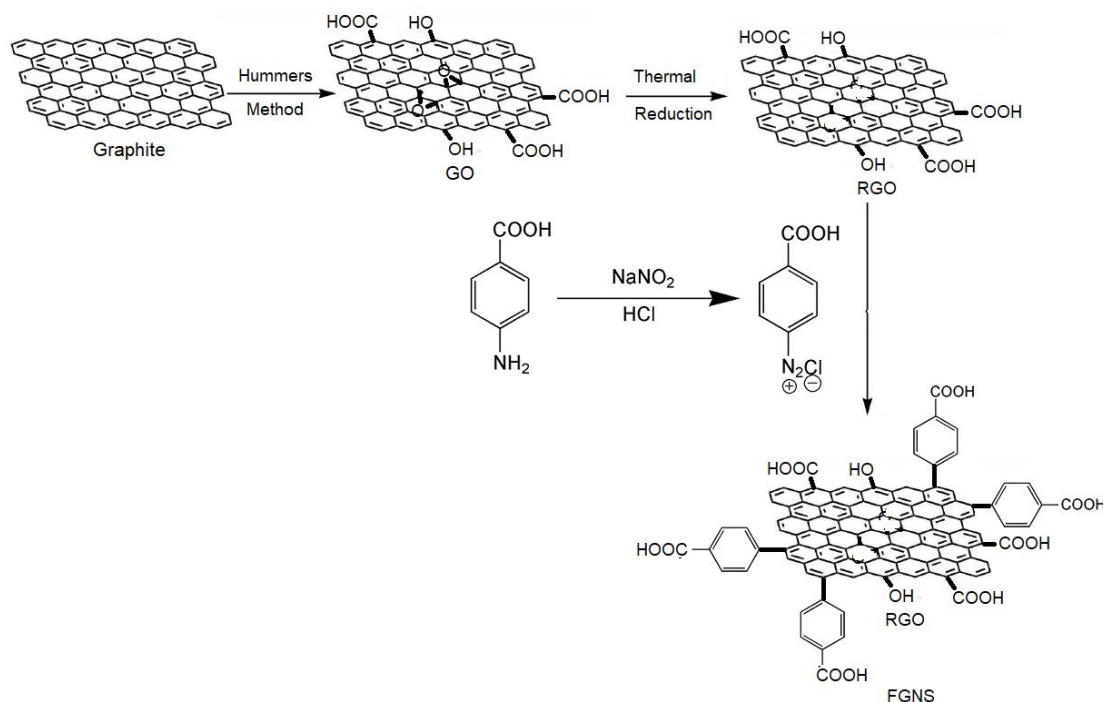


Fig.2.1 Schematic depicting the synthesis of GO, RGO, and FGNS.

### 2.2.6 Electrospinning of PVDF and 0.50 wt% talc nanosheets/FGNS/PVDF (TGP)-based composite nanofabrics

For preparing electrospun PVDF nanofabrics (E-PVDF), PVDF powder (13.5 wt/v%) was dissolved in 9:1 v/v mixture of DMF/acetone and stirred for 10 h at 30 °C. For the TGP-based composite nanofabrics, desired amount of FGNS was first dispersed in the solvent mixture by ultrasonication for 1 h, and then talc nanosheets were added under stirring followed by ultrasonication for another 1 h. To the resultant mixture, PVDF powders were added followed by continuous magnetic stirring for 10 h to produce a homogeneous electrospinning solution. For the TGP-based system, talc nanosheets content was fixed at 0.50 wt% and FGNS loading was varied (0.05, 0.10, 0.15, and 0.20 wt%) relative to PVDF. The prepared electrospinning solution was then loaded into a 10 mL syringe with a stainless steel needle (22-G), and

electrospinning was performed at 30 °C on a vertical electrospinning unit (ESPIN-NANO model V1, Physical equipments Co., Chennai, India) under the following optimized conditions: voltage 18 kV; flow rate 0.6 mL/h; tip to collector distance 16 cm; rotating drum collector speed 1400 rpm; and relative humidity  $52 \pm 2$  %.

### 2.3 MEASUREMENT AND CHARACTERIZATION

The morphology of OLDH, talc nanosheets, and electrospun nanofabrics were evaluated using scanning electron microscopy (SEM) (JSM-6380LA, JEOL, Japan). The morphology of GO, RGO, FGNS, and TGP-based composite nanofabrics were examined by field emission scanning electron microscopy (FESEM) (ZEISS GeminiSEM-300, Germany). All the samples were gold sputtered using auto fine coater (JFC-1600, JEOL, Japan) before SEM/FESEM observations. The mean fiber diameter of electrospun nanofabrics was measured using the Image-J software (a total of 50 nanofibers were considered from the SEM/FESEM images). The assessment of filler dispersion and distribution in the polymer matrix was evaluated using elemental mapping by energy dispersive X-ray spectroscopy (EDS) (AMETEK, Model-E1816-C2B EDS, USA). Transmission electron microscope (TEM) (JEOL-JEM 2100, Japan) was also performed at an accelerating voltage of 200 kV to evaluate the morphology of nanofillers and PVDF-based composite nanofabrics. For the TEM analysis, a small quantity of these nanofiller samples was ultrasonicated in ethanol solution for 2h, and then this solution mixture was drop cast onto the carbon-coated grid (200 mesh) followed by drying of the copper grid in the vacuum oven for 10 h. In the case of nanofabrics, the nanofibers were directly spun on the copper grid, and later the grid was dried.

Fourier transform infrared (FTIR) spectroscopy (JASCO, Model-FT/IR 4200 LE, Japan) was used to obtain the spectra of the samples in the KBr-transmission mode ( $4000-400 \text{ cm}^{-1}$ ) and attenuated total reflectance (ATR) mode ( $4000-650 \text{ cm}^{-1}$ ) at a resolution of  $4 \text{ cm}^{-1}$  and 32 accumulated scans. The percentage fraction of the  $\beta$ -phase  $F(\beta)$  in the electrospun nanofabrics was calculated using the equation (2.1) [Gregorio, Jr. and Cestari 1994], conforming Lambert-Beer's law.

$$F(\beta) = \frac{A_{\beta}}{\left(\frac{K_{\beta}}{K_{\alpha}}\right)^{A_{\alpha}+A_{\beta}}} \times 100\% \quad (2.1)$$

In the equation,  $A_\alpha$  and  $A_\beta$  represent measured absorbance at  $763\text{ cm}^{-1}$  and  $840\text{ cm}^{-1}$ , respectively. The values of absorbance coefficients at  $763\text{ cm}^{-1}$  and  $840\text{ cm}^{-1}$  are  $K_\alpha=6.1 \times 10^4$  and  $K_\beta=7.7 \times 10^4\text{ cm}^2\text{ mol}^{-1}$ , respectively.

To validate the formation of OLDH, high-resolution X-ray diffractometer (Rigaku Smartlab, USA) was carried out with Cu  $K_\alpha$  radiation of  $0.154\text{ nm}(\lambda)$  operating at 40 kV and 30 mA. The sample was scanned at the rate of  $1^\circ/\text{min}$  over the  $2\theta$  range of  $2^\circ$  to  $40^\circ$ . The interplanar distance ( $d$ ) was calculated from equation (2.2).

$$d = \frac{\lambda}{2\sin\theta} \quad (2.2)$$

The phases and crystallinity of electrospun nanofabrics were determined by another X-ray diffractometer (Rigaku Miniflex 600-5<sup>th</sup> generation, USA) operating at 40 kV and 15 mA,  $2\theta$  range of  $10^\circ$  to  $50^\circ$  and a scan rate of  $1^\circ/\text{min}$ . The % crystallinity ( $\chi_c$ ) was determined using equation (2.3).

$$\chi_c = \frac{A_c}{A_a + A_c} \times 100\% \quad (2.3)$$

Where,  $A_c$  and  $A_a$  are the integrated areas of the XRD peaks pertaining to crystalline and amorphous phases, respectively. Further the XRD patterns of GO, RGO, and FGNS was evaluated using X-ray diffractometer (Empyrean-Malvern Panalytical, UK) with Cu  $K_\alpha$  radiation ( $\lambda=0.154\text{ nm}$ ) under 45 kV and 30 mA.

The thermal behavior of electrospun nanofabrics was evaluated by thermogravimetric analysis (TGA) and differential scanning calorimetry (DSC) under a nitrogen environment. The TGA traces of the electrospun nanofabrics were recorded using a thermogravimetric analyzer (TA instruments, Model-TGA Q500, Germany) from  $25\text{ }^\circ\text{C}$  to  $600\text{ }^\circ\text{C}$  at a heating rate of  $10\text{ }^\circ\text{C}/\text{min}$ . The overall crystallinity and melting temperature of electrospun nanofabrics were obtained by differential scanning calorimetry (DSC) (822E, Mettler Toledo, USA) with a heating rate of  $10\text{ }^\circ\text{C}/\text{min}$  from  $25\text{ }^\circ\text{C}$  to  $200\text{ }^\circ\text{C}$ . The % crystallinity ( $\chi_c$ ) of the nanofabrics was calculated according to equation (2.4).

$$\chi_c = \frac{\Delta H_{\text{sample}}}{\Delta H_{100\%}} \times 100\% \quad (2.4)$$

Where  $\Delta H_{\text{sample}}$  and  $\Delta H_{100\%}$  denotes the enthalpies of fusion of the sample and 100 % crystalline PVDF, given as  $104.7\text{ Jg}^{-1}$  [Liu et al. 2013].

The dielectric properties of electrospun nanofabrics were analyzed using a precision LCR Meter (E4980A, Keysight, USA) in the frequency range of 1k to 1MHz



at room temperature. Data measurements were done by sandwiching the sample between two copper electrodes. The dielectric constants ( $\epsilon_r$ ) of the samples were calculated using equation (2.5).

$$\epsilon_r = \frac{Cd}{\epsilon_0 A} \quad (2.5)$$

Where C is the capacitance, d is the thickness of the sample, A is the area of the electrode and  $\epsilon_0$  is the permittivity of free space ( $8.854 \times 10^{-12} \text{ Fm}^{-1}$ ).

Tensile testing of the electrospun nanofabrics was done using a universal testing machine (INSTRON, Model-5967, USA) at room temperature and in accordance with ASTM D882. All the test samples (60 mm  $\times$  10 mm) were subjected to a crosshead speed of 5 mm/min.

Raman spectra of RGO and FGNS were acquired using a Raman spectrometer (Horiba-LabRAM HR, France) using a 532 nm laser source.

The piezoelectric responses of individual nanofibers (pristine PVDF and composite nanofibers) were measured using piezoresponse force microscopy (PFM) mode of an atomic force microscope (MFP-3D-BIO, Asylum Research, USA). The nanofibers were directly electrospun on a gold-coated glass slide for 10 s. Ti/Ir coated silicon conductive cantilever (ASYELEC-01, Asylum Research, USA) with a spring constant of 2 N/m and resonant frequency of 70 kHz was used for PFM measurements. DART-PFM (dual alternating current (AC) resonance tracking) mode was used to analyze the nanofiber's vertical piezoelectric response (contact frequency 290-310 kHz). The nanodomain switching properties of the individual nanofiber was assessed by SS-PFM (switching spectroscopy) mode. At least five different locations on a single nanofiber were considered for the PFM analysis.

### **2.3.1 Setups and methodology used for piezoelectric performance evaluation of PVDF-based composite nanofabrics**

The piezoelectric response of the electrospun composite nanofabrics was evaluated using an indigenously developed nanogenerator (Fig.2.2). The electrospun fabrics were sandwiched between two copper electrodes (3.0 cm  $\times$  2.0 cm) that were covered with a polymer film (ethylene-octene copolymer, thickness of 0.5 mm), and the entire set-up was wrapped with an adhesive tape (transparent scotch tape). The piezoelectric

response (voltage and current) of the nanogenerator under repetitive finger imparting was recorded using a USB oscilloscope (Digilent, Model-Analog Discovery 2, USA) and picoammeter (SES instruments, Model-DPM-111-C2, India). The finger imparting force on the nanogenerator ( $\sim 3.8$  N) was measured by a force sensor (Kistler, Model-9712B5, Switzerland).

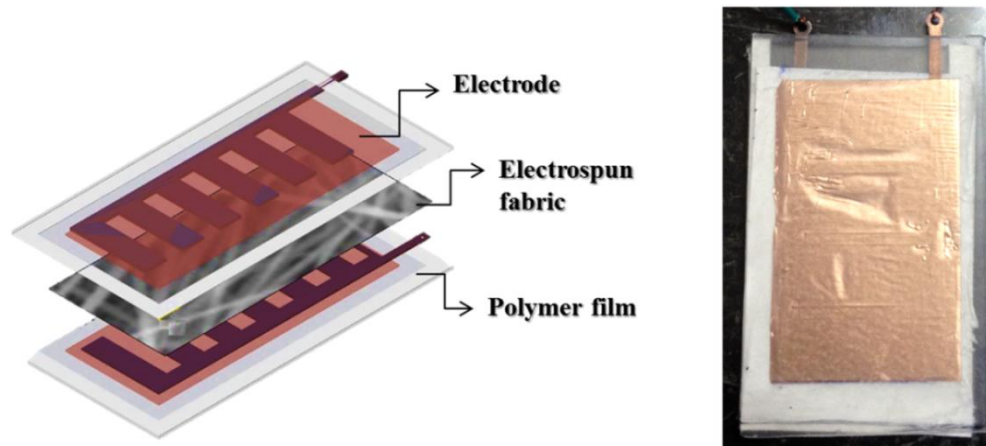


Fig.2.2 Schematic demonstrating the construction, and photographic image of the nanogenerator.

The frequency modulated-shaker mode consisted of Modal Shaker (YMC Piezotronics Inc, Model-MS-100, China), Function/Arbitrary Waveform Generator (Keysight technologies, Model-33220A, USA) and Voltage Module (National Instruments, Model- NI-9215C, USA). The output voltage was measured by a voltage module interfaced with a computer (LabVIEW software). Accordingly, the nanogenerator is fixed at one end, and the free end is attached to the steel ruler ( $34 \times 2.5 \times 1$  cm) using double-sided adhesive foam tape. The steel ruler scale is linked to a piezoelectric shaker that excites the former. The nanogenerator based on electrospun fabric is deformed mechanically by varying the vibrational frequency of the shaker using a frequency generator. The output response of the nanogenerator under varying frequency modes ( $1 V_{PP}$ , 10 to 50 Hz) is recorded using a data acquisition device interfaced with the computer. Fig.2.3.a and b depict the set-up for frequency modulated-shaker mode.

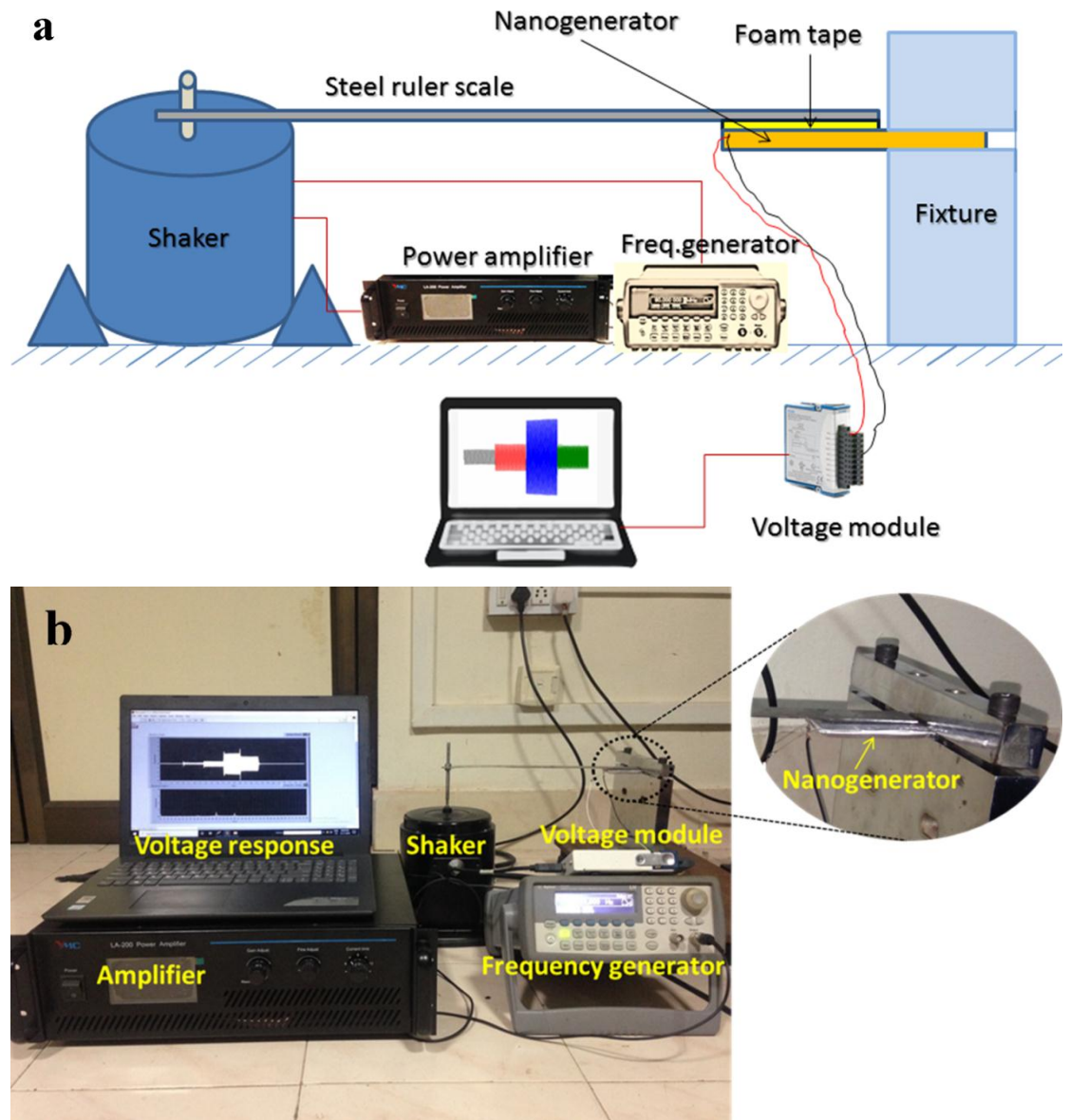


Fig.2.3 Illustration of piezoelectric evaluation of E-PVDF and talc/PVDF fabrics based nanogenerator by frequency modulated-shaker mode; (a) Schematic, and (b) Photographic image of the set-up.

In the pneumatic-actuator mode, the assembled nanogenerator (Fig.2.2) was mechanically impacted by a custom-built pneumatic compression setup (FESTO-DSNU-20-100-P-A, Germany) operating at an inlet pressure of 0.4 MPa (Fig.2.4). A pneumatic actuator impacts the nanogenerator composed of electrospun nanofabrics in the vertical direction. The pneumatic actuator is operated using a 5/2-push button. The nanogenerator under impact and release modes are shown in Fig.2.4, and their

corresponding output response is measured using an oscilloscope (Digilent-Analog Discovery 2, USA), and the piezoresponse is displayed on the laptop.

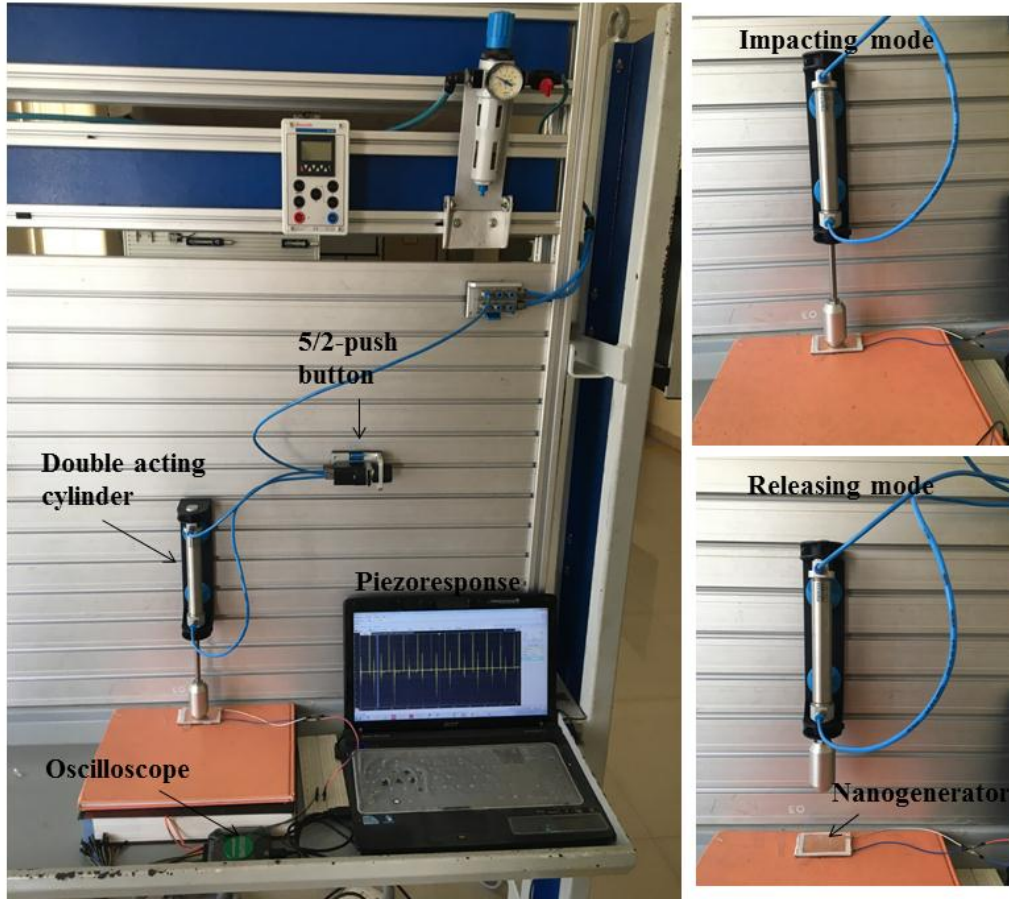


Fig.2.4 Schematic of piezoelectric response evaluation for electrospun nanofabrics based nanogenerator by pneumatic-actuator mode.

# CHAPTER 3

---

The results of this chapter have been published in *Journal of Materials Science: Materials in Electronics*, 2019, 30, 20703–20715.



## CHAPTER 3

# ORGANO-MODIFIED Ni-Co LDH: ON THE POLYMORPHISM, DIELECTRIC, AND PIEZOELECTRIC RESPONSE OF ELECTROSPUN POLY(VINYLLIDENE FLUORIDE) NANOFABRICS

---

*In this study, organically modified Ni-Co layered double hydroxide (OLDH) was synthesized and the nanosheets of this OLDH were used as filler in electrospun PVDF nanofabrics. Morphology, crystallinity, dielectric, and piezoelectric properties of the electrospun nanofabrics were characterized. Dielectric constant of the nanofabrics tend to increase with OLDH content, while the corresponding dielectric loss remained low. An indigenously designed nanogenerator was used to evaluate the piezoresponse of OLDH/PVDF nanofabrics. The synergistic effect of OLDH and electrospinning contributed to the enhancement of the  $\beta$ -phase content, thereby the piezoelectric response of the composite nanofabrics.*

### 3.1 RESULTS AND DISCUSSION

#### 3.1.1 Characterization of OLDH

The XRD patterns of LDH (Fig.3.1a) revealed peaks centered at  $2\theta$  values of  $10.6^\circ$ ,  $22.2^\circ$ , and  $32.8^\circ$  indexed as (0 0 3), (0 0 6), and (0 1 2) planes of cobalt nickel carbonate hydroxide hydrate (ICDD-033-0429), respectively. For OLDH the basal reflections shifted to lower  $2\theta$  angles of  $2.9^\circ$  and  $6.0^\circ$  (Fig.3.1b). The modification of LDH with SDBS resulted in the shift of basal reflection, indicating an increased expansion in the interlayer space of LDH. This increase in d-value from 0.83 nm ( $\text{LDH}_{(003)}$ ) to 3.04 nm ( $\text{OLDH}_{(003)}$ ) is attributed to the monolayer arrangement of SDBS ions in the interlayer space of LDH [Costa et al. 2008].

FTIR analysis was performed to ascertain the presence of SDBS ions in the OLDH interplanar space. FTIR spectra of LDH and OLDH are shown in Fig.3.1c. For LDH, the broadband in the range of  $3200\text{-}3700\text{ cm}^{-1}$  corresponds to O-H stretching vibration of the metal hydroxide layer and interlayer water molecules. The band centered at  $1630\text{ cm}^{-1}$  is ascribed to O-H bending vibration of water molecules. The

band at  $1383\text{ cm}^{-1}$  indicates the vibrations due to the  $\text{CO}_3^{2-}$  and  $\text{NO}_3^-$  interlayer anions. Additionally, the broad peak at  $624\text{ cm}^{-1}$  is ascribed to the M-O (M=Ni, and Co) and M-O-M vibrations. In the OLDH spectrum, bands appearing at  $2952$  and  $2855\text{ cm}^{-1}$  resulted from the  $\text{CH}_2$  stretching vibration of sulfonate chains. The bands around  $1592$  and  $1408\text{ cm}^{-1}$  are due to the C=C stretching of benzene ring. The asymmetric and symmetric stretching of S=O present in SDBS appears at  $1186$  and  $1038\text{ cm}^{-1}$ , respectively [Xu and Braterman 2003]. The sharp band at  $832\text{ cm}^{-1}$  is assigned to CH aromatic out of plane bending. The sharp peak appearing at  $426\text{ cm}^{-1}$  arises due to the lattice vibration related to metal hydroxide layers [WANG et al. 2009].

SEM image of LDH revealed its flake-like morphology (Fig.3.2a). In comparison to LDH, the OLDH retained its flake-like morphology with more irregularity at the edges. This was probably due to the larger size of SDBS anions, which intercalate in to the galleries of LDH; this influences the assembly and thickening of metal hydroxide sheets during the regeneration process (Fig.3.2b). Also, the TEM micrograph of OLDH (Fig.3.2c) confirmed its layered structure.

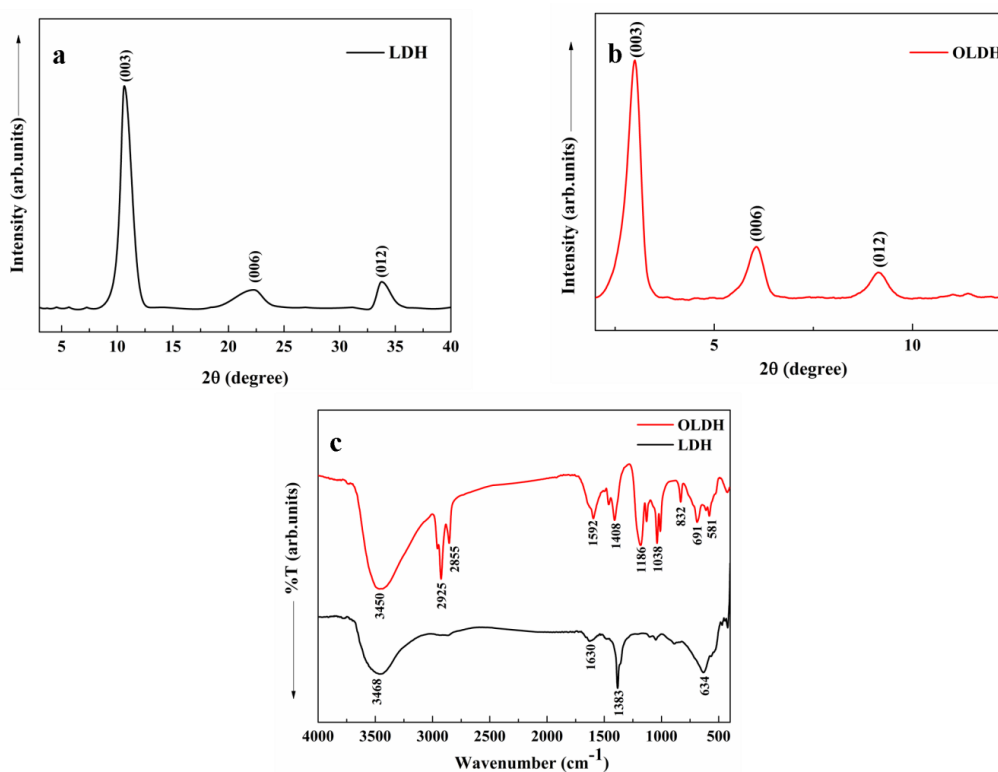


Fig.3.1 XRD pattern of: a) LDH, and b) OLDH; c) FTIR spectra of LDH and OLDH.



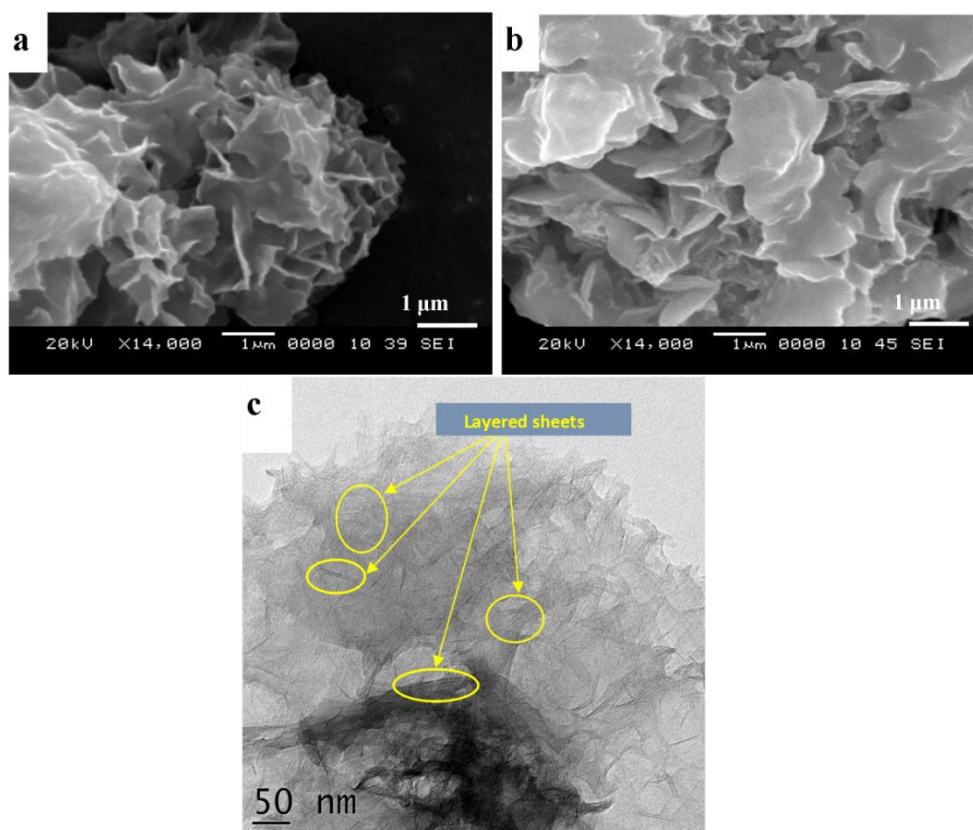


Fig.3.2 SEM micrograph of: a) LDH, and b) OLDH; c) TEM micrograph of OLDH.

### 3.1.2 Characterization of OLDH/PVDF composite nanofabrics

#### 3.1.2.1 SEM, EDS and TEM results

Fig.3.3 (a, b, c, d, and e) shows the SEM images of OLDH/PVDF nanofabrics containing varying amounts of OLDH. Incorporation of OLDH into PVDF matrix increased the charge density of electrified jet causing extended elongation of the jet during electrospinning that resulted in smoother and finer nanofibers. The fiber diameters of electrospun nanofabrics were in the range of 150-450 nm, with significant number of fibers with diameters around 220 nm (Fig.3.3f). The mean fiber diameter (MFD) and standard deviation of the fiber diameter (SD) of the E-PVDF and OLDH/PVDF nanofabrics are shown in Table 3.1. For a loading of 3 wt% OLDH, the MFD decreased to 204 nm (SD of 26), which could be attributed to the higher solution conductivity and higher stretching of the solution jet during electrospinning [Yee et al. 2007 Andrew and Clarke 2008]. The MFD and SD for OLDH/PVDF nanofabrics increased with the content of OLDH, which was due to the aggregation of

filler particles. The EDS elemental mapping of the nanofabric (with OLDH loading of 3 wt%) confirmed the presence of OLDH and its uniform dispersion in the PVDF matrix (Fig.3.4).

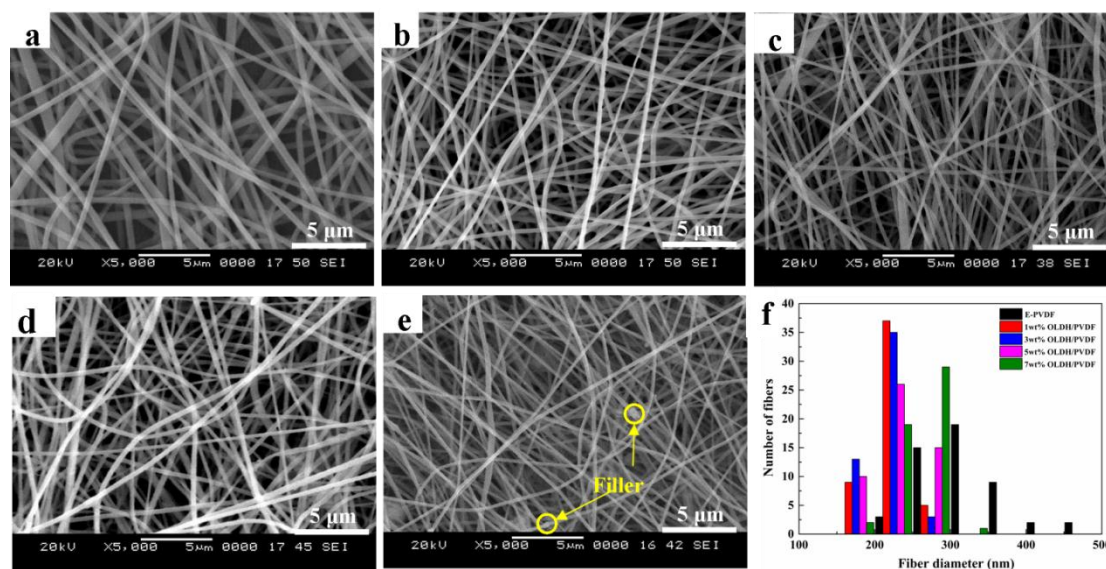


Fig.3.3 SEM micrographs of electrospun OLDH/PVDF nanofabrics with varying OLDH content: (a) 0%, (b) 1%, (c) 3%, (d) 5%, (e) 7% and (f) distribution of fiber diameters of E-PVDF and OLDH/PVDF nanofabrics.

Table 3.1 MFD and SD of OLDH/PVDF nanofabrics with different contents of OLDH.

| OLDH loading (wt %) | MFD (nm) | SD (nm) |
|---------------------|----------|---------|
| 0 (PVDF)            | 326      | 51      |
| 1                   | 225      | 23      |
| 3                   | 204      | 26      |
| 5                   | 230      | 30      |
| 7                   | 250      | 32      |

Fig.3.5a and b show the TEM micrographs of E-PVDF and 3 wt% OLDH/PVDF composite nanofiber, respectively. The E-PVDF nanofiber is relatively brighter; the dark lined shades in Fig.3.5b represented OLDH filler encapsulated within PVDF matrix. Additionally, the OLDH filler was well dispersed in the PVDF

matrix and also the sheets were orientated along the fiber axis. The elongational forces offered by electrospinning possibly align the OLDH platelets in the direction of PVDF fiber axis. The uniform dispersion of OLDH filler in PVDF nanofabrics could be ascribed to the effective interaction between the hydroxyl group of OLDH and fluorine atoms of PVDF [Tian et al. 2017].

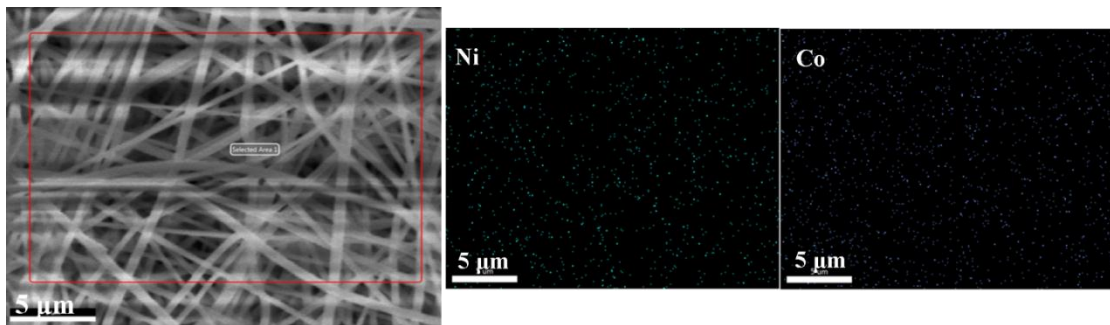


Fig.3.4 SEM-EDS elemental mapping of Ni and Co in 3wt% OLDH/PVDF nanofabrics.

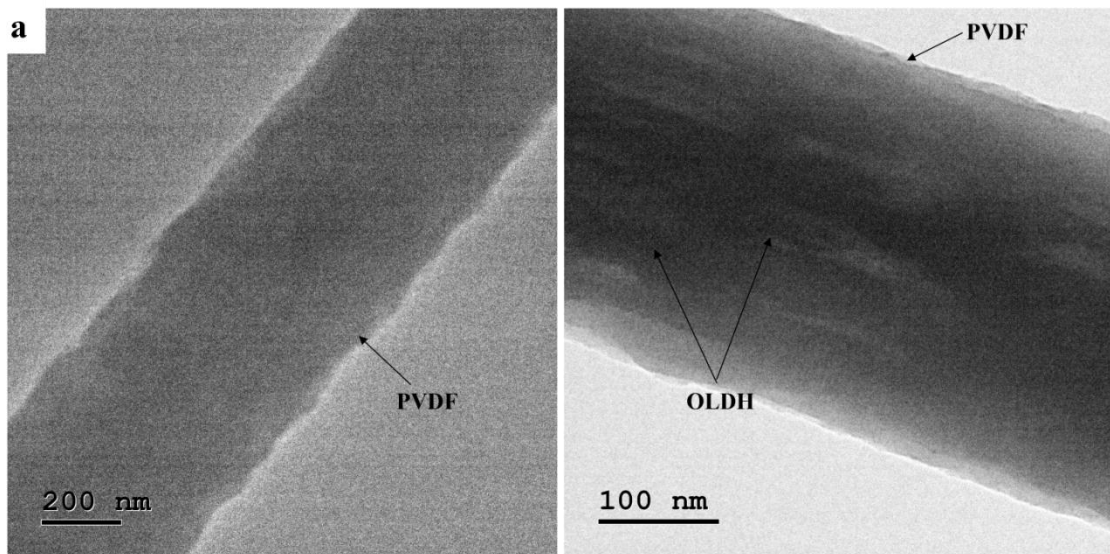


Fig.3.5 TEM images of single nanofiber of: a) E-PVDF, and b) 3 wt% OLDH/PVDF composite.

### 3.1.2.2 XRD results

Fig.3.6 depicts the XRD patterns of PVDF powder, E-PVDF, and OLDH/PVDF nanofabrics. In PVDF powder, the  $\alpha$ -phase is predominant as evidenced by the  $2\theta$  values at  $18.3^\circ$ ,  $19.9^\circ$ , and  $26.6^\circ$ , corresponding respectively to the (0 2 0), (1 1 0), and (0 2 1) reflections of  $\alpha$ -phase [Xue et al. 2017]. Notably, for E-PVDF and

OLDH/PVDF nanofabrics, the intensity of the characteristic peak of the  $\alpha$ -phase decreased, and a sharp peak was observed at  $20.6^\circ$  followed by a weaker one at  $36.3^\circ$  corresponding to (110/200) and (201) planes of the  $\beta$ -phase [Cai et al. 2017], respectively. The higher stretching and in-situ electrical poling offered by electrospinning process facilitate the transformation of non-polar  $\alpha$ -phase to the polar  $\beta$ -phase in the resultant nanofabrics. The crystallinity of E-PVDF and OLDH/PVDF nanofabrics were evaluated by a deconvolution technique [Kim et al. 2011], and the  $\chi_c$  values are given in Table 3.2. The crystallinity of nanofabrics tends to increase with OLDH loading in the PVDF matrix up to 3 wt%, beyond which it decreased. Generally, fillers play a crucial role in polymer crystallization either by providing nucleation sites or hindering the polymer chain mobility [Issa et al. 2017]. Herein, the OLDH sheets had a dual role in the crystallization of PVDF; it provided nucleation sites for crystal transition at low loading, and a higher filler concentration led to inhibition of polymer chain motions.

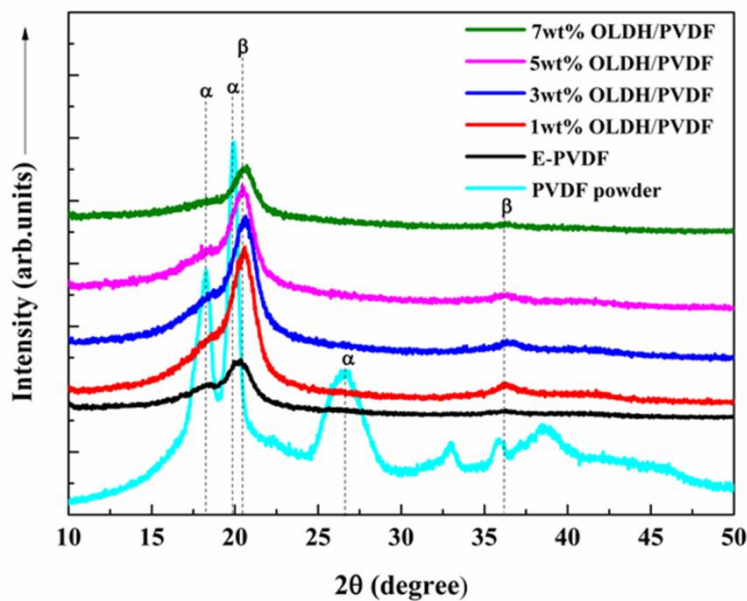


Fig.3.6 XRD patterns of PVDF powder, E-PVDF and OLDH/PVDF nanofabrics.

### 3.1.2.3 DSC results

DSC traces of E-PVDF and OLDH/PVDF nanofabrics are shown in Fig.3.7 and their corresponding melting temperature ( $T_m$ ), melting enthalpy ( $\Delta H_m$ ), and crystallinity ( $\chi_c$ ) are highlighted in Table 2. For 3 wt% OLDH/PVDF nanofabrics, the melting peak was observed at  $175.5^\circ\text{C}$  and that there was an increase in the  $T_m$  compared to

E-PVDF. The increase in  $T_m$  for the composite nanofabric can be attributed to the significant contribution from the higher melting  $\beta$ -phase [Pramoda et al. 2005]. The  $T_m$  values for OLDH/PVDF nanofabrics decrease with the loading of OLDH, possibly due to the rearrangement of the  $\alpha$ -phase in the PVDF matrix [Pramoda et al. 2005; Andrew and Clarke 2008]. The crystallinity ( $\chi_c$ ) values from DSC and XRD results (Table 3.2) are found to have a similar trend.

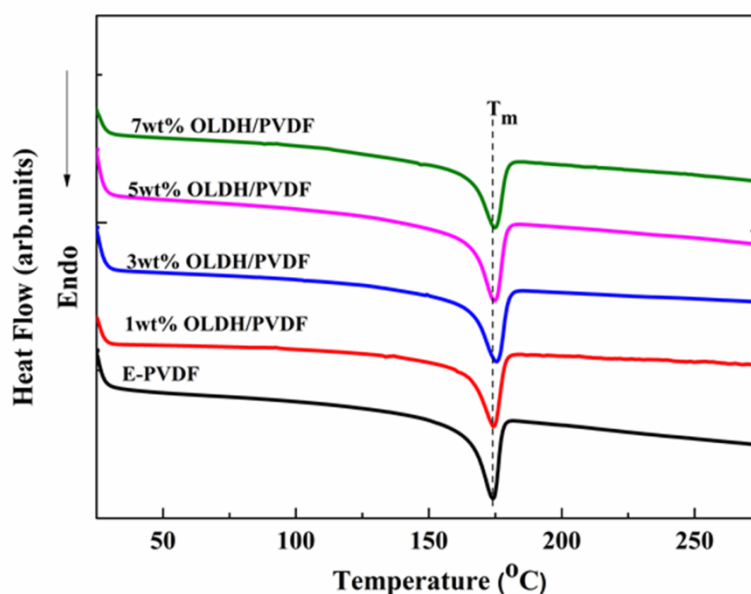


Fig.3.7 DSC traces of E-PVDF and OLDH/PVDF nanofabrics.

Table 3.2 Melting temperature, melting enthalpy, and crystallinity of E-PVDF and OLDH/PVDF nanofabrics.

| Electrospun nanofabrics | Melting temperature (°C) | $\Delta H_m$ ( $Jg^{-1}$ ) | % $\chi_c$ |      |
|-------------------------|--------------------------|----------------------------|------------|------|
|                         |                          |                            | DSC        | XRD  |
| E-PVDF                  | 174                      | 48.0                       | 45.8       | 31.2 |
| 1wt% OLDH/PVDF          | 174.3                    | 57.6                       | 55.0       | 35.4 |
| 3wt% OLDH/PVDF          | 175.5                    | 55.6                       | 53.1       | 35.3 |
| 5wt% OLDH/PVDF          | 174.8                    | 53.5                       | 51.0       | 34.6 |
| 7wt% OLDH/PVDF          | 174.3                    | 51.4                       | 49.1       | 33.7 |

### 3.1.2.4 FTIR spectroscopy

FTIR spectra of PVDF powder, E-PVDF, and OLDH/PVDF nanofabrics are shown in Fig.3.8. The spectra of PVDF powder showed stark bands at 489, 532, 614, 763, and 975  $\text{cm}^{-1}$  ascribed to the  $\alpha$ -phase, and the signature bands for the  $\beta$ -phase were evident at 840 ( $\text{CH}_2$  rocking) and 1400  $\text{cm}^{-1}$  ( $\text{CH}_2$  wagging) [Khalifa et al. 2016; Xue et al. 2017]. Addition of OLDH into PVDF nanofabrics significantly reduced the intensity of the  $\alpha$ -phase bands and promoted a new band that was discernible at 1275  $\text{cm}^{-1}$  corresponding to the all trans conformation of the  $\beta$ -phase [Cai et al. 2017]. Furthermore, the distinctive infrared band of the  $\gamma$ -phase was not evident, thus suggesting that the synergistic effect of OLDH and electrospinning favors the formation of the  $\beta$ -polymorph. The  $\beta$ -phase content of E-PVDF and OLDH/PVDF nanofabrics were measured (Table 3.3). The  $\beta$ -phase content reached a maximum value of 87.8% at 3 wt% OLDH content, after which it decreased; this is possibly due to the aggregation of filler particles at a higher concentration, as supported by the SEM results.

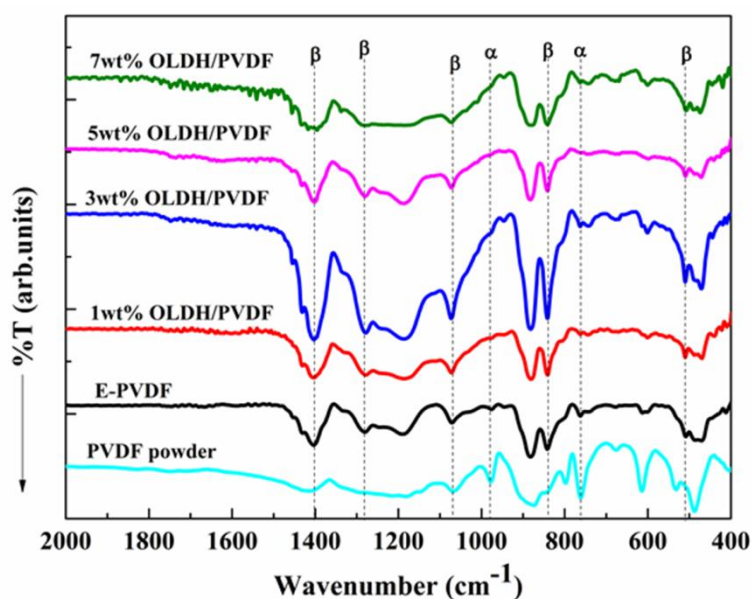


Fig.3.8 FTIR spectra of PVDF powder, E-PVDF, and OLDH/PVDF nanofabrics.

Table 3.3 FTIR results of OLDH/PVDF nanofabrics with different content of OLDH.

| OLDH content (wt %) | Absorbance intensity |                  | f( $\beta$ ) (%) |
|---------------------|----------------------|------------------|------------------|
|                     | A <sub>764</sub>     | A <sub>840</sub> |                  |
| 0                   | 0.0917               | 0.1701           | 59.5             |
| 1                   | 0.0384               | 0.1419           | 74.5             |
| 3                   | 0.0347               | 0.3147           | 87.8             |
| 5                   | 0.0278               | 0.1217           | 77.6             |
| 7                   | 0.0338               | 0.1390           | 76.5             |

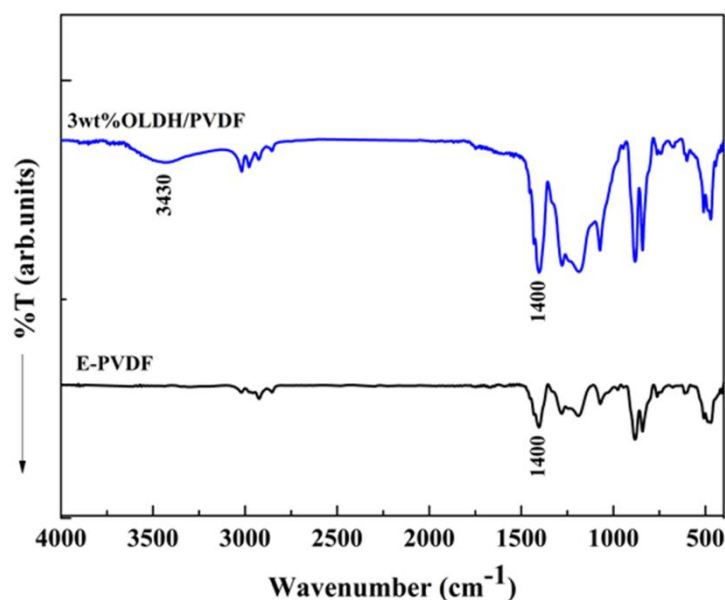


Fig.3.9 FTIR spectra of electrospun PVDF and 3 wt% OLDH/PVDF nanofabrics.

FTIR spectra in the wavenumber range of 4000-400  $\text{cm}^{-1}$  were studied to determine the possible interactions in the OLDH/PVDF nanofabrics (Fig.3.9). In comparison with E-PVDF, a broad peak at 3430  $\text{cm}^{-1}$  was observed for 3wt% OLDH/PVDF nanofabrics. Also, shifting of the peak from 3450 to 3430  $\text{cm}^{-1}$  compared with the FTIR spectrum of OLDH sample (Fig.3.1c) suggests a functional interaction between -C-F groups of PVDF and -OH groups of OLDH nanosheets. In the FTIR spectrum of 3 wt% OLDH/PVDF nanofabrics, the peak centered at 1408  $\text{cm}^{-1}$  overlaps with a peak at 1400  $\text{cm}^{-1}$  (-CH<sub>2</sub>- vibration) of PVDF. Also, shifting of

the band from 1186 to 1184  $\text{cm}^{-1}$  indicates the possible interaction between SDBS ions and  $-\text{CH}_2-$  groups of PVDF. Therefore, the effective interaction between OLDH nanosheets and PVDF chains resulted in the formation of the  $\beta$ -phase in the resultant composites. The probable interaction mechanism is depicted in Fig.3.10.

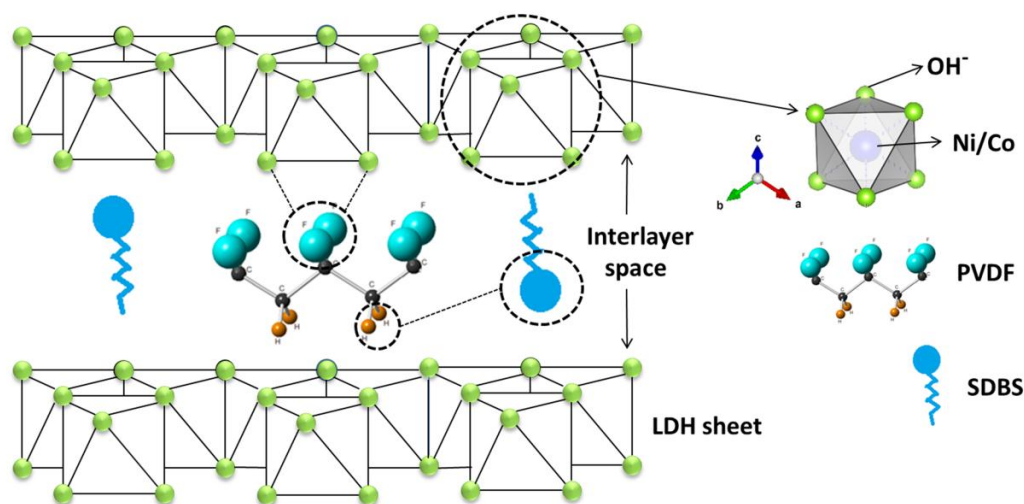


Fig.3.10 Schematic illustration of probable interactions between OLDH and PVDF in the composite nanofabrics.

### 3.1.2.5 Dielectric properties

The dielectric constants ( $\epsilon_r$ ) of E-PVDF and OLDH/PVDF nanofabrics were measured over a frequency range of 1 kHz to 1 MHz at room temperature (Fig.3.11a). Notably, there was an enhancement of  $\epsilon_r$  value for all the OLDH/PVDF nanofabrics compared to E-PVDF. The  $\epsilon_r$  values for all the nanofabrics tend to increase in the low-frequency range after which the same decreases continuously at higher frequency. This is due to the insufficient time available for the dipoles present in the nanofabrics to align themselves along the direction of the electric field at higher frequency regions. The maximum  $\epsilon_r$  value of 7.2 was achieved at 1 kHz for 7 wt% OLDH/PVDF; this was three times higher in magnitude compared with that of E-PVDF. This remarkable increase in  $\epsilon_r$  for OLDH/PVDF nanofabrics could be ascribed to the availability of free charges at the interface between the OLDH surface and PVDF chains, as related to Maxwell-Wagner-Sillars (MWS) interfacial polarization effect [Anithakumari et al. 2016; Adhikary and Mandal 2017]. The electro-active



phases of PVDF demonstrate the largest spontaneous polarization, and the porous structure of the nanofabrics vary the dipole density. Thus, the  $\beta$ -phase fraction and porosity of the electrospun nanofabrics also affect the  $\epsilon_r$  values [Yang et al. 2014].

Fig.3.11b shows the variation of dielectric loss ( $\tan\delta$ ) in E-PVDF and OLDH/PVDF nanofabrics measured as a function of frequency at room temperature. The OLDH/PVDF nanofabrics maintained low dielectric loss compared with E-PVDF. The lower dielectric loss was possibly due to the restricted mobility of the electric charges through the PVDF chains [Jahan et al. 2018]. With an improved dielectric constant and a low dielectric loss, the OLDH/PVDF nanofabrics could possibly find their application in energy devices.

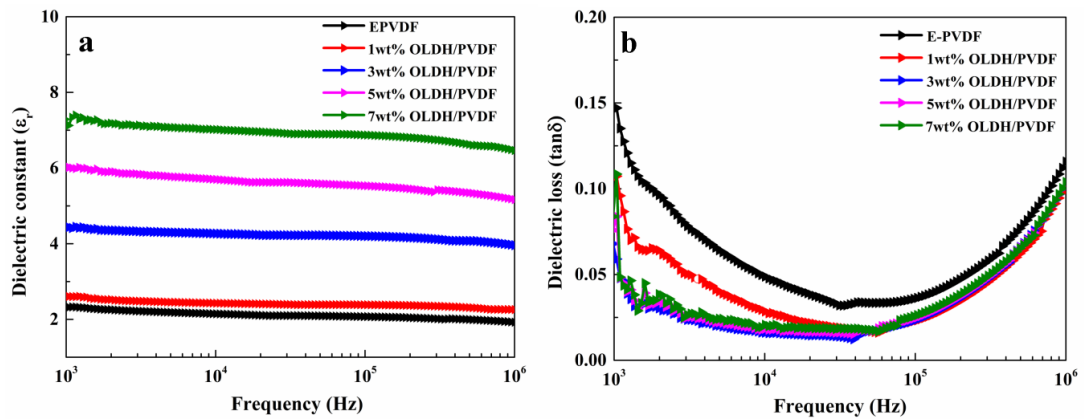


Fig.3.11 Frequency-dependent a) dielectric constant, and b) dielectric loss of E-PVDF and OLDH/PVDF nanofabrics.

### 3.1.2.6 Piezoelectric performance

The piezoelectric performance of the nanogenerator based on OLDH/PVDF nanofabrics was assessed under the repetitive compressive impact via human finger tapping mode and the corresponding output voltage as a function of OLDH content is shown in Fig.3.12a and b. Nanogenerator with E-PVDF nanofabrics produced a voltage output of 1.2 V and current output of 1.27 nA. In contrast, the presence of OLDH in PVDF nanofabrics increased the performance of the nanogenerator, reaching a peak voltage output of 6.9 V and current output of 11.78 nA for 3 wt% OLDH loading. Fig.3.13a and b demonstrates the switching polarity test for 3 wt% OLDH/PVDF nanofabrics, while no signal was generated from blank nanogenerator,

thus confirming that the output response from NG stemmed solely from the piezoelectric effect. The two signals arise from nanogenerator under the finger impact load, one due to the deformation (pressing) in the positive direction and the other from recovery (releasing) in the negative direction. This mechanism can be explained as follows: when the material is subjected to a compressive load, the resultant potential difference causes the dipoles in the material to orient along the direction of the applied force, resulting in a positive electrical signal. When the force is released, the material tends to return to its initial state, producing reversed polarity signals [Ren et al. 2016; Zhao et al. 2016]. Accordingly, the improved piezoelectric response of OLDH/PVDF nanofabrics is due to the fineness of fiber [Abbasipour et al. 2017] and dominance of the electroactive  $\beta$ -phase content.

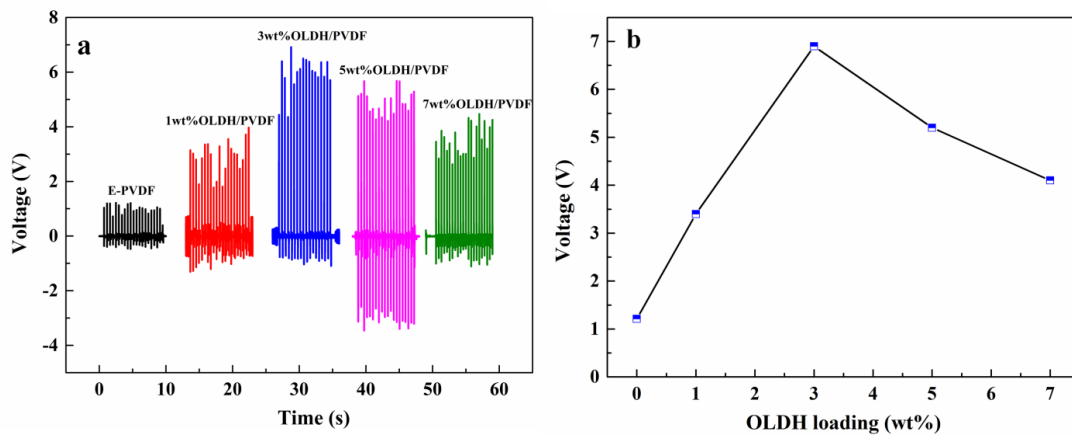


Fig.3.12 a) Variation of the piezoelectric response of E-PVDF and OLDH/PVDF nanofabrics based NG; b) The output voltage as a function of OLDH content in OLDH/PVDF nanofabrics.

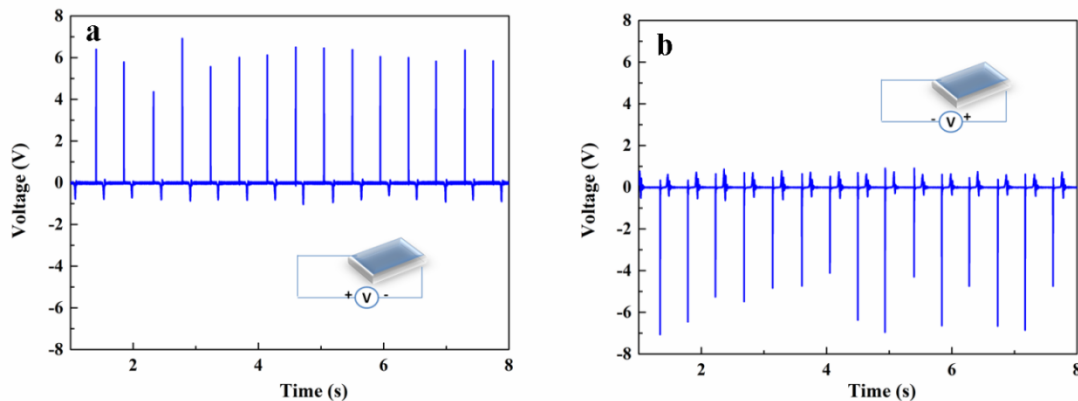


Fig.3.13 Switching polarity evaluation for 3 wt% OLDH/PVDF nanofabrics a) forward connection, and b) reverse connection.

Fig.3.14a depicts the variation of the output voltage and current from the nanogenerator as a function of load resistance (0.1-5 M $\Omega$ ) under finger tapping mode. The output voltage increases and the corresponding current values decrease with the load resistance. The power density ( $W = \frac{V^2}{R_L A}$ , where V is the voltage,  $R_L$  the load resistance and  $A = 7.5 \text{ cm}^2$ , the active area) reaches a peak value of  $0.92 \mu\text{W}/\text{cm}^2$  at a resistance of 2 M $\Omega$ , as shown in Fig.3.14b. The results of this study suggest its applicability in powering portable electronic sensors and devices.

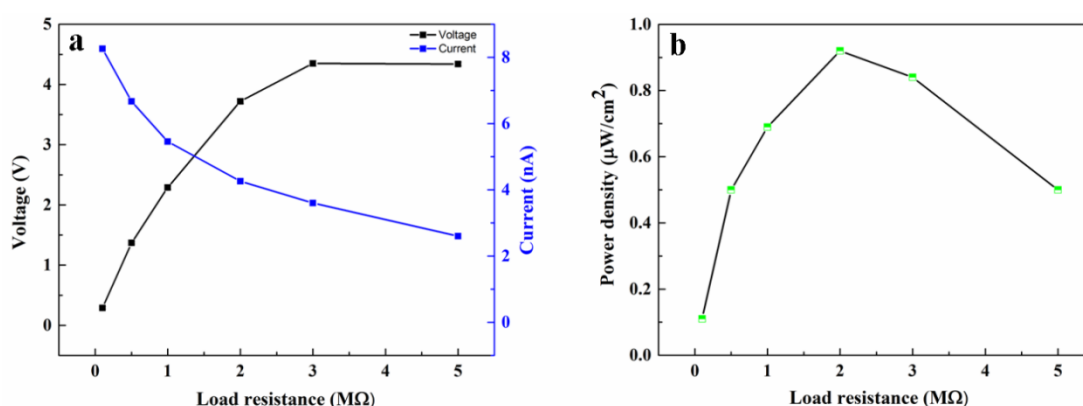


Fig.3.14 a) The output voltage and current, and b) calculated power density of 3 wt% OLDH/PVDF nanofabrics based NG across the different load resistance.

### 3.2 SUMMARY AND CONCLUSIONS

In this study, a low content of OLDH as filler resulted in the promotion of the electroactive  $\beta$ -phase in the ensuing PVDF-based electrospun nanocomposite fabrics. Also, the dielectric constant of OLDH/PVDF nanofabrics increased significantly, and dielectric loss was suppressed compared with E-PVDF. The realignment of dipoles of PVDF combined with their interfacial interaction with OLDH nanosheets resulted in an enhanced piezoelectric response of electrospun OLDH/PVDF composite nanofabrics. Flexible nanogenerator based on OLDH/PVDF nanofabrics demonstrated the maximum output voltage of 6.9 V and power density of  $0.91 \mu\text{W}/\text{cm}^2$ . Moreover, the scalability of the OLDH synthesis as well as electrospinning process could pave the way for the fabrication of viable and cost-effective nano-energy harvesting devices.



# CHAPTER 4

---

The results of this chapter have been published in *Soft Matter*, 2020, 16, 5679-5688.



## CHAPTER 4

### DEVELOPMENT OF A NEW FLEXIBLE NANOGENERATOR FROM ELECTROSPUN NANOFABRIC BASED ON PVDF/TALC NANOSHEET COMPOSITES

---

*Herein, a flexible piezoelectric nanogenerator composed of electrospun talc/PVDF composite nanofabrics has been developed. These composite nanofabrics demonstrated enhanced mechanical and piezoelectric properties compared with pristine PVDF nanofabrics. X-ray diffraction, Fourier transform infrared spectroscopy, and differential scanning calorimetry conclusively affirmed the promotion of polar  $\beta$ -phase in the talc/PVDF composite nanofabrics. The piezoelectric response of these composite nanofabrics based nanogenerator was evaluated by finger tapping and frequency modulated shaker modes delivering a maximum open-circuit voltage of 9.1 V and 8.9 V, respectively.*

#### 4.1 RESULTS AND DISCUSSION

##### 4.1.1 Morphology

Fig.4.1a shows the SEM micrographs of bead-free electrospun PVDF (E-PVDF), having the mean fiber diameter (MFD) of  $396 \pm 65$  nm. Fig.4.1b, c, d, and e display the SEM micrographs of the electrospun composite nanofabrics with different loading of talc (0.25, 0.50, 0.75, and 1 wt%). The addition of talc to the PVDF matrix led to the fiber diameter reduction of the composite nanofabrics. This decrease in fiber diameter in the presence of talc can be attributed to the enhanced charge density of the polymer solution. The polymer solution experiences shear and electrostatic forces during the electrospinning process. With the increased charge density, electrostatic force subsequently causes the jet to experience higher elongation and stretching effect leading to a reduction in MFD of the composite nanofabrics.

Talc loading of 0.50 wt% resulted in the minimum MFD, beyond which an increase in the MFD was observed. This was due to the fact that a higher concentration of talc increased the viscosity of the polymer solution, consequently reducing the mechanical stretching effect pronounced in the spinning zone. A similar phenomenon was also found in the literature data pertaining to phyllosilicate fillers [Qiu et al. 2014; Prado et al. 2015]. The SEM micrograph of talc nanoparticles (Fig.4.1f) revealed the presence of its lamellar structure.

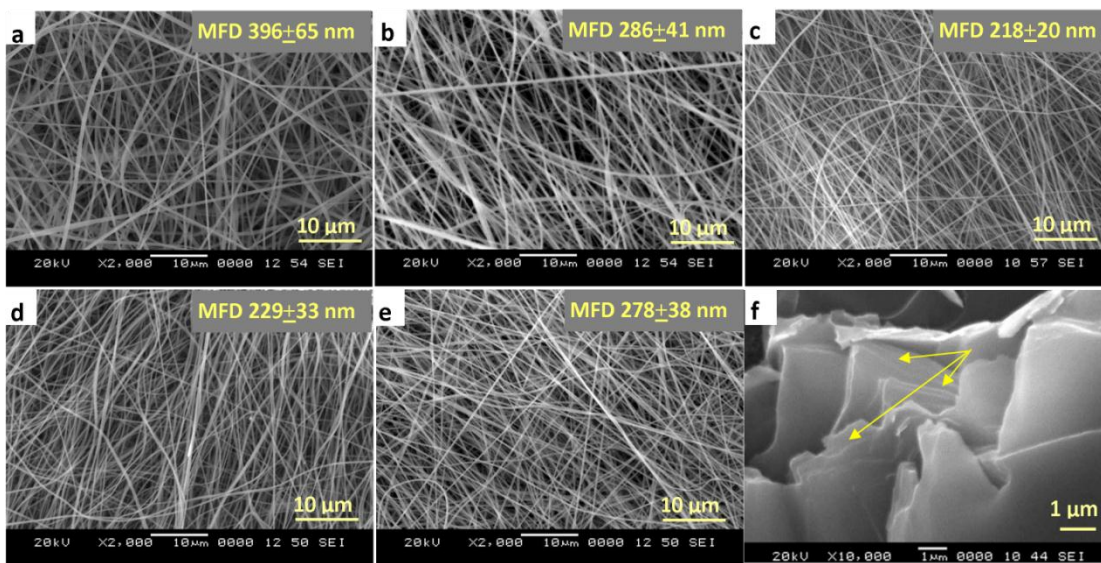


Fig.4.1 SEM micrographs of the electrospun talc/PVDF composite nanofabrics: (a) without, (b) with 0.25 wt.%, (c) with 0.50 wt.% , (d) with 0.75 wt%, and (e) with 1 wt% addition of talc in PVDF matrix ; (f) SEM micrograph of talc nanoparticles, with yellow arrows indicating the talc layers.

Fig.4.2a and b showed the TEM image of 0.50 wt% talc/ PVDF single nanofiber, and the corresponding selected area electron diffraction (SAED) pattern is depicted in Fig.4.2c. The TEM results indicate the presence and inclusion of talc filler within the PVDF nanofiber with the lattice separation of 0.168 nm in the (1 5 2) lattice plane. The lattice planes indicated by the SAED pattern of the composite nanofiber matches with the SAED pattern of talc nanoparticles. Also, the talc layers are mostly oriented along the fiber axis of the composite nanofibers. The stretching force during electrospinning played a dominant role in the alignment of filler along the PVDF fiber axis. In addition, the elemental mapping for 0.5wt% talc/PVDF



nanofabrics (Fig.4.3) showed homogeneous dispersion of the elements Fluorine (F), Carbon (C), Oxygen (O), Magnesium (Mg), and Silicon (Si) further substantiating the uniform distribution of talc layered crystals in the PVDF nanofabrics. The hydrogen bonding interaction between talc and PVDF contributes to the excellent compatibility and dispersion of talc layered crystals within the PVDF nanofabrics.

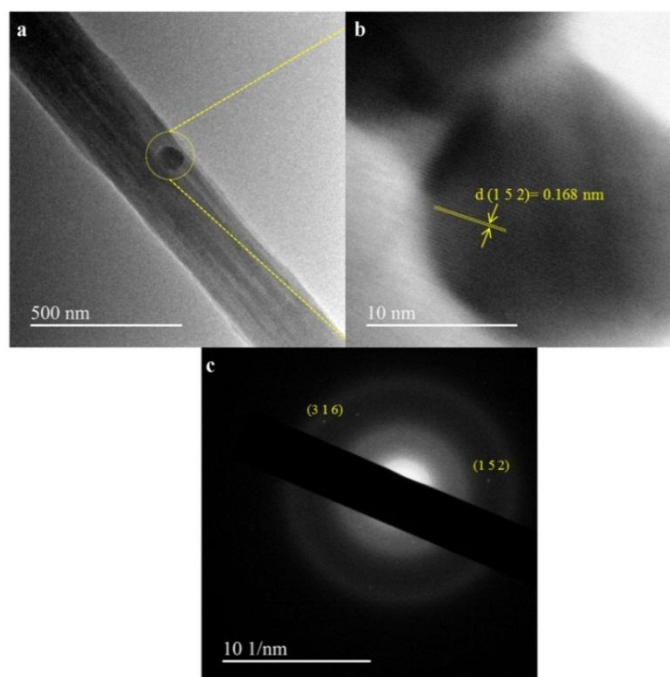


Fig.4.2 (a) TEM image of 0.50 wt% talc/PVDF single nanofiber; (b) magnified TEM image of talc nanoparticle with d-value, and (c) SAED pattern of the 0.50 wt% talc/PVDF single nanofiber.

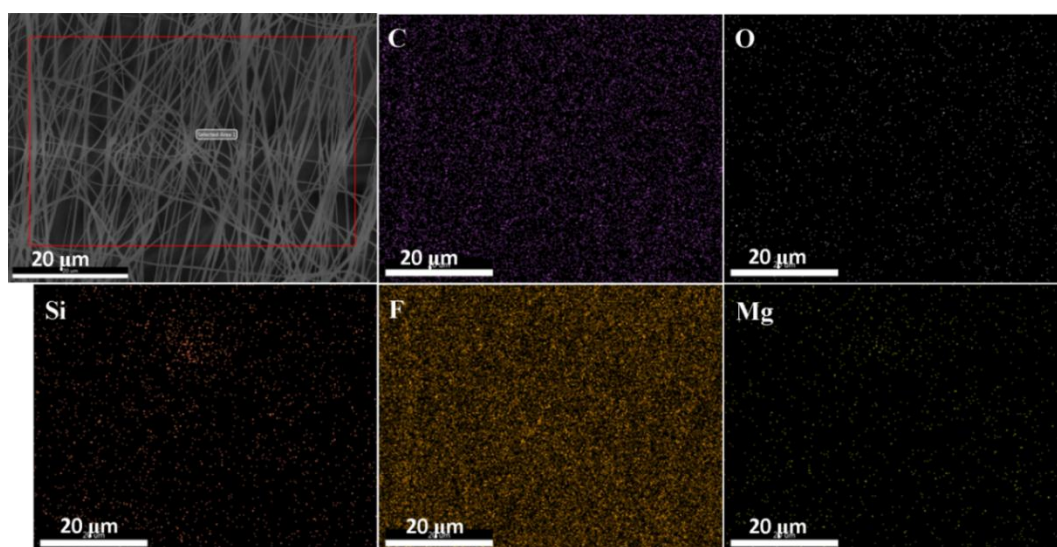


Fig.4.3 SEM micrograph and EDS elemental mapping of 0.50 wt% talc/PVDF composite nanofabrics demonstrating the distribution of carbon (C), oxygen (O), silicon (Si), fluorine (F), and magnesium (Mg) elements in the PVDF matrix.

#### 4.1.2 XRD analysis

The XRD patterns of E-PVDF and talc/PVDF composite nanofabrics are shown in Fig.4.4. The peaks of E-PVDF nanofabrics appear at  $18.4^\circ$  and  $20.6^\circ$  corresponding to the reflections of (020)  $\alpha$ -phase and (110/200)  $\beta$ -phase, respectively [Cai et al. 2017]. These indicate the coexistence of  $\alpha$  and  $\beta$ -phase in the E-PVDF nanofabrics. The introduction of talc in the PVDF matrix led to a decrease in the representative peak intensity of  $\alpha$ -phase and subsequent enhancement of  $\beta$ -phase in the ensuing composite nanofabrics. Moreover, the talc/PVDF composite nanofabrics showed an additional weak peak at  $36.3^\circ$ , which corresponds to the reflection of (201)  $\beta$ -phase [Esterly and Love 2004]. The result indicates a remarkable promotion of electroactive  $\beta$ -phase by the addition of talc to the PVDF matrix. This can be attributed to the nucleation sites offered by the surface of talc nanolayers for the  $\beta$ -crystallinity. The two peaks at  $9.4^\circ$  (002) and  $28.6^\circ$  (006) observable in talc/PVDF composite nanofabrics are in accordance with the XRD data of talc (ICDD-013-0558).

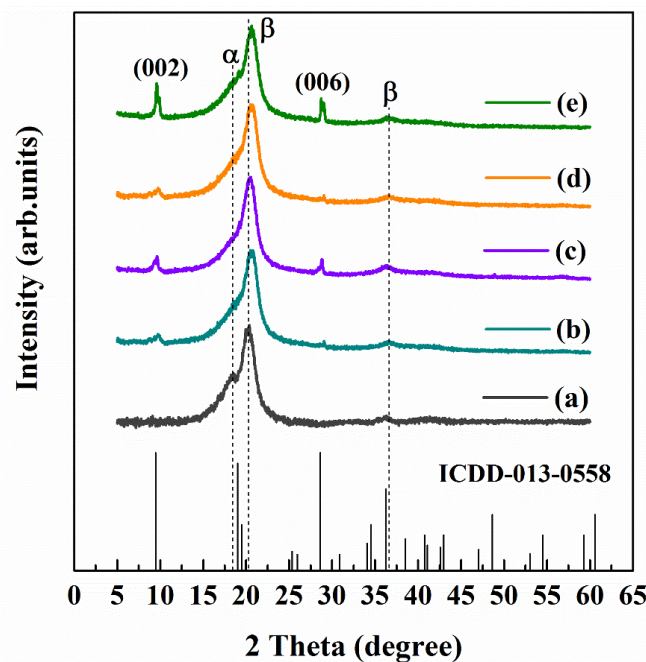


Fig.4.4 XRD patterns corresponding to (a) E-PVDF, (b) 0.25 wt% talc/PVDF, (c) 0.50 wt% talc/PVDF, (d) 0.75 wt% talc/PVDF, and (e) 1 wt% talc/PVDF composite nanofabrics.

#### 4.1.3 FTIR analysis

FTIR spectra of E-PVDF and talc/PVDF composite nanofabrics are presented in Fig.4.5. For composite nanofabrics, the dominance of  $\beta$ -phase is evident from the distinctive bands appearing at 840, 1071, 1176, 1275, and 1401  $\text{cm}^{-1}$  [Ramasundaram et al. 2008; Cai et al. 2017]. Furthermore, the  $\alpha$ -phase characteristic bands diminished, and exclusive bands of  $\gamma$ -phase (811 and 1234  $\text{cm}^{-1}$ ) were also not apparent [Cai et al. 2017], thus, suggesting the coexistence of weak  $\alpha$  and dominant  $\beta$ -phases in the composite nanofabrics. Compared with E-PVDF, the characteristic bands of  $\alpha$ -phase weakens with the increment of talc content in composite nanofabrics.

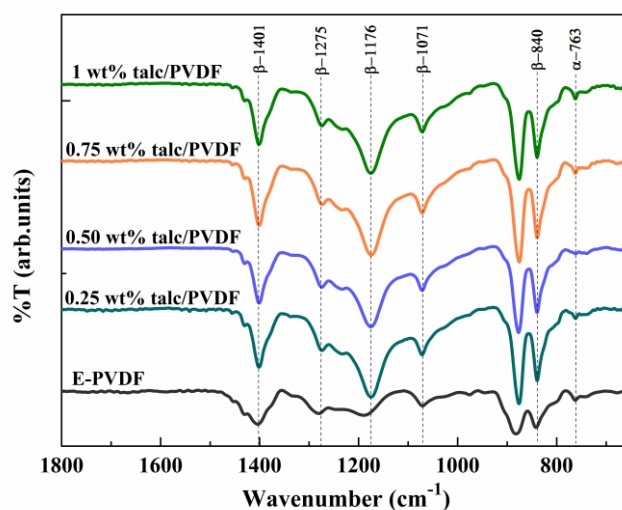


Fig.4.5 FTIR spectra of E-PVDF and talc/PVDF composite nanofabrics.

The percentage fraction of the  $\beta$ -phase ( $F(\beta)$ ) values for electrospun nanofabrics are highlighted in Table 4.1. For E-PVDF,  $F(\beta)$  is 60.4%. In contrast,  $F(\beta)$  in composite nanofabrics increases with the addition of talc concentration up to 0.50 wt% and attains a maximum value of 89.6%; after that, it decreases. Synergistic interaction between the filler particles and PVDF chains facilitates the all-trans (TTTT) conformation of PVDF, resulting in enhanced  $\beta$ -phase. Furthermore, to reveal the possible interactions between talc nanoparticles and PVDF, FTIR spectra of E-

PVDF, talc nanoparticles, and 0.50 wt% talc/PVDF nanofabrics were probed (Fig.4.6). In the spectrum of talc, the sharp band at  $3676\text{ cm}^{-1}$  was due to the Mg-OH stretching vibration, and band at  $1017\text{ cm}^{-1}$  was attributed to the Si-O-Si stretching vibration [Beattie et al. 2014]. Additionally, the peak at  $669\text{ cm}^{-1}$  is regarded as the stretching vibration of Si-OH [Morsy 2017]. In comparison to the spectrum of E-PVDF, a broad peak at  $3456\text{ cm}^{-1}$  was observed in the spectrum of 0.50 wt% talc/PVDF nanofabrics corresponding to the stretching vibrations of hydroxyl groups present in talc. In the E-PVDF spectrum, the bands appearing at  $1280$  and  $1189\text{ cm}^{-1}$  attributed to the vibration of  $-\text{CF}_2$  groups evidenced a shift to  $1278$  and  $1187\text{ cm}^{-1}$  in the spectrum of 0.50 wt% talc/PVDF nanofabrics. This peak shift is indicating a possible interaction between the  $-\text{OH}$  groups of talc and  $-\text{CF}_2$  groups of PVDF matrix via hydrogen bonding. This is driven by the affinity displayed by hydroxyl groups ( $-\text{SiOH}$  and  $-\text{MgOH}$ ) of the filler towards the electronegative fluorine atoms of PVDF, thereby contributing to the orientation of dipoles in PVDF matrix and subsequently favoring the  $\beta$ -phase conformation. A proposed interaction mechanism between talc nanosheets and PVDF in the composite nanofabric is shown in Fig.4.7.

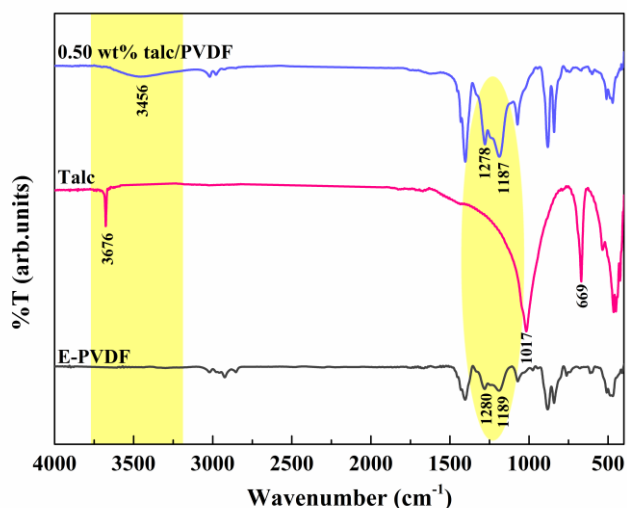


Fig.4.6 FTIR spectra of E-PVDF, talc, and 0.50 wt% talc/PVDF composite nanofabrics with yellow shades indicating the possible interactions between talc and PVDF chains.

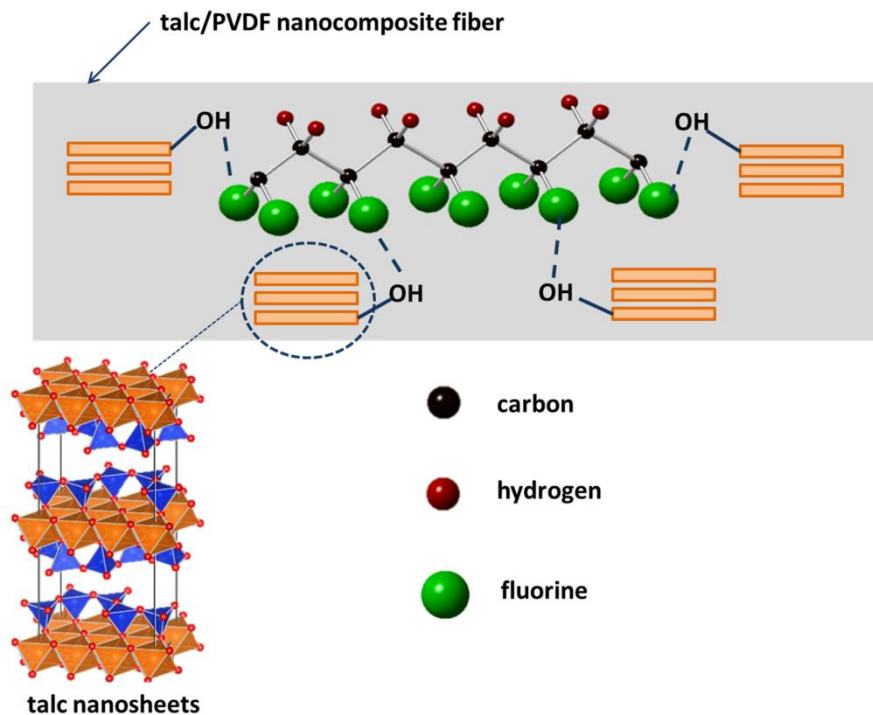


Fig.4.7 Proposed interacting mechanism in the talc/PVDF composite nanofabric.

#### 4.1.4 TGA analysis

TGA and derivative thermogravimetry (DTG) curves were analyzed to evaluate the thermal stability of E-PVDF and talc/PVDF composite nanofabrics, and their related traces are presented in Fig.4.8a and b. TGA traces of E-PVDF nanofabrics showed one-step decomposition with significant weight loss observed in the temperature range of 430-490 °C. The decomposition mechanism observed in E-PVDF nanofabrics involves the scission of carbon-hydrogen bond leading to the formation of hydrogen fluoride, followed by further loss of hydrogen fluoride along the polymer chains [Botelho et al. 2008]. The inclusion of talc in the PVDF matrix led to the increase in the onset degradation temperature of talc/PVDF composite nanofabrics in comparison to E-PVDF, as evidenced in Fig.4.8a. The first derivative peak temperature of E-PVDF was 476 °C, while talc/PVDF composite nanofabrics with 0.25, 0.50, 0.75, and 1 wt % of talc in PVDF matrix displayed 482 °C, 485 °C, 486 °C, and 485 °C, respectively (Fig.4.8b). The improved thermal stability of talc/PVDF nanofabrics in comparison to E-PVDF was possibly due to the; Tortuous path imposed by the talc sheets in the matrix and the interaction of talc sheets with PVDF

chains leading to the retardation of the diffusion of volatile products during the degradation of the polymer matrix. A similar effect has been reported in the literature, wherein thermally stable synthetic talc incorporated polymer composites demonstrated an improvement in thermal stability as compared to the virgin polymer matrix [Prado et al. 2015].

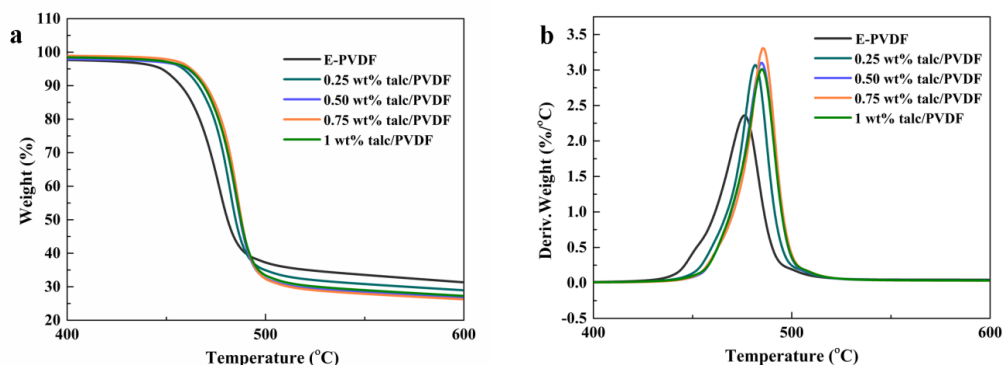


Fig.4.8 (a) TGA traces; and (b) DTG plots of E-PVDF and talc/PVDF composite nanofabrics.

#### 4.1.5 DSC analysis

Fig.4.9a and b show the DSC plots of E-PVDF and talc/PVDF composite nanofabrics. Both, the crystallization temperature ( $T_c$ ) and melting temperature ( $T_m$ ) for composite nanofabrics increased in the presence of talc in the PVDF matrix. For E-PVDF, the  $T_c$  and  $T_m$  are 141.5°C and 173.2°C, respectively. However, for talc composite nanofabrics, the  $T_c$  and  $T_m$  increased, reaching maximum values of 143.4°C and 174.3°C, respectively (Table 4.1). This increment in  $T_c$  and  $T_m$  is ascribed to the nucleation sites offered by the talc layered crystals for the crystallization process. Further, talc layered crystals restricted the mobility of PVDF chains, resulting in a shift in  $T_c$  and  $T_m$  to lower values for above 0.5wt% talc concentration in the nanofabrics.

DSC is a complementary technique to XRD and FTIR for the identification of polymorphs of PVDF, as the melting temperatures of  $\alpha$  and  $\beta$  crystallites overlap. The presence of  $\gamma$ -phase in nanofabrics was not reflected in FTIR; also, the melting temperature of  $\gamma$ -phase ( $\geq 179^\circ\text{C}$ ) was not evident in DSC traces [Gregorio 2006]. This observation suggests the absence of  $\gamma$ -phase in the composite nanofabrics. The

conclusive results from DSC, XRD, and FTIR indicate the enhancement of polar  $\beta$ -phase in the talc/PVDF composite nanofabrics.

Table 4.1 % $\beta$ -phase content, crystallization temperatures, and melting temperatures of E-PVDF and talc/PVDF composite nanofabrics.

| Sample             | % $\beta$ -phase | $T_c$ ( $^{\circ}\text{C}$ ) | $T_m$ ( $^{\circ}\text{C}$ ) |
|--------------------|------------------|------------------------------|------------------------------|
|                    | FTIR             | DSC                          | DSC                          |
| E-PVDF             | 60.4             | 141.5                        | 173.2                        |
| 0.25 wt% talc/PVDF | 84.9             | 142.8                        | 173.9                        |
| 0.50 wt% talc/PVDF | 89.6             | 143.4                        | 174.3                        |
| 0.75 wt% talc/PVDF | 84.2             | 143.2                        | 174.2                        |
| 1 wt% talc/PVDF    | 82.1             | 142.7                        | 173.5                        |

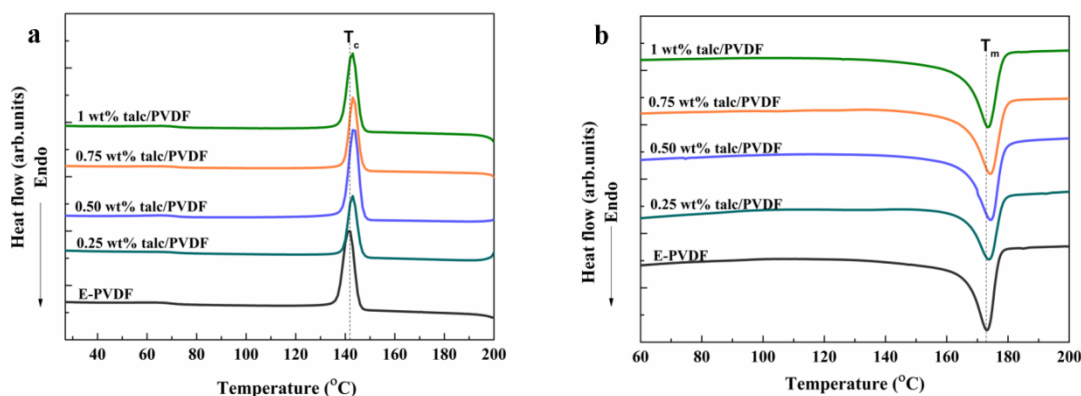


Fig.4.9 DSC traces of E-PVDF and talc/PVDF composite nanofabrics: (a) first cooling cycle, (b) second heating cycle.

#### 4.1.6 Tensile properties

Fig.4.10a demonstrates the tensile stress-strain behavior of E-PVDF and talc/PVDF electrospun composite nanofabrics, with their mechanical properties illustrated in Fig.4.10b. The inclusion of talc up to 0.50 wt% in the PVDF matrix led to the increased tensile strength and Young's modulus compared to E-PVDF. This is attributed to the good dispersion and interfacial interaction between the talc and PVDF matrix, as evidenced by the EDS-elemental mapping of and FTIR analysis of the composite nanofabrics. Also, the rigid platy talc filler restricts the mobility of

PVDF chains in the matrix. The type of filler, its dispersion, and interaction with the polymer matrix plays a vital role in tuning the mechanical properties of the resultant composites. The composite nanofabrics with 0.75 wt% and 1 wt% talc exhibited lower tensile strength and moduli. The decrement in mechanical properties at higher loading of talc is possibly due to the aggregation of filler particles, resulting in poor adhesion between the filler and polymer matrix. A similar trend was observed with other nucleating agent such as nanoclay in the PVDF matrix [Peng et al. 2009; Gaur et al. 2019]. Furthermore, the filler-filler contact increases and filler-polymer interaction in the composite nanofabrics decreases, thereby impeding the load transfer efficiency.

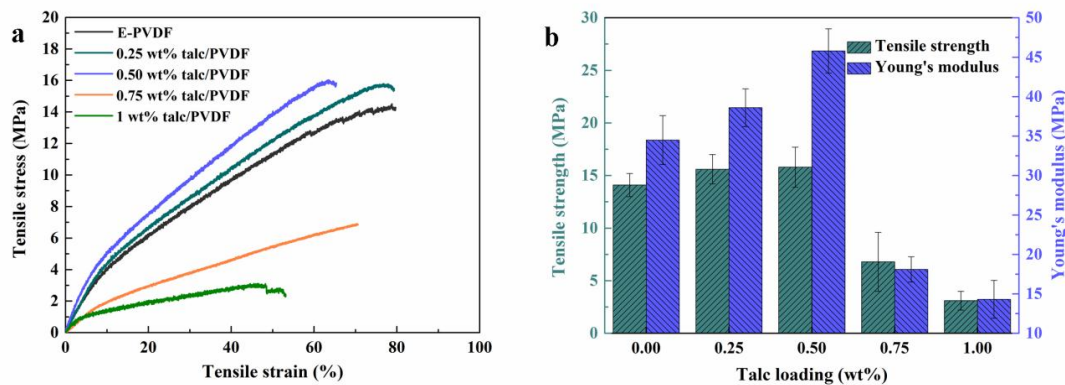


Fig.4.10 (a) Tensile stress-strain curve; and (b) Tensile strength, and Young's modulus as a function of talc loading in the PVDF matrix.

#### 4.1.7 Piezoelectric evaluation

The piezoelectric response of the E-PVDF and talc/PVDF composite nanofabrics were evaluated by subjecting the nanogenerator based electrospun nanofabrics (Fig.2.2) to two modes of excitation; finger tapping mode and frequency modulated-shaker mode. In the finger tapping mode, a compressive load in the vertical direction was applied on the nanogenerator based electrospun nanofabrics, and their corresponding output responses were recorded. When a repetitive compressive force imparts the nanogenerator surface, changes in polarisation takes place, resulting in the potential difference between the top and bottom electrodes of the nanogenerator. Thus, a positive voltage peak is produced. Furthermore, upon the release of the compressive force, a negative voltage is displayed due to the release of accumulated charges at the electrodes of the nanogenerator. Additionally, the switching polarity



test was done to confirm that the output voltage was engendered solely from the piezoelectric effect.

Fig.4.11a and b display the output voltage for E-PVDF and talc/PVDF composite nanofabrics under repeated finger tapping method. As evidenced, the output voltage of E-PVDF was 1.6 V, whereas the 0.50 wt% talc/PVDF nanofabrics demonstrated a maximum of 9.1 V. The corresponding output current of the E-PVDF was 1.4 nA and 0.50 wt% talc/PVDF composite nanofabrics reached a maximum of 16.5 nA. The higher  $\beta$ -phase content and homogeneous distribution of filler in the PVDF matrix led to the enhanced piezoelectric response displayed by the 0.50 wt% talc/PVDF composite nanofabrics. The different loading of talc i.e at 0.75 wt% and 1 wt% in the PVDF matrix led to a decline in the output voltage. This is perhaps due to the filler agglomeration effect at higher talc loading in the PVDF matrix, causing hindrance to the nucleation of  $\beta$ -crystallinity and thereby polarizability of PVDF nanofabrics. The instantaneous power density (P) of 0.5 wt% talc/PVDF nanofabrics based nanogenerator across the external load resistance (R) ranging from 500 k $\Omega$ -5 M $\Omega$  was evaluated using the equation (4.2).

$$P = \frac{V^2}{R \times A} \quad (4.2)$$

Where V is the voltage signal observed across the R, and A is the active area (15 cm<sup>2</sup>). The output voltage signal from 0.50 wt% talc/PVDF based nanogenerator across the different load resistance was measured and depicted in Fig.4.11c. The instantaneous power density reaches a maximum of 1.12  $\mu$ W/cm<sup>2</sup> across 2 M $\Omega$  load resistance and, after that, tends to decrease.

Furthermore, the nanogenerator based on 0.50 wt% talc/PVDF nanofabrics was also subjected to mechanical vibration via frequency modulated-shaker mode (Fig.2.3). The frequency of the shaker was varied from 10 to 40 Hz, and the corresponding output response of nanogenerator over the range of vibrating frequency is depicted in Fig.4.12a. The output voltage measured increases with frequency and reaches a maximum value of 8.9 V at a vibrating frequency of 30 Hz. In addition, the maximum output voltage of electrospun composite nanofabrics with varying concentrations of talc at a vibrating frequency of 30 Hz is shown in Fig.4.12b. As evidenced, the inclusion of nanostructured talc in the PVDF matrix led to the

enhancement of the piezoelectric response of the resultant composite nanofabrics. Nanostructured talc provided nucleation sites for the  $\beta$ -crystallites of PVDF, and electrospinning led to the in situ orientation of molecular dipoles of PVDF; thus, the cooperative influence of talc and electrospinning led to the enhanced polarization of the composite nanofabrics. It is noteworthy that a very low content of talc (0.50 wt%) without any surface modification was good enough to boost the piezoelectric response of PVDF. Moreover, most of the expensive carbon-based fillers (CNT, graphene) involve cumbersome purification and functionalization routes to ensure their compatibility with the polymer matrix. Thus, the talc nanosheets benefit over the fillers as mentioned earlier.

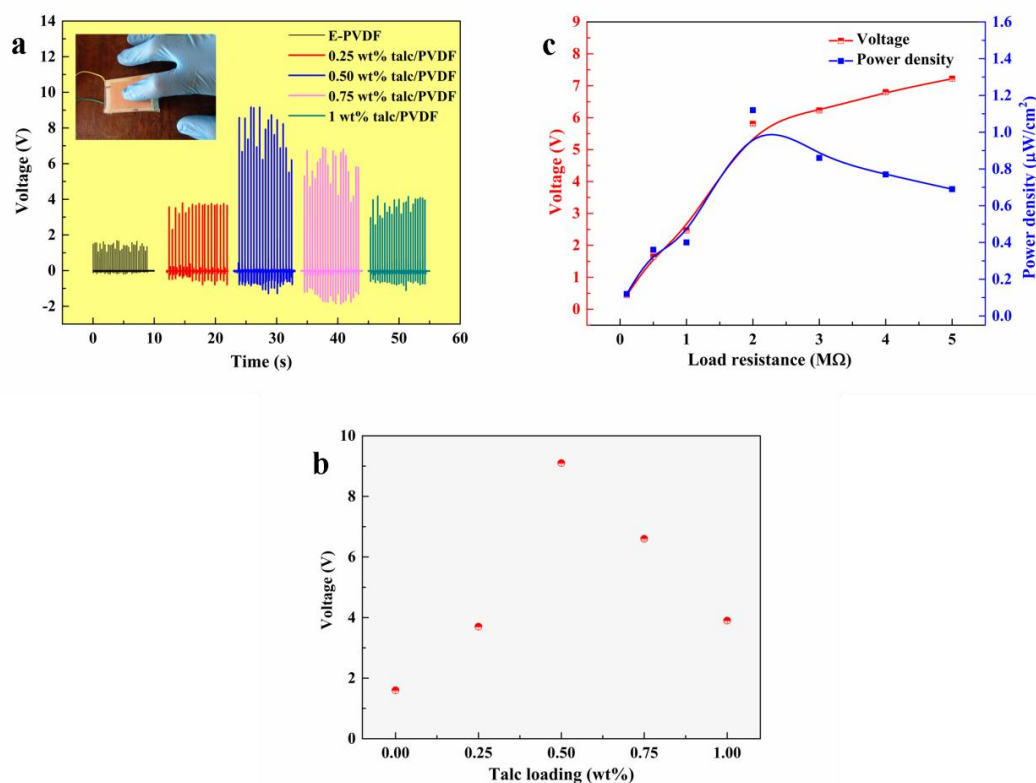


Fig.4.11 The output voltage of nanogenerator under repetitive finger imparting: (a) E-PVDF and talc/PVDF composite nanofabrics, and (b) maximum output voltage as function of talc loading in the composite nanofabrics; (c) power density of 0.50 wt% talc/PVDF fabrics across varying load resistance.

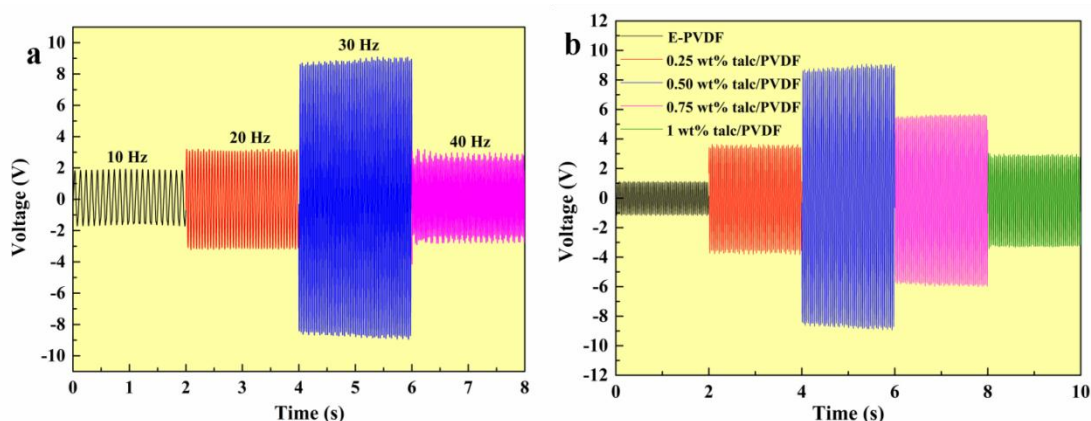


Fig.4.12 The output voltage: (a) 0.50 wt% talc/PVDF based nanogenerator at varying vibrating frequency; (b) E-PVDF and talc/PVDF composite based nanogenerator at 30 Hz vibrating frequency.

#### 4.2 SUMMARY AND CONCLUSIONS

In summary, talc/PVDF composite nanofabrics were prepared via electrospinning technique. The inclusion of nanodimensioned talc sheets in the PVDF matrix led to the promotion of polar  $\beta$ -phase. The nano-sized dimension and high aspect ratio of the talc sheets ensured their uniform dispersion and distribution in the PVDF matrix even without the necessity of any surface modification. The preferential alignment of molecular  $-\text{CH}_2/-\text{CF}_2$  dipoles during electrospinning and filler-polymer interfacial compatibility via hydrogen bonding resulted in an 89.6% polar- $\beta$  content in the talc/PVDF composite nanofabrics. Besides, the nanogenerator composed of talc/PVDF nanofabrics demonstrated a significant enhancement in its piezoelectric response compared to E-PVDF nanofabrics. The outlook of obtained results here points towards the use of these composite nanofabrics in energy harvesting applications.



# CHAPTER 5

---

The results of this chapter have been submitted to *ACS Applied Biomaterials* (*in review*).



## CHAPTER 5

# NANOSCALE MAPPING OF DOMAIN SWITCHING AND PIEZOELECTRIC COEFFICIENT OF TALC NANOSHEETS INCORPORATED PVDF NANOFIBERS BY PIEZORESPONSE FORCE MICROSCOPY

---

*This chapter discusses the electromechanical response of talc nanosheets/PVDF composite nanofibers measured by piezoresponse force microscopy. The results indicate that the composite nanofibers demonstrated ferroelectric characteristics with an improved piezoelectric response against the pristine PVDF nanofibers. Herein, the advantage of a high aspect ratio and surface charges offered by talc nanosheets alongside the electrospinning augmented the composite nanofiber's piezoelectric response.*

### 5.1 RESULTS AND DISCUSSION

#### 5.1.1 PFM analysis

The electromechanical response of the electrospun nanofibers was probed using converse piezoelectric effect under the PFM mode. In PFM, the nanofiber's local piezoelectric response is measured in terms of amplitude and phase signals. The PFM amplitude signal corresponds to the piezoelectric displacement the sample undergoes under the applied AC voltage, whereas the PFM phase signal specifies the orientation of polarization. Fig.5.1a-e and 5.2a-e showed the 3-D topography, 2-D topography with the height cross-section profile, vertical PFM amplitude, and phase images (trace and retrace) of pristine PVDF nanofiber and talc nanosheets/PVDF-0.50 nanofiber with a scanned area of  $10\ \mu\text{m} \times 10\ \mu\text{m}$ , respectively. The diameter of the nanofiber appears to be larger than the actual diameter in the PFM topographic images due to the tip convolution experienced during the measurements [Schneider et al. 2001]. Therefore, the height cross-section profile of the nanofiber measures the true diameter and accordingly indicating 320 nm and 115 nm for PVDF and talc nanosheets/PVDF-

0.50 nanofibers, respectively. The PFM phase images of talc nanosheets/PVDF-0.50 nanofiber display bright (yellow) and dark (purple) contrast regions that manifest the domain as polarized in the upward and downward directions. Meanwhile, the PFM amplitude image of PVDF nanofiber displays weaker contrast regions (bright) indicating its lower piezoelectric response in comparison with the talc nanosheets/PVDF-0.50 nanofiber.

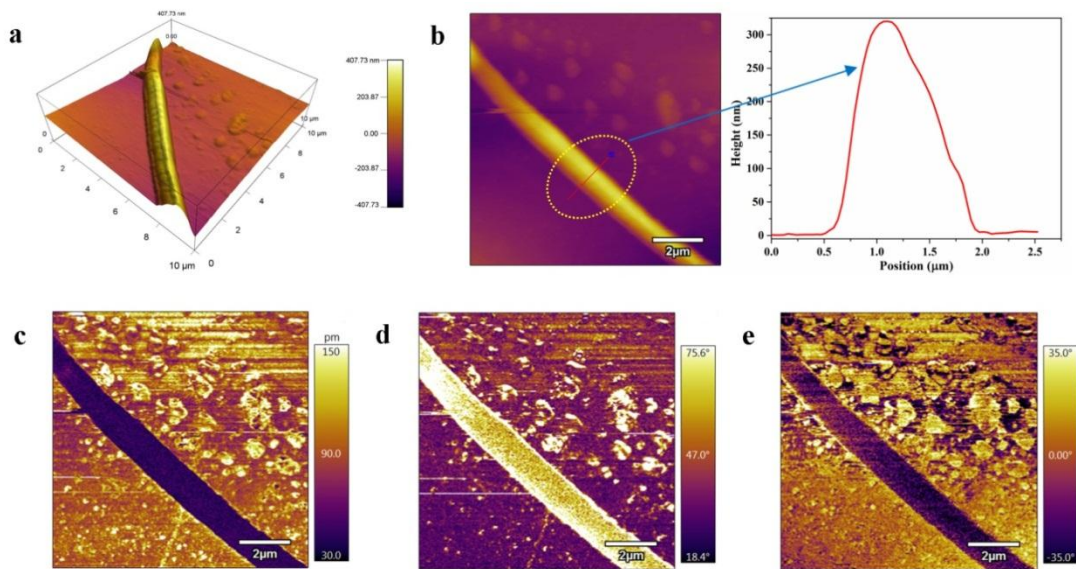


Fig.5.1 PFM images of pristine PVDF nanofiber: (a) 3-D topography image, (b) 2-D topography with the height cross-section profile, (c) amplitude image, (d) phase-1 image (trace), and (e) phase-2 image (retrace).

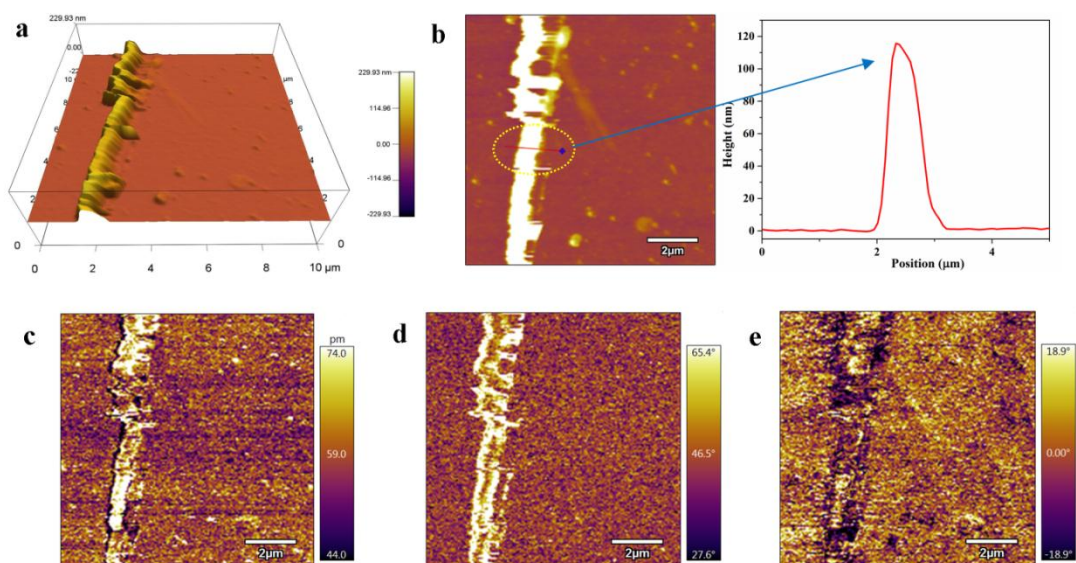




Fig.5.2 PFM images of talc nanosheets/PVDF-0.50 nanofiber: (a) 3-D topography image, (b) 2-D topography with the height cross-section profile, (c) amplitude image, (d) phase-1 image (trace), and (e) phase-2 image (retrace).

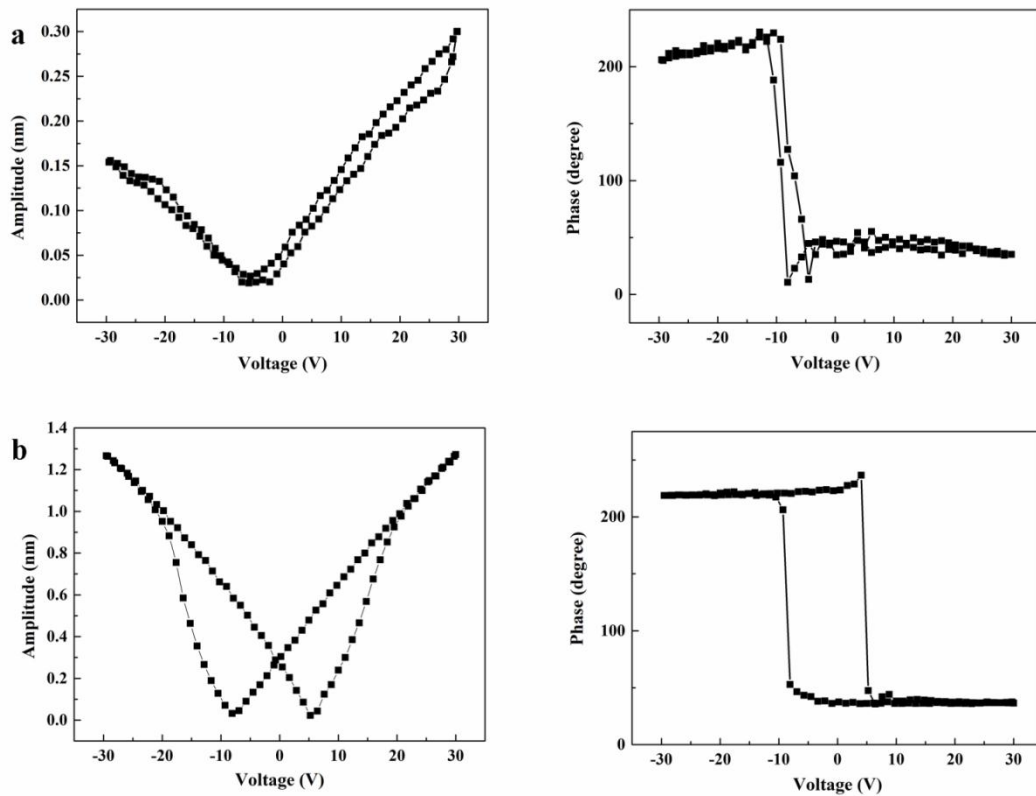


Fig.5.3 Amplitude and phase hysteresis loops of (a) PVDF nanofiber and (b) talc nanosheets/PVDF-0.50 nanofiber.

To further elucidate the nanofibers' local piezoelectric response characteristics, the amplitude strain and ferroelectric switching loops were analyzed. Under the pulsed voltage signals, a butterfly-shaped amplitude loop and rectangular-shaped phase loop were displayed by both the pristine PVDF nanofiber (Fig.5.3a) and the talc nanosheets/PVDF-0.50 nanofiber (Fig.5.3b). The domain phase curve reveals a standard  $180^\circ$  domain switching behavior, thereby supporting PVDF's ferroelectric nature in both these nanofiber systems. The domain phase response of PVDF nanofiber exhibited a hysteresis loop inclining towards the negative bias voltage. This could be ascribed to the domain wall pinning effect that suppresses the domain's switching ability or due to mechanical stress [Bhimireddi et al. 2016]. Moreover, this

also explains the asymmetry displayed in the amplitude and phase loops of talc nanosheets/PVDF-0.50 nanofiber (coercive fields of + 5 V and – 8 V). The amplitude signal tends to decrease as the applied voltage sweeps from – 30 V to 0 V (Fig.5.3b) due to the contraction of dipoles, and at + 5 V (coercive field), the domain switching happens with a 180° phase shift. With further increase in applied voltage, the amplitude signal increases due to the expansion of dipoles and reach a maximum at + 30 V. At this stage, a decrement in the applied voltage (+ 30 V to 0 V) results in the decrease in amplitude signal with antiparallel field directions to the dipoles. At a negative coercive field of – 8 V, polarizations of dipoles with 180° phase switching happen until the applied voltage reaches – 30 V.

Since the amplitude loop image is proportional to the magnitude of the piezoelectric coefficient ( $d_{33}$ ), the corresponding  $d_{33}$  values of the electrospun nanofibers were calculated using equation (5.1) [Ding et al. 2016; Gebrekrstos et al. 2018].

$$d_{33} = \frac{S}{E} \quad (5.1)$$

Where S refers to the total strain or amplitude under the applied electric field E.

From the measured PFM amplitude data, PVDF and talc nanosheets/PVDF-0.50 nanofibers recorded maximum amplitudes of 0.3 nm and 1.3 nm, respectively at  $E = 30$  V. The calculated  $d_{33}$  value of pristine PVDF nanofiber was  $10 \pm 1$  pm/V, which was substantially enhanced to  $43.3 \pm 2$  pm/V for the talc nanosheets/PVDF-0.50 nanofiber. In addition, the  $d_{33}$  values were  $18 \pm 0.5$  pm/V (talc nanosheets/PVDF-0.25),  $37.3 \pm 1$  pm/V (talc nanosheets/PVDF-0.75), and  $28.4 \pm 3$  pm/V (talc nanosheets/PVDF-1) at different loading of talc nanosheets in the PVDF nanofibers (Fig.5.4a-c). A fourfold improvement in the piezoelectric coefficient displayed by talc nanosheets/PVDF-0.50 nanofiber here could be ascribed to the reduction in fiber diameter, which in turn tunes the electroactive  $\beta$ -phase orientation or lowers the domain wall barrier [Ico et al. 2016]. The remarkable improvement in electroactive  $\beta$ -phase with a reduced fiber diameter of nanofiber has been demonstrated in our previous work [Shetty et al. 2020]. It was explained on the basis of the intermolecular hydrogen bonding between talc nanosheets and PVDF chains that led to the  $\beta$ -nucleating activity of talc nanosheets. Furthermore, the addition of

talc nanosheets into the PVDF nanofiber causes the swelling of PVDF around the filler region. Thus, it leads to the enhanced radius of gyration of PVDF, thereby facilitating the all-trans conformation of polar  $\beta$ -phase [Baji et al. 2011]. The dimensional reduction (thinner nanofiber) combined with the polar  $\beta$ -phase fraction and its orientation contributed to the talc nanosheets/PVDF nanofibers' piezoelectric efficacy.

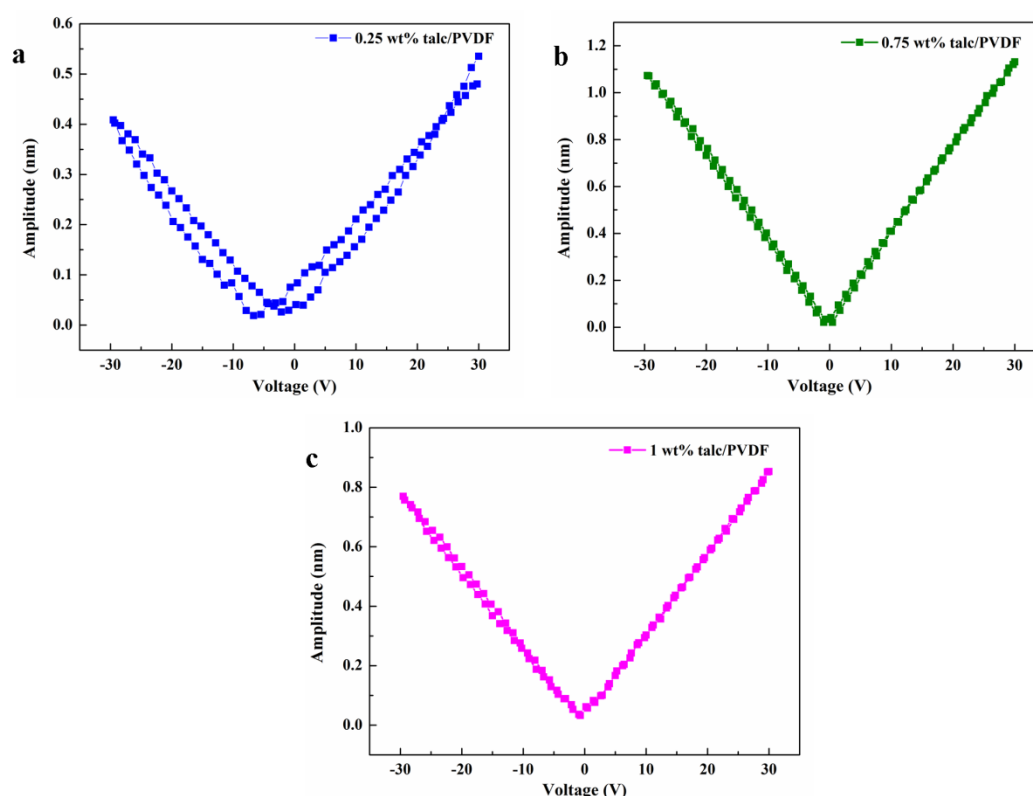


Fig.5.4 PFM amplitude loops of (a) talc nanosheets/PVDF-0.25, (b) talc nanosheets/PVDF-0.75, and (c) talc nanosheets/PVDF-1 nanofibers.

## 5.2 SUMMARY AND CONCLUSIONS

Herein, the nanoscale ferroelectric and piezoresponse characteristics of talc nanosheets/PVDF based composite nanofiber were studied by PFM. The phase domain and amplitude loops of the composite nanofiber demonstrated its local switching domain and piezoelectric responses. The incorporation and fine dispersion of a low content (0.50 wt%) of talc nanosheets in PVDF nanofiber resulted in a four-fold increase in the piezoelectric coefficient value compared to virgin PVDF

nanofiber. Synergistic effects of talc nanosheets and electrospinning accounted for the enhanced piezoresponse displayed by the composite nanofiber. In summary, the ferroelectric nature and excellent piezoelectric coefficient demonstrated by talc nanosheets/PVDF composite nanofiber is promising for its possible application in miniaturized self-powered electronic devices.

# CHAPTER 6

---

The results of this chapter have been published in *Journal of Polymer Research*, 2021, 28, 419.



## CHAPTER 6

### PIEZOELECTRIC EVALUATION OF FLEXIBLE NANOGENERATOR BASED ON ELECTROSPUN PVDF/FUNCTIONALIZED GRAPHENE/TALC NANOSHEETS HYBRID NANOCOMPOSITES

---

*Herein, a new flexible nanogenerator was developed from electrospun nanofabrics based on PVDF/carboxyl functionalized graphene nanosheets (FGNS)/talc nanosheet hybrid composite. Talc nanosheet loading was fixed at 0.50 wt% while FGNS loading was varied (0.05, 0.10, 0.15, and 0.20 wt %) in these nanofabrics and their structure-property relationship was explored. The incorporation of FGNS led to forming a conducting network in the polymer matrix that aided in the easy alignment and effective enhancement of electroactive  $\beta$ -phase PVDF. These results were affirmed by the Fourier transform infrared spectroscopy and X-ray diffraction analysis. Further, a nanogenerator composed of these hybrid composite nanofabrics was mechanically impacted using a pneumatic actuator, resulting in an output voltage of 12.9 V and a power density of 1.72  $\mu\text{W}/\text{cm}^2$ , respectively. The piezoelectric coefficient ( $d_{33}$ ) of this nanofiber system was 61 pm/V as revealed by piezoelectric force microscopy.*

#### 6.1 RESULTS AND DISCUSSION

##### 6.1.1 Characterization of carboxyl functionalized graphene nanosheets (FGNS)

The FTIR spectra of graphene oxide (GO), reduced graphene oxide (RGO), and FGNS are shown in Fig.6.1. In the spectrum of GO, the absorption peaks at 3400 and 1720  $\text{cm}^{-1}$  correspond to the O–H stretching and carboxyl C=O stretching, respectively. Further, the absorption peaks at 1228 and 1045  $\text{cm}^{-1}$  are assigned to the epoxy C–O stretching. The peak at 1620  $\text{cm}^{-1}$  is assigned to the stretching and bending vibrations of adsorbed water molecules on the GO [Nethravathi and Rajamathi 2008; Park et al. 2009; Khalili 2016; Mirza-Aghayan et al. 2016] In the spectrum of RGO the absorption peak at 1720  $\text{cm}^{-1}$  completely disappeared, and the

intensity of peak at  $1620\text{ cm}^{-1}$  is noticeably reduced. This implies a significant reduction in the oxygen functional groups of RGO. The FGNS exhibits strong absorptions at  $1555$  and  $1171\text{ cm}^{-1}$  due to the C–C stretching and C–H bending vibrations related to the aromatic benzene groups [Samsonowicz et al. 2005]. And C–O stretching vibrations of –COOH group can also possibly appear in that range. The absorption peak at  $1685\text{ cm}^{-1}$  is assigned to the C=O stretching of aromatic carboxylic acids [Coates 2006]. The peak at  $770\text{ cm}^{-1}$  is due to C–H out of plane bending vibrations in the benzene rings [Guo et al. 2017]. Moreover, the absence of a peak in the range of  $2200\text{--}2300\text{ cm}^{-1}$  corresponding to the diazonium group's  $\text{N}\equiv\text{N}$  stretching mode corroborates the grafting mechanism of benzoate on the RGO [Griffete et al. 2012].

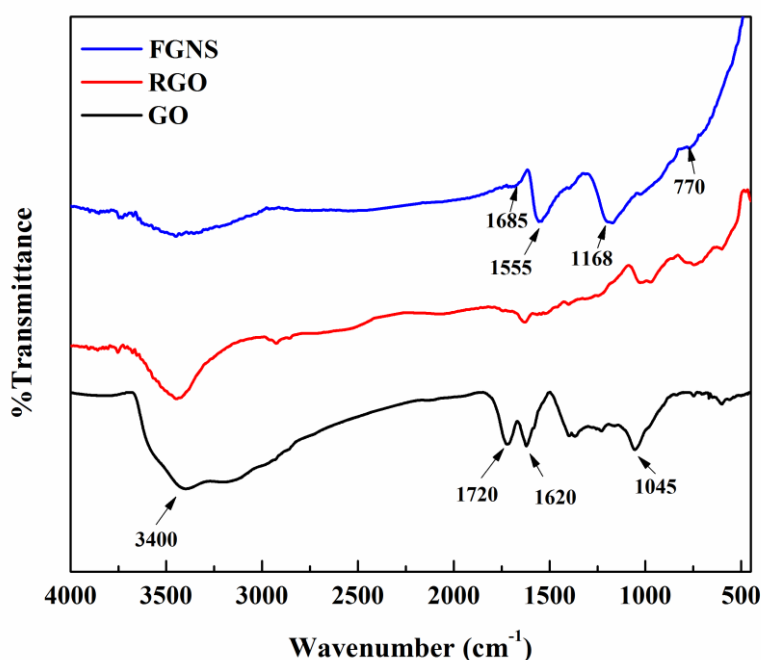


Fig.6.1 FTIR spectra of GO, RGO, and FGNS.

XRD patterns of GO, RGO, and FGNS are shown in Fig.6.2. Compared to the reference graphite diffraction pattern (ICDD-00-001-0646), GO displays a sharp peak at  $9.41^\circ$  (001) that corresponds to an interlayer space of  $0.942\text{ nm}$ . This is significantly greater as against the interlayer space of graphite ( $0.337\text{ nm}$ ) due to the intercalation of oxygen functional groups between the layers [Jiao et al. 2017]. Thermal reduction of GO results in the diffraction peaks at  $12.5^\circ$ ,  $25.20^\circ$ , and  $42.9^\circ$  that correspond to the (001), (002), and (100) crystal planes of RGO, respectively.



The weak peak at  $12.5^\circ$  (001) arises due to the remnant oxygen functional groups that were not completely eliminated during the thermal reduction process [Fu et al. 2013]. Further, the XRD pattern of RGO exhibits broadening and shifting of diffraction peak (002) to  $25.20^\circ$  with reduced interlayer space value of 0.354 nm as against the  $9.41^\circ$  (001) and 0.942 nm of GO. This reduction in the interlayer space value of RGO could be due to elimination of the most of the oxygen functional groups between the layers that subsequently led to the restacking of graphene sheets. Compared to RGO, the FGNS exhibit a broadening and marginal shift in the diffraction peak (002) from  $25.20^\circ$  to  $24.78^\circ$ . Also, the functionalization of RGO led to the introduction of additional oxygen-containing functional groups ( $-\text{COOH}$ ) on the graphene sheets that led to the increment of interlayer space value from 0.354nm (RGO) to 0.360 nm in the FGNS.

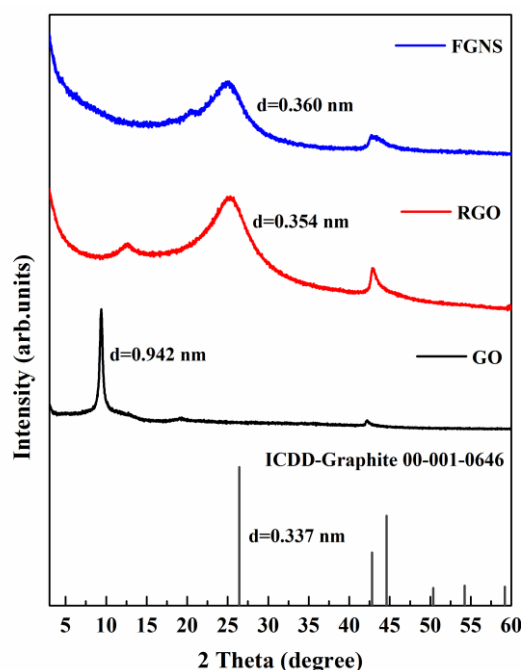


Fig.6.2 XRD patterns of GO, RGO, and FGNS.

Raman spectroscopy was used to assess the structural changes from RGO to FGNS, as shown in Fig.6.3. Raman spectra of both RGO and FGNS exhibit characteristic D and G bands. The D band arises from the breathing modes of  $\text{sp}^2$  rings and is initiated by the defects/disorders in the graphite lattice, and the G band corresponds to the first-order scattering of  $\text{E}_{2g}$  mode of  $\text{sp}^2$  carbon atoms [Behzadi et al. 2021]. The Raman spectrum of RGO exhibits the D-band at  $1346 \text{ cm}^{-1}$  and a G-

band at  $1580\text{ cm}^{-1}$ , with an intensity ratio ( $I_D/I_G$ ) of 1.22. After functionalizing RGO, the D- and G-bands were observed at  $1346\text{ cm}^{-1}$  and  $1587\text{ cm}^{-1}$ , respectively, with an intensity ratio ( $I_D/I_G$ ) of 1.18. The intensity ratio of D and G bands ( $I_D/I_G$ ) is used to measure the degree of disorder/defects. The intensity ratio ( $I_D/I_G$ ) of FGNS was lower in comparison with that of RGO. This was possibly due to the contribution of a larger amount of  $sp^2$  carbon atoms from the grafted aromatic structure of benzoate that outweighs the net amount of transformed  $sp^3$  carbon atoms in the FGNS. This functionalization of RGO does not induce any additional defects in the graphene domains. The results demonstrated here agree well with earlier literature on functionalized RGO [Zhang et al. 2012].

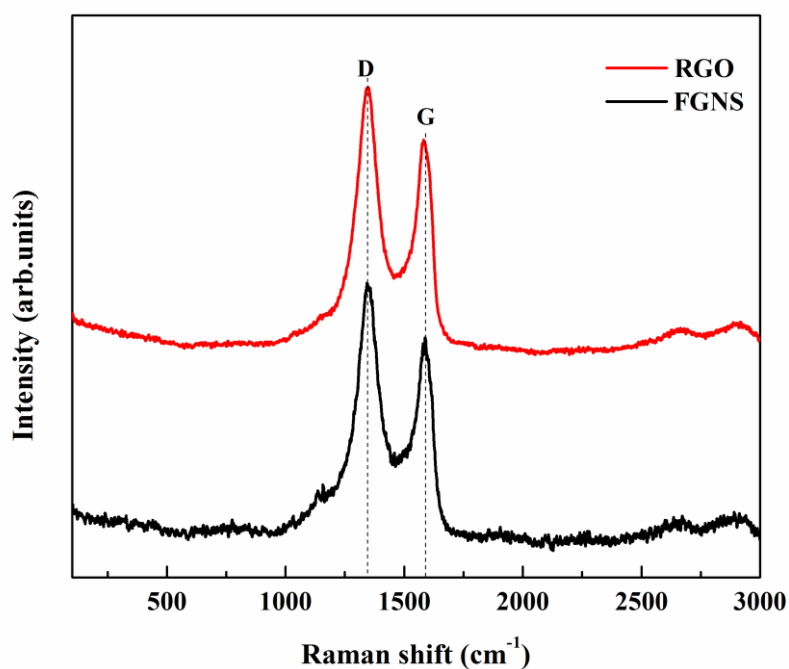


Fig.6.3 Raman spectra of RGO, and FGNS.

The surface morphological characteristics of RGO and FGNS were imaged under FESEM and are shown in Fig.6.4a and b. The micrograph of RGO displayed layered stacks of nanosheets with irregular, lightly crumpled, and folded structures that can be attributed to the intrinsic thermal stability of 2-D structured graphene (Fig.6.4a). However, the FGNS surface morphology (graphite-rose) showed the dominance of corrugated and wrinkled structure that is predominant on the edges of

the sheet, resulting from the grafting of carboxylic groups via the functionalization route (Fig.6.4b).

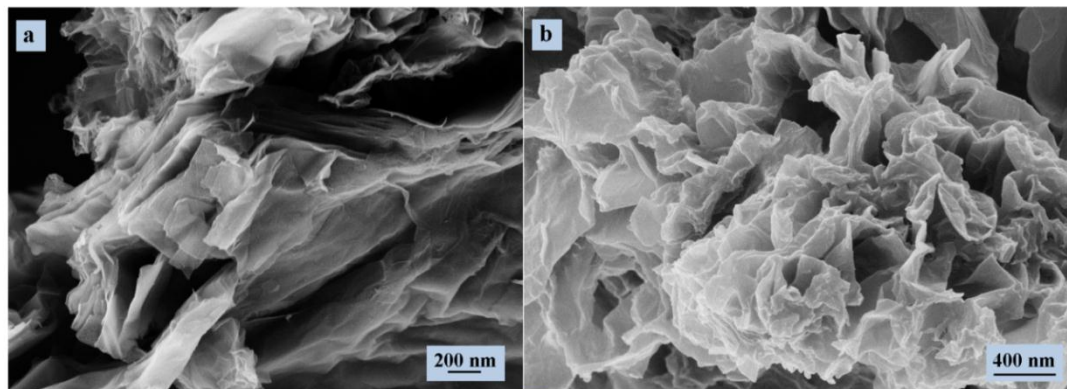


Fig.6.4 FESEM images: a) RGO and b) FGNS.

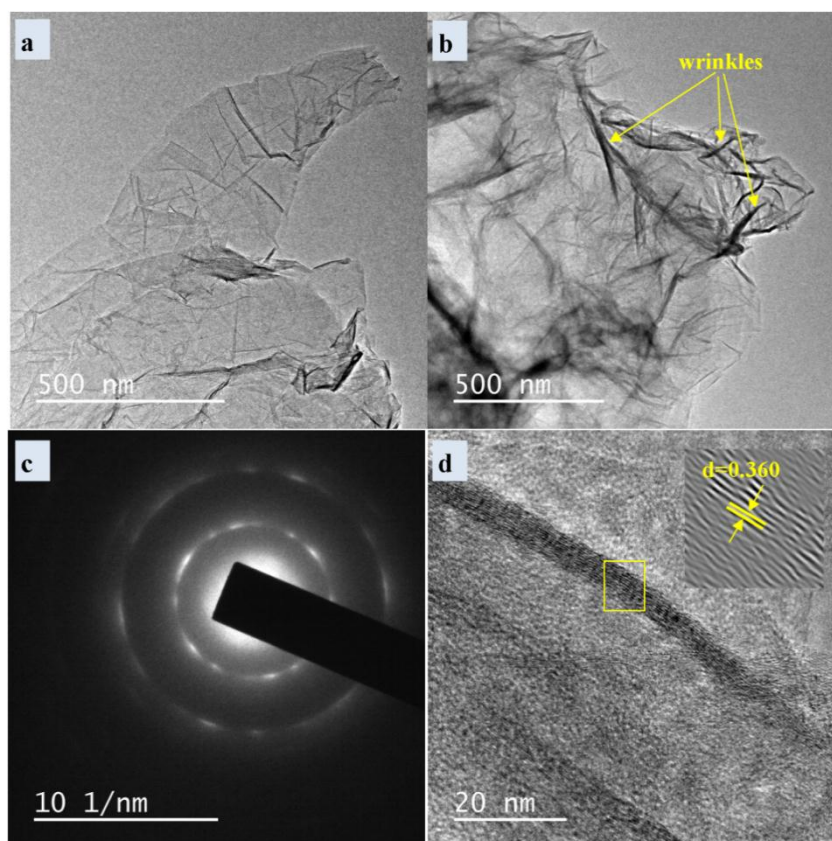


Fig.6.5 Microstructure analysis of FGNS : (a, b) TEM images with yellow arrows indicating the wrinkled structure, (c) SAED pattern, and (d) d-space value from TEM image.

This is further corroborated via TEM analysis of the FGNS that demonstrates the lamellar structure with the folding of graphene sheets (Fig.6.5a and b). The dark regions represent the crumpled structure that is formed by the stacking of several graphene nanosheets. The lateral dimensions of the nanosheets range from a few nanometers to several micrometers. The selected area diffraction pattern (SAED) of FGNS shows its polycrystalline nature (Fig.6.5c). Additionally, the lattice fringes measure the interlayer space value of 0.360 nm (that belongs to the (002) plane), which is well in agreement with the XRD results of FGNS (Fig.6.5d).

### **6.1.2 Characterization of 0.50 wt% talc nanosheets/FGNS/PVDF (TGP)-based hybrid composite nanofabrics**

#### **6.1.2.1 FESEM results**

The FESEM micrographs of TGP-based fabrics with varying FGNS content (0, 0.05, 0.10, 0.15, and 0.20 wt%) are shown in Fig.6.6a-e. Electrospun PVDF (E-PVDF) and TGP-based nanofabrics demonstrated a bead-free morphology, with E-PVDF displaying a mean fiber diameter (MFD) of  $397\pm 56$  nm. On the contrary, the TGP-based nanofabrics exhibited a reduction in MFD compared to the E-PVDF. This is attributed to the increased electrical conductivity and viscosity of the electrospinning solution in the presence of talc nanosheets and FGNS [Lee et al. 2017; Shetty et al. 2020]. Throughout electrospinning, the increased electrical conductivity of the solution causes longer stretching of the nanofibers resulting in reduced fiber diameters. While the viscosity of the solution increases, the viscoelastic forces resist the stretching of the nanofiber and lead to formation of thicker fibers. Hence, the balance between the viscoelastic and charge repulsion forces during electrospinning could significantly influence the morphology of nanofibers. As reported from the previous findings, graphene was demonstrated to improve the electrical conductivity and viscosity of the electrospinning solutions [Shi et al. 2018; Shan et al. 2019]. In the current work, the increased content of FGNS loading in TGP-based nanofabrics had a significant effect on the viscosity of the solution that contributed to the increased fiber diameters. A high magnification FESEM micrograph of TGP-0.20 based nanofiber

displayed (Fig.6.6f) a rough surface with a sheet-like texture, possibly due to the inclusion of talc nanosheets and graphene in the PVDF matrix.

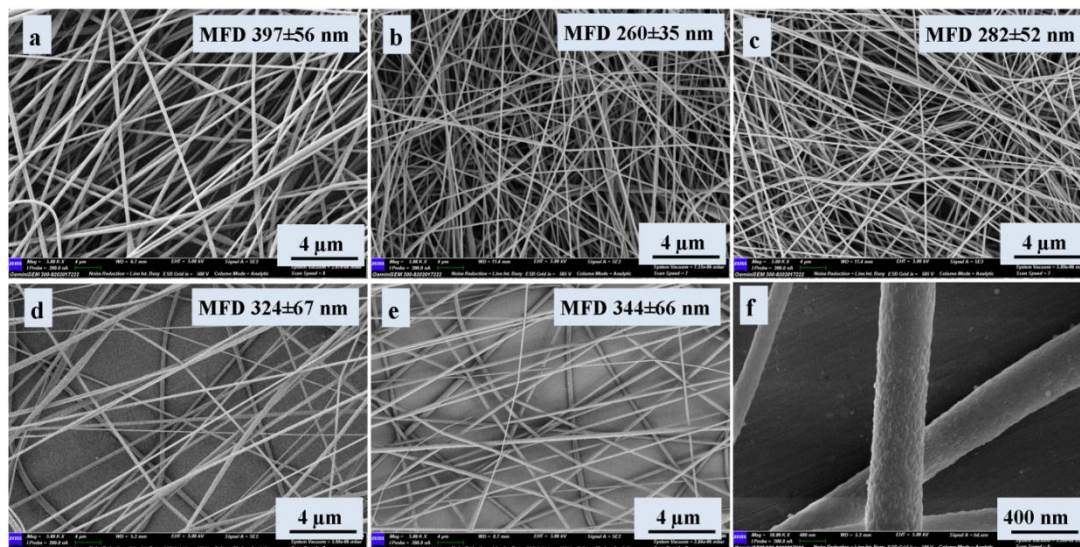


Fig.6.6 FESEM micrographs of electrospun nanofabrics: a) E-PVDF; b) TGP-0.05; c) TGP-0.10; d) TGP-0.15; e) TGP-0.20; f) high magnification FESEM image of TGP-0.20.

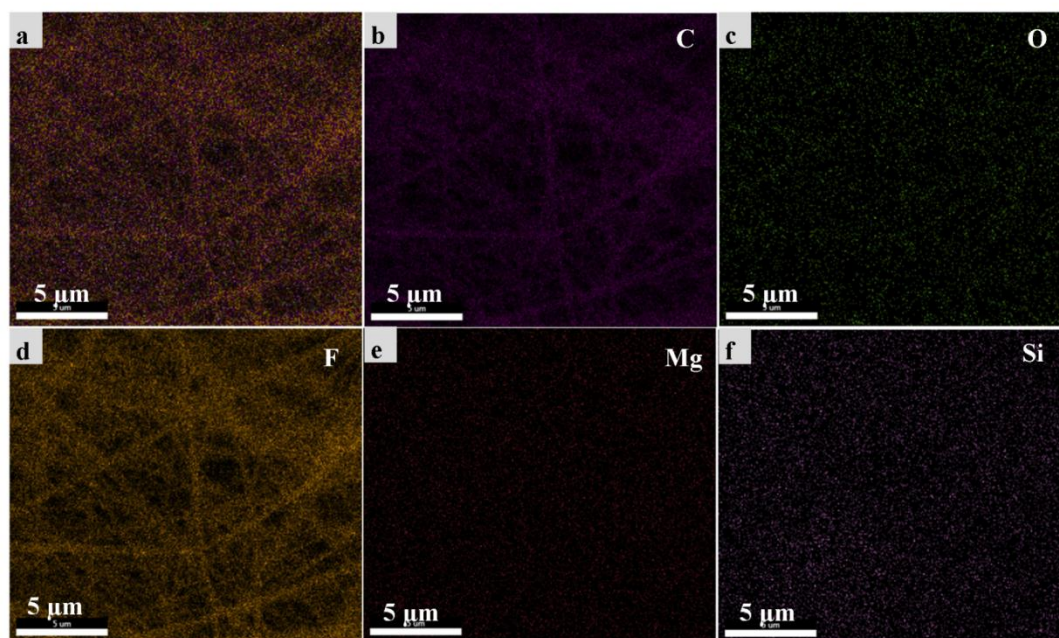


Fig.6.7 EDS elemental mapping of TGP-0.10 nanofabrics: (a) overlay distributions of elements, (b) distribution of carbon, (c) distribution of oxygen, (d) distribution of fluorine, (e) distribution of magnesium, and (f) distribution of silicon.

The electrostatic stretching effect induced during electrospinning ensures the alignment and embedding of the fillers within the PVDF matrix. Additionally, improving the interfaces of FGNS with the PVDF matrix facilitates the chemical interaction between them. This is further corroborated by the EDS elemental mapping of TGP-0.10 based nanofabrics that display improved dispersion of fillers without any possible aggregation in the PVDF matrix (Fig.6.7).

### 6.1.2.2 XRD results

Fig.6.8 represents the XRD patterns of E-PVDF and TGP-based composite nanofabrics. E-PVDF displays the diffraction peak at  $2\theta = 18.4^\circ$  and  $20.4^\circ$ , which correspond to the (020) and (110/200) crystal planes of  $\alpha$ - and  $\beta$ -phases of PVDF, respectively [Chi et al. 2019]. With the introduction of FGNS in TGP nanofabrics, the intensity of  $\alpha$  peak weakens while the  $\beta$  peak intensifies. Notably, the characteristic  $\alpha$  peak diminishes while  $\beta$  peak shifts to  $2\theta = 20.6^\circ$  for TGP-0.10 based nanofabrics, thereby indicating the probable interactions between the fillers and PVDF matrix.

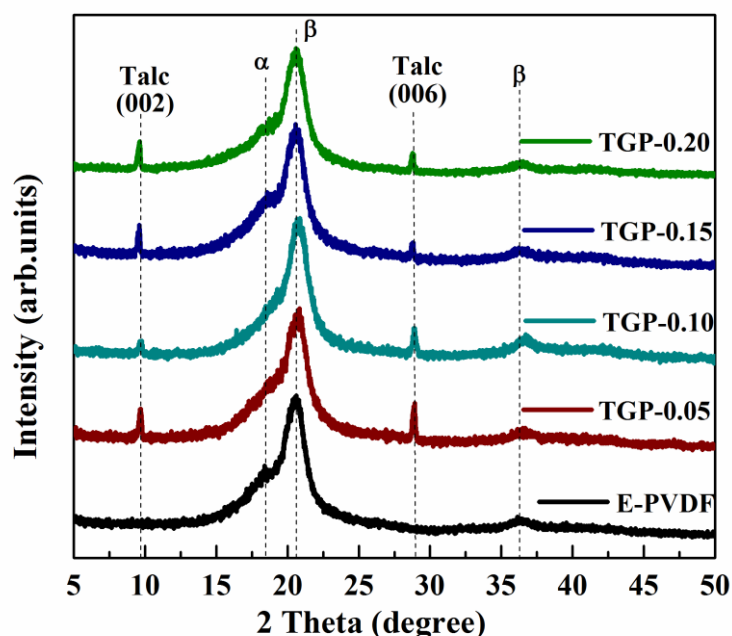


Fig.6.8 XRD patterns of E-PVDF and TGP-based nanofabrics.

Additionally, the diffraction peaks at  $2\theta = 9.4^\circ$  and  $28.6^\circ$  displayed by the TGP nanofabrics correspond to the crystal planes (002) and (006) of talc nanosheets (ICDD-013-0558), thus confirming their presence in the former. XRD results imply the domination of the  $\beta$ -phase with the strong reflection peak at  $2\theta = 20.6^\circ$  and a weak peak at  $2\theta = 36.3^\circ$  for TGP-0.10 based nanofabrics compared to E-PVDF [Cai et al. 2017]. Thus the addition of FGNS facilitates the transformation of  $\alpha$ - to  $\beta$ -phase of PVDF in the TGP-based nanofabrics.

### 6.1.2.3 FTIR results

The enhancement of  $\beta$ -phase crystallization in the TGP nanofabrics is further confirmed via FTIR analysis. Evident from Fig.6.9a, E-PVDF and TGP nanofabrics display absorption bands characteristic of the  $\alpha$ -phase ( $763$  and  $975\text{ cm}^{-1}$ ) and the  $\beta$ -phase ( $840$ ,  $1071$ ,  $1275$ , and  $1401\text{ cm}^{-1}$ ) of PVDF [Mandal and Nandi 2013; Shetty et al. 2020]. The tiny peak at  $1234\text{ cm}^{-1}$  corresponds to the  $\gamma$ -phase; however, other exclusive bands ( $776$ ,  $812$ , and  $833\text{ cm}^{-1}$ ) characteristics of  $\gamma$ -phase are not evident in the present study [Gregorio 2006]. Moreover, the presence of a prominent band at  $1275\text{ cm}^{-1}$  that is characteristic of the  $\beta$ -phase exhibited by TGP nanofabrics substantiates the crystallization of the  $\beta$ -phase in the PVDF matrix.

The calculated  $F(\beta)$  values for E-PVDF and TGP nanofabrics are shown in Table 6.1. TGP nanofabrics demonstrated improved  $F(\beta)$  values compared to E-PVDF, with TGP-0.10 reaching a maximum of 90.2 %. Thus the enhancement of  $F(\beta)$  values displayed by TGP nanofabrics implies the facilitation of  $\beta$ -phase by the induced FGNS in the talc/PVDF matrix. This enhancement of  $\beta$ -phase in the TGP based nanofabrics can be ascribed to the strong interactions between the functional groups ( $-\text{OH}$ ,  $-\text{C}=\text{O}$ ,  $-\text{COOH}$ ) on the graphene sheets/talc nanosheets and  $-\text{CF}_2$  groups of PVDF. The vibrational bands at  $875$  and  $1173\text{ cm}^{-1}$  associated with the CC asymmetric stretching and  $\text{CF}_2$  symmetric stretching modes of E-PVDF shifted to  $877\text{-}879\text{ cm}^{-1}$  and  $1177\text{-}1179\text{ cm}^{-1}$ , respectively in the vibrational spectra of TGP-based nanofabrics (Fig.6.9b and c) [Ulaganathan and Rajendran 2010; Sharma et al. 2015]. Due to the higher electronegativity of fluorine as against carbon and hydrogen atoms of PVDF, the shifting of vibrational bands as mentioned earlier corroborates the strong interaction between the FGNS and PVDF chains; this interaction facilitates the

transformation of trans-gauche-trans-gauche (TGTG) conformation of the  $\alpha$ -phase to the all-trans conformation (TTTT), characteristic of the  $\beta$ -phase.

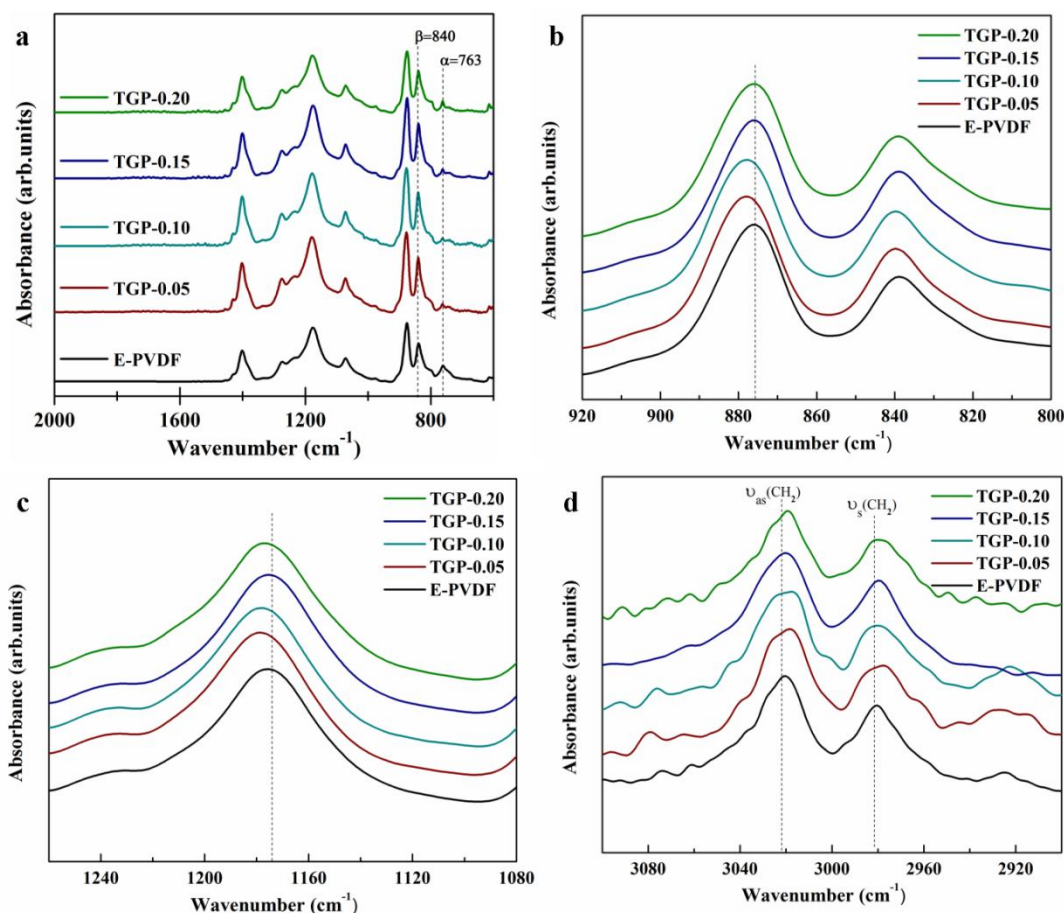


Fig.6.9 FTIR spectra of E-PVDF and TGP-based nanofabrics in the wavenumber range of a) 2000-650  $\text{cm}^{-1}$ , b) 920-800  $\text{cm}^{-1}$ , c) 1250-1080  $\text{cm}^{-1}$ , and d) 3100-2900  $\text{cm}^{-1}$ .

Further, the FTIR bands in the region of 3100-2900  $\text{cm}^{-1}$  (Fig.6.9d) were probed to ascertain the interfacial interactions between the FGNS and PVDF matrix. The  $-\text{CH}_2$  stretching vibration bands [asymmetric ( $\nu_{\text{as}}$ ) and symmetric ( $\nu_{\text{s}}$ )] of TGP-based fabrics shifted to lower wavenumbers when compared with that of the E-PVDF, affirming the interfacial interactions between the filler and the polymer matrix. The shifting of the bands mentioned above could be ascribed to the damping of the stretching vibrations of  $-\text{CH}_2$  dipoles, and accordingly the damping coefficient ( $r_{\text{dc}}$ ) is calculated using equation (6.1) [Abdalla et al. 2016].



$$r_{dc} = 4\pi c \sqrt{(\vartheta_{PVDF}^2 - \vartheta_{TGP}^2)} \quad (6.1)$$

Where  $c$  is the velocity of light,  $\vartheta_{PVDF}$  is the wavenumber of E-PVDF with damping-free stretching vibrations of  $-\text{CH}_2$  dipoles, and  $\vartheta_{TGP}$  is the wavenumber of TGP-based nanofabrics exhibiting damped stretching vibrations of  $-\text{CH}_2$  dipoles. The damping coefficient ( $r_{dc}$ ) increases and attains the maximum value for TGP-0.10 nanofabrics and decreases thereafter (Fig I.6, Appendix). This is ascribed to the attainment of percolation threshold loading of FGNS at the loading of 0.10 wt% in the PVDF matrix. The increased damping coefficient ( $r_{dc}$ ) displayed by TGP-0.10 nanofabrics indicates good interfacial interaction, which promotes the electroactive  $\beta$ -phase of PVDF. The probable mechanism of interaction between the hybrid fillers (talc nanosheets and FGNS) and the PVDF matrix is represented in Fig.6.10.

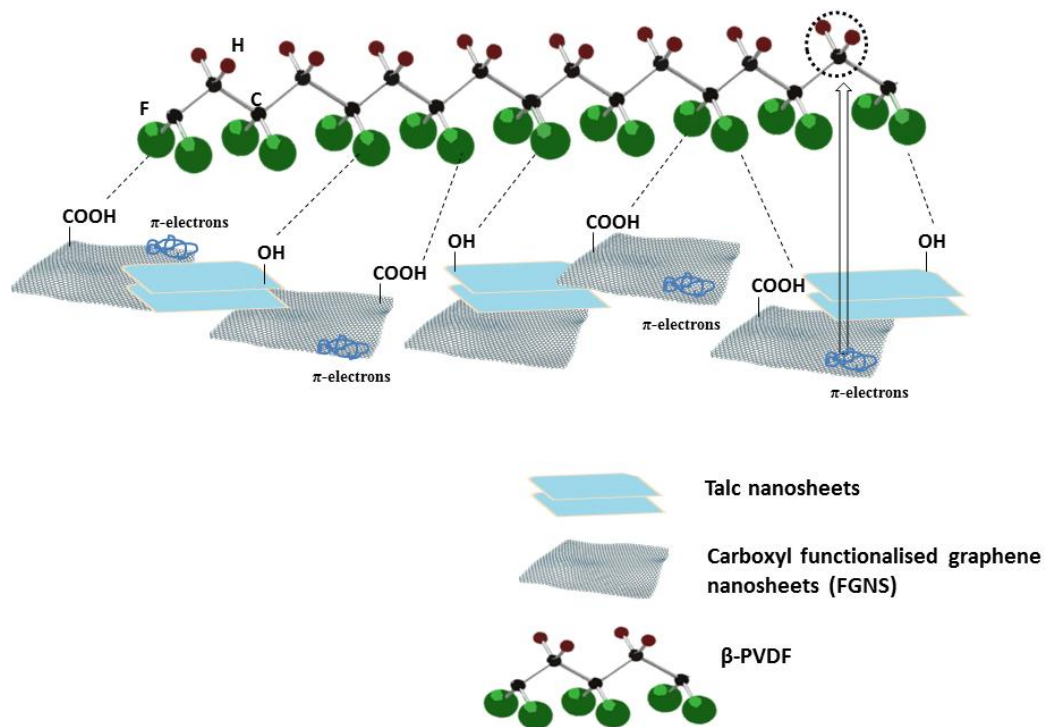


Fig.6.10 Schematic illustration of plausible interactions between hybrid fillers and PVDF.

### 6.1.2.4 DSC results

Fig.6.11a and b shows the DSC curves during the cooling and heating cycles for E-PVDF and TGP-based nanofabrics with their corresponding melting temperatures ( $T_m$ ), crystallization temperature ( $T_c$ ), and degree of crystallinity ( $X_c$ ) as listed in Table 6.1. Evidently, for TGP-based nanofabrics, the  $T_m$  and  $T_c$  values shifted to a higher temperature than E-PVDF. This can be attributed to the inclusion of well-dispersed filler particles that act as nucleation sites, which promote the crystallization of PVDF. However, the  $X_c$  values of TGP-based nanofabrics decreased as against the E-PVDF. This may be ascribed to a larger number of nuclei growth initiated by the nucleating agents, which continue to grow in the limited space of the nanofiber during electrospinning, subsequently leading to smaller spherulites. Thus, the growth of these nuclei results in more crystal defects that reduce the degree of crystallinity. Furthermore, the length, distribution, and curvature of filler hinder the mobility of PVDF chains, which also affects the  $X_c$  values. A similar trend in the decline of  $X_c$  values for graphene/PVDF-based systems was reported in the literature [Al-Saygh et al. 2017; Ismail et al. 2018].

Since the melting temperature range for the  $\alpha$ - and  $\beta$ -crystallites of PVDF is similar (167-175 °C), the DSC will not be able to distinguish between these two phases [Zhang et al. 2020]. However, DSC can be used to identify  $\gamma$ -phase in the TGP-based nanofabrics, as the melting peak of the same appears in the temperature range of 179-190 °C [Martins et al. 2014; Pickford et al. 2019]. Accordingly, the results of XRD, FTIR, and DSC together suggest the predominance of the  $\beta$ -phase in TGP-based nanofabrics.

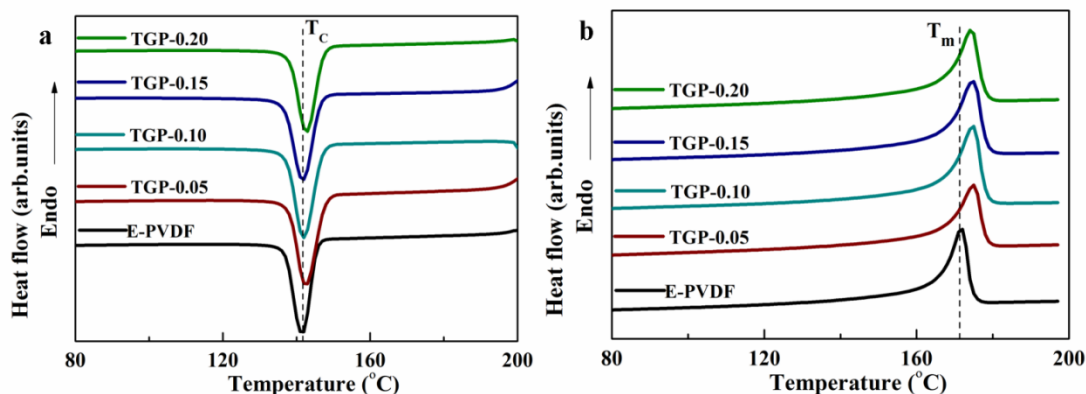


Fig.6.11 DSC traces of E-PVDF and TGP-based fabrics: (a) Cooling cycle; and (b) Heating cycle.

#### 6.1.2.5 Tensile testing results

The characteristic tensile stress-strain behavior of the E-PVDF and TGP-based nanofabrics is shown in the Fig.6.12, with its mechanical properties summarized in Table 6.1. The addition of FGNS in TGP-based nanofabrics enhanced the tensile strength and Young's modulus of the latter. Graphene and its derivatives have been proven to improve the tensile properties of PVDF-based composites as the former offers higher aspect ratio, flexibility and Young's modulus [Chhetri et al. 2016; Islam et al. 2019]. A low loading of 0.10 wt% FGNS in TGP-based nanofabrics resulted in a significant increment in tensile strength ( $17.03 \pm 2.58$  MPa) and Young's modulus ( $53.41 \pm 1.12$  MPa) while the strain at break was reduced, compared to E-PVDF. Moreover, the FGNS loading beyond 0.10 wt% in TGP-based nanofabrics displayed no significant enhancement in the mechanical properties. This is attributable to the possible restacking of graphene flakes due to van der Waals forces that promote the piling of graphene flakes at higher loading; and this subsequently impairs the mechanical properties the composite [Zhao et al. 2010]. The enhancement of mechanical properties demonstrated by the TGP-based nanofabrics is ascribed to the following: first, the good dispersion of nanofillers (talc nanosheets and FGNS) in the PVDF matrix improves the filler-polymer interfacial contact. Second, the effective interaction between the  $-CF_2$  groups of PVDF and hydroxyl groups of nanofillers via hydrogen bonding facilitates the stress transfer from the polymer matrix to the nanofillers. And third, the high aspect ratio offered by nanofillers restricts the movement of PVDF chains. Overall, the inclusion of FGNS in TGP-based nanofabrics increased the mechanical properties due to the compatibility of the former with the PVDF matrix.

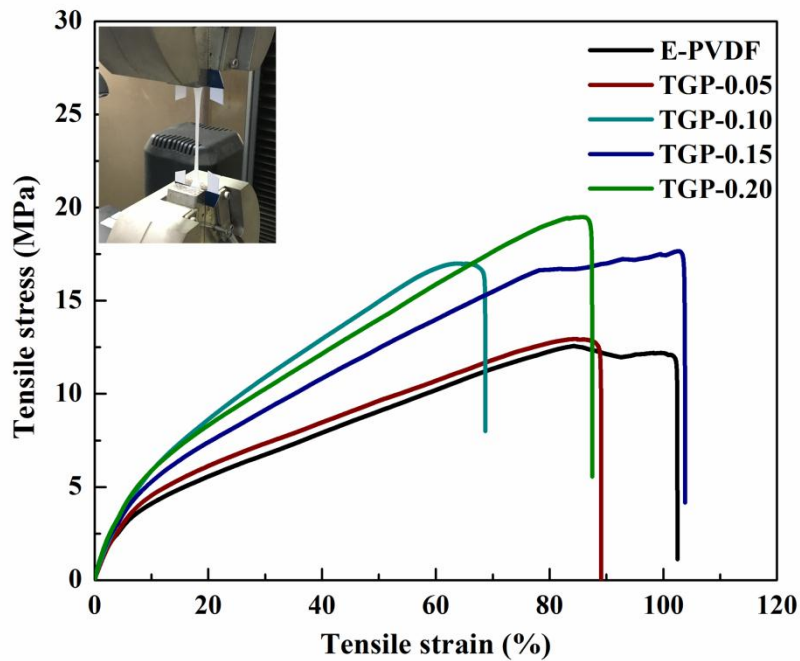


Fig.6.12 Tensile stress-strain plots of E-PVDF and TGP-based nanofabrics.

Table 6.1  $\beta$ -phase fraction, crystallization temperature, melting temperature, degree of crystallinity, tensile strength, and Young's modulus of the E-PVDF and TGP-based nanofabrics.

| Sample          | FTIR<br>% $\beta$ -<br>phase | DSC                          |                              |             | Mechanical property                |                                    |
|-----------------|------------------------------|------------------------------|------------------------------|-------------|------------------------------------|------------------------------------|
|                 |                              | $T_c$ ( $^{\circ}\text{C}$ ) | $T_m$ ( $^{\circ}\text{C}$ ) | $X_c$ (%)   | Tensile<br>strength<br>(MPa)       | Young's<br>modulus<br>(MPa)        |
| E-PVDF          | 61.4                         | 141.5                        | 171.7                        | 55.4        | $12.70 \pm 0.11$                   | $26.69 \pm 0.23$                   |
| TGP-0.05        | 87.7                         | 142.6                        | 174.8                        | 48.4        | $13.70 \pm 0.55$                   | $32.61 \pm 0.74$                   |
| <b>TGP-0.10</b> | <b>90.2</b>                  | <b>141.9</b>                 | <b>174.7</b>                 | <b>38.2</b> | <b><math>17.03 \pm 2.58</math></b> | <b><math>53.41 \pm 1.12</math></b> |
| TGP-0.15        | 82.6                         | 141.7                        | 174.8                        | 51.0        | $17.49 \pm 0.55$                   | $33.52 \pm 2.21$                   |
| TGP-0.20        | 76.9                         | 142.6                        | 174.3                        | 42.8        | $19.43 \pm 1.22$                   | $42.43 \pm 0.44$                   |

### 6.1.2.6 Piezoelectric measurements

The flexoelectric effect is the induction of electrical polarization due to strain gradient evident in dielectric materials. Further, this effect is more significant at the nanoscale

and has been demonstrated to enhance the piezoelectric response of the nanogenerator [Han et al. 2016]. Thus, the flexoelectric effect possibly contributes to the piezoelectric performance of the TGP-based nanogenerator. The nanogenerators based on the E-PVDF and TGP nanofabrics were imparted with compression force using a pneumatic actuator (operating pressure 0.4 MPa) setup (Fig.2.3) and their corresponding piezoelectric responses are shown in Fig.13a. TGP based nanofabrics demonstrated a significant enhancement in the piezoelectric potential when compared to virgin PVDF nanofabrics, with TGP-0.10 reaching a maximum open-circuit voltage of 12.9 V. In contrast, E-PVDF displayed the open-circuit voltage of 2.0 V. The piezoelectric performance of the nanogenerator is enhanced with an increase in FGNS loading up to 0.10 wt% beyond which the piezoelectric output voltage decreased. The declined piezoelectric performance of the TGP nanofabrics at higher FGNS loading may be attributed to the filler aggregation leading to leakage of charges through the conducting FGNS networks in the PVDF matrix.

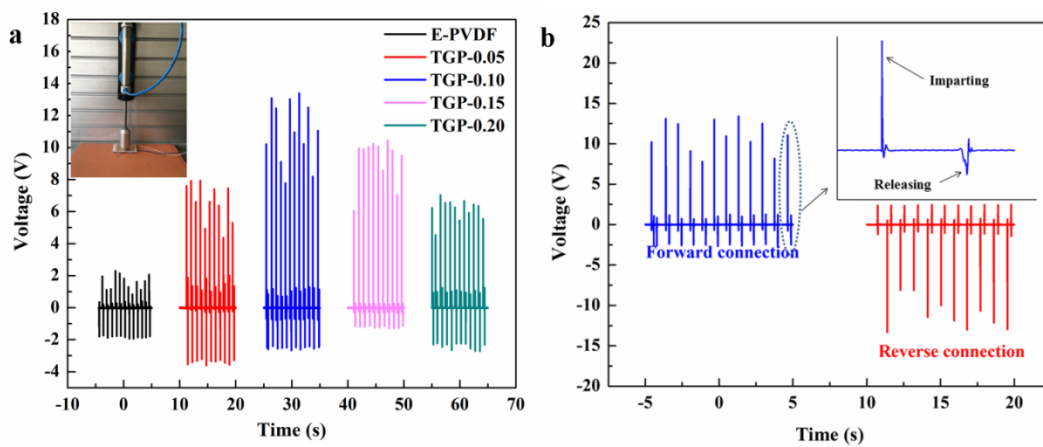


Fig.6.13 a) The output voltage generated from E-PVDF and TGP-based nanofabrics under impact by pneumatic actuator mode, b) switching polarity sequence test of TGP-0.10 nanofabrics with inset displaying magnified impacting and releasing responses.

Fig.6.13b shows the switching polarity sequence with voltage amplitudes implying the mechanical imparting and releasing modes on the nanogenerator comprised of TGP-0.10 nanofabrics. Evidently, the imparting mode voltage amplitude is greater compared to release amplitude, as the former is proportional to the impact

force while the latter is dependent on the elasticity of the material. The switching polarity sequence demonstrated by the TGP based nanogenerator confirms that the output signals stemmed solely from the piezoelectric response of TGP nanofabrics. When the nanogenerator composed of electrospun nanofabrics is excited via a compressive strain in vertical direction, positive and negative piezoelectric potentials are produced on the top and bottom electrodes of the nanogenerator, respectively. The potential difference between the nanogenerator electrodes causes the charges to flow between the electrodes through an external circuit resulting in an electrical signal. The moment the compressive strain is released the piezoelectric potential difference between the electrodes vanishes and the accumulated charges flow in opposite direction resulting in a reverse electrical signal. Fig.6.14a displays the working mechanism of the nanogenerator under the mechanical impact and releasing modes.

Further the power density of the TGP-0.10 based nanogenerator was measured by connecting the nanogenerator across different load resistances (0.1-5 M $\Omega$ ) and noticing the voltage drop across the same as illustrated in Fig.6.14b. Under the mechanical imparting mode, TGP-0.10 based nanogenerator produced a maximum voltage of 8.8 V across a load resistance of 3 M $\Omega$ . Accordingly, the instantaneous power density (P) was measured to be 1.72  $\mu\text{W}/\text{cm}^2$ . Fig.6.14b shows the output voltage and power density generated from TGP-0.10 based nanogenerator across varying load resistance. This increment in the open-circuit voltage and power density displayed by TGP-0.10 nanofabrics can be ascribed to the higher  $\beta$ -phase fraction and easier alignment of the  $-\text{CH}_2/-\text{CF}_2$  dipoles due to the uniformly dispersed networks of talc nanosheets and FGNS in the PVDF matrix. Further, the electrical conductivity of the E-PVDF and TGP-based nanofabrics was measured (Section I.7, Appendix). The electrical conductivity of the TGP nanofabrics reached a maximum value at FGNS loading of 0.10 wt %, beyond which there was a marginal decrease in it (Fig I.7, Appendix). The inherent electrical conductivity of FGNS led to the higher conductivity at a lower percolation threshold that boosted the piezoelectric performance of TGP-0.10 based nanofabrics. Further, the rough and porous surface morphology of TGP-0.10 based nanofibers possibly contributes to its improved piezoelectric response (Section I.8, Appendix).

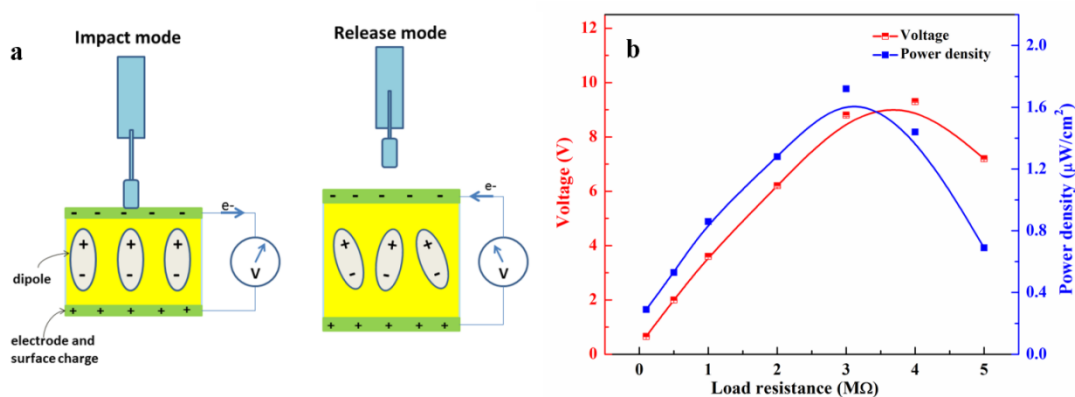


Fig.6.14 a) working mechanism of the nanogenerator under impact and release mode; b) generated output voltage and power density as a function of varying load resistance from a TGP-0.10 based nanogenerator.

#### 6.1.2.7 PFM results

PFM was used to probe the local piezoelectric response of the TGP-based nanofabrics at the nanoscale. In PFM, a single nanofiber was subjected to a bias voltage, and its corresponding electromechanical response was recorded in terms of PFM amplitude and phase data. The PFM amplitude and phase data yield the material's local strain and polarization responses, respectively. PFM evaluated the nanoscale electromechanical behavior of the TGP-0.10 based single nanofiber with topography, amplitude, and phase responses as a function of bias voltage -30 V to +30 V, as represented in the Fig.6.15a-c. The phase image (Fig.6.15c) displays regions of different contrast (bright and dark) indicating the polarization directions; the corresponding phase hysteresis loop (Fig.6.15d) represents 180° domain switching behavior, indicating the ferroelectric response of TGP nanofiber. The phase switches by 180° at the coercive voltage (~ 0.9 V), beyond which the phase loop saturates. Furthermore, the amplitude signal (Fig.6.15e) from TGP nanofiber depicts the butterfly-shaped characteristics loop resembling its piezoelectric property. The variation of amplitude response equals the strain changes ( $S$ ) under the external electrical field ( $E$ ); thus, the piezoelectric coefficient ( $d_{33}$ ) of the TGP nanofiber can be calculated using the formula of  $S = d_{33}E$  [Gebrekrestos et al. 2018]. From Fig.6.15e the maximum amplitude for TGP-0.10 nanofiber is 1.83 nm at 30 V, and

accordingly, the calculated  $d_{33}$  is 61 pm/V, which is much higher than that of E-PVDF (10 pm/V). Similarly, the piezoelectric coefficient values for TGP-0.05, TGP-0.15, and TGP-0.20 based nanofibers were measured to be 45 pm/V, 38 pm/V, and 36 pm/V, respectively (Fig.6.16).

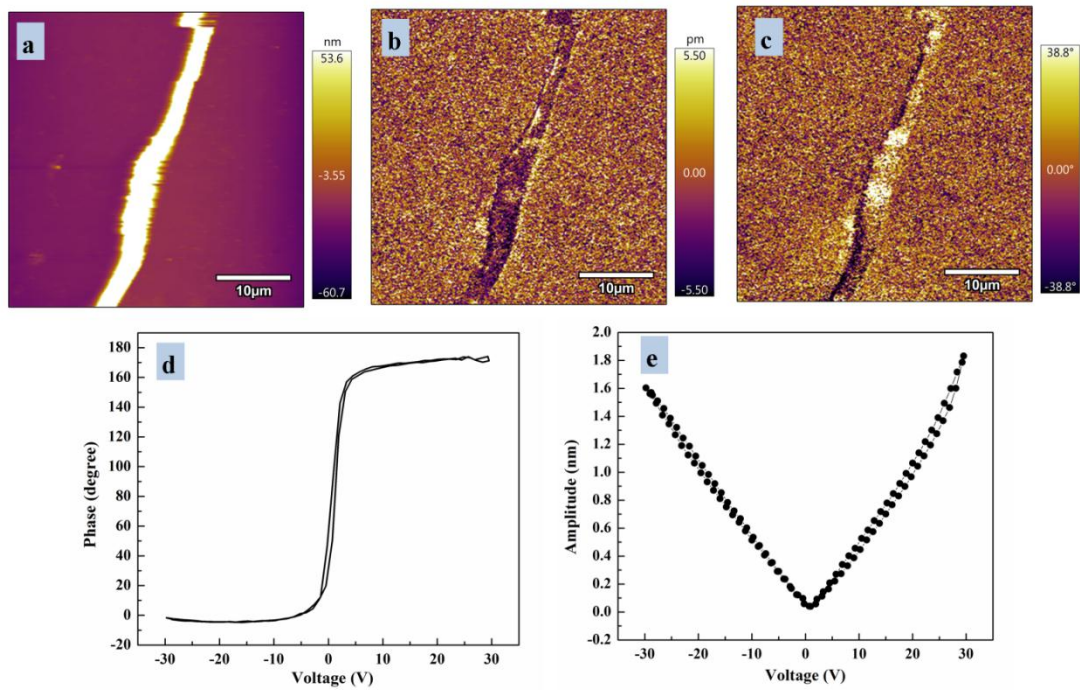


Fig.6.15 PFM analysis of TGP-0.10 : (a) topography image, (b) amplitude image, (c) phase image, (d) amplitude loop, and (e) phase loop.



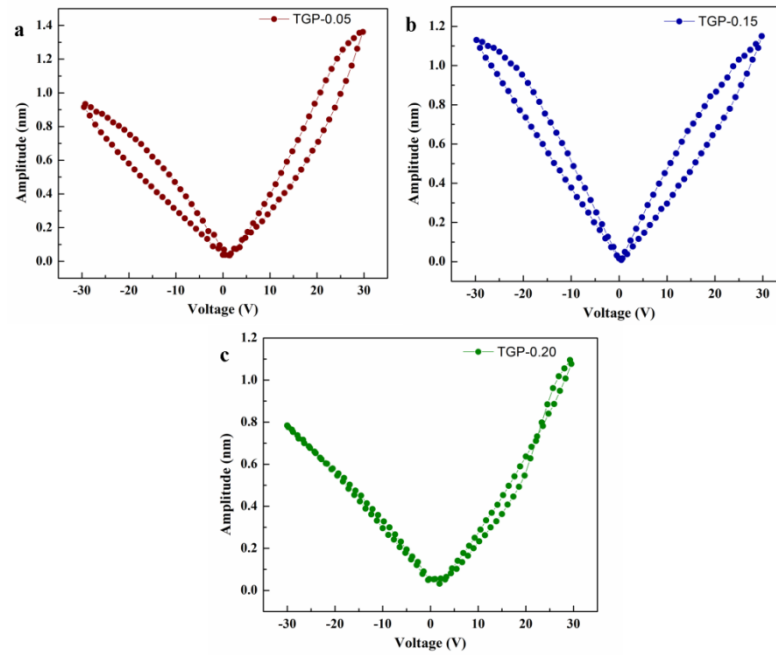


Fig.6.16 PFM amplitude loops of a) TGP-0.05, b) TGP-0.15, and c) TGP-0.20 based nanofibers.

According to equation (6.2), the output voltage (V) is dependent on the material's piezoelectric coefficient, Young's modulus (E), applied strain ( $\epsilon$ ), and charge separation distance/nanofiber diameter (d) [Ico et al. 2016]. Thus, the significant output voltage exhibited by TGP-based nanofabrics can be accounted to its reduced fiber diameter and higher Young's modulus when compared against E-PVDF nanofabrics.

$$V = \frac{d_{33}E_{33}\epsilon_3d}{k} \quad (6.2)$$

Further, the interactions between the oxygen containing functional groups ( $-\text{OH}$ ,  $-\text{COOH}$ ) of the hybrid fillers (talc nanosheets and FGNS) and  $-\text{CF}_2/-\text{CH}_2$  groups of PVDF matrix enable the orientation of the all-trans  $\beta$ -phase. Also, the conducting path provided by FGNS in the host matrix would reduce the internal resistance of the nanogenerator and thereby facilitate the movement of induced charges generated by the PVDF. Herein talc nanosheets facilitated the  $\beta$ -phase conformation and aided the dispersion of FGNS in the PVDF matrix. In contrast, the FGNS provided conducting network for easy movement of induced charges in the polymer matrix and partly contributing to the  $\beta$ -phase fraction enhancement via interaction with PVDF. Thus

hybrid fillers synergistically improved the performance of PVDF-based composite nanofabrics.

## 6.2 SUMMARY AND CONCLUSIONS

In summary, a flexible hybrid filler/PVDF based composite nanofabric was successfully fabricated by electrospinning. Synergistic effects of talc nanosheets and carboxyl functionalized graphene nanosheets contributed to the enhanced piezoelectric response of the PVDF-based composite nanofabrics. A low loading of 0.10 wt% of FGNS in TGP-based nanofabrics led to a significant improvement in the  $\beta$ -phase fraction, mechanical property, and piezoelectric performance when compared against E-PVDF. Further, the nanogenerator based on 0.5 wt% of talc nanosheets and 0.10 wt% of FGNS nanofabrics demonstrated a peak output voltage of 12.9 V and a maximum power density of  $1.72 \mu\text{W}/\text{cm}^2$  under the mechanical impacted conditions. TGP-0.10 based nanofibers exhibited the piezoelectric coefficient ( $d_{33}$ ) value of 61 pm/V, that being 6 times higher than the E-PVDF nanofibers (10 pm/V). The uniform distribution and effective interactions of hybrid fillers (talc nanosheets and FGNS) with the PVDF matrix led to the promotion of all-trans conformation of  $\beta$ -phase. The developed hybrid composite nanofabrics could be a promising material in designing portable and flexible electronic devices.

# **CHAPTER 7**



## CHAPTER 7

### SUMMARY AND CONCLUSIONS

---

Functional nanofabrics of 2-D nanosheets/PVDF composites were successfully prepared by electrospinning. The inclusion of these nanofillers (organically modified Ni-Co layered double hydroxide (OLDH), talc nanosheets, and carboxyl functionalized graphene nanosheets (FGNS)) in the PVDF matrix improved the physical and piezoelectric properties of the resultant composite nanofabrics. It was observed that the mean fiber diameter of PVDF composite nanofibers decreased compared to pristine PVDF nanofibers that were ascribed to the enhanced charge density of the electrospinning solution. Further, the composite nanofabrics displayed a higher  $\beta$ -phase fraction with a subsequent reduction in crystallinity as against PVDF nanofabrics.

In the case of OLDH/PVDF composite nanofabrics, the specific interaction between the hydroxyl groups of OLDH and  $-\text{CF}_2$  groups of PVDF through hydrogen bonding facilitated the promotion of electroactive  $\beta$ -phase in the resultant composites. The dielectric and piezoelectric responses of the composite nanofabrics were significantly improved compared to the pristine PVDF nanofabrics. For talc nanosheets/PVDF composite nanofabrics, talc was embedded in the PVDF matrix without any surface modification. This was possible due to its nano dimension and high aspect ratio. Synergistic interaction between the nanofiller and electrospinning led to the improved electroactive  $\beta$ -phase and thereby the piezoelectric response of the talc/PVDF composite nanofabrics. The tortuous path imposed by the talc nanosheets in the PVDF matrix led to the improved thermal stability of the composite nanofabrics. Piezoelectric nanogenerator based on the composite nanofabric with a talc loading of 0.50 wt% generated an output voltage of 9.1 V and a power density of  $1.12 \mu\text{W}/\text{cm}^2$ . Furthermore, the composite nanofibers displayed well-defined ferroelectric characteristics with an enhanced  $d_{33}$  value of 43.3 pm/V. Reduction of nanofiber diameters and improved  $\beta$ -phase fraction of the electrospun PVDF/talc nanosheet composites accounted for their augmented piezoelectric response. Finally, talc nanosheets/FGNS/PVDF (TGP) based hybrid composite nanofabrics displayed a

maximum  $\beta$ -phase fraction of 90.2% with enhanced mechanical and piezoelectric properties. Functionalization of graphene nanosheets improved the compatibility with the polymer matrix, and the carboxyl groups of FGNS promoted the  $\beta$ -phase of PVDF via interfacial interactions. Further, FGNS led to forming an electrically conductive network in the polymer matrix aided by talc nanosheets and electrospinning. The talc nanosheets and FGNS synergistically improved the  $\beta$ -phase fraction, mechanical property (tensile strength ( $17.03 \pm 2.58$  MPa) and Young's modulus ( $53.41 \pm 1.12$  MPa)), and piezoelectric response (12.9 V and  $\sim 61$  pm/V) of the TGP nanofabrics.

Conclusively, role of nanofillers, particularly that of nucleating agents, as conducting pathways and as facilitators for dipole alignment, has significantly contributed to the promotion of electroactive  $\beta$ -phase in the PVDF composite nanofabrics. Herein, the incorporated nanofillers, coupled with the electrospinning, have enhanced the mechanical, dielectric, and piezoelectric properties of the PVDF-based composite nanofabrics. Thus the developed composite nanofabrics here could be used to fabricate viable and cost-effective nano-energy harvesting devices.

## SCOPE FOR FURTHER STUDY

---

- Modeling these developed PVDF-based composite nanofabrics using adequate software (Molecular dynamics and Finite element method (FEM)) could be used to study the structure-property relationships at the nanoscale.
- Core-shell nanofibers of these PVDF-based composites could be fabricated by coaxial electrospinning and subsequently explored for energy-harvesting applications.
- Could explore the good piezoelectric and biocompatibility of these PVDF-based composite nanofabrics in biomedical applications (possibly serve as scaffolds for tissue engineering).
- The triboelectric and pyroelectric effects of these PVDF-based composite nanofabrics could be studied and possibly combine these effects in developing a Hybrid energy harvesting system.
- PVDF-based composite nanofabrics could be explored in supercapacitors, filtration membranes, battery separators (lithium-ion), and fuel cells.





## APPENDIX-I

### I.1 Output current values produced from OLDH/PVDF nanofabrics based nanogenerator under tapping mode.

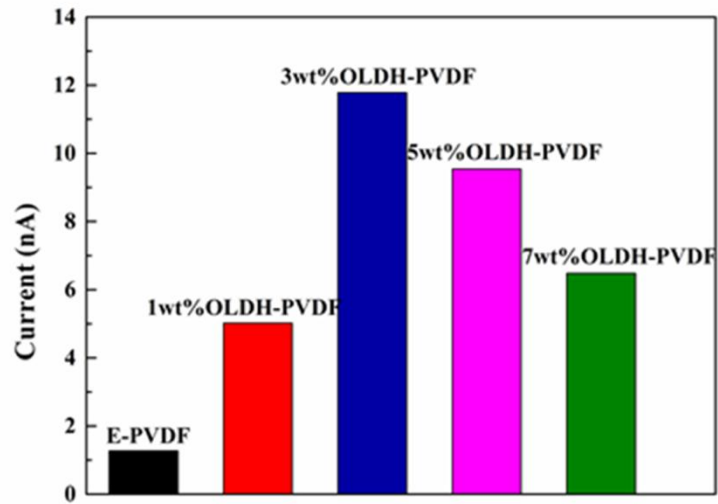


Fig. I.1 The variation of the output current of E-PVDF and OLDH/PVDF nanofabrics based nanogenerator under human finger tapping mode.

### I.2 Output voltage produced from reference nanogenerator under tapping mode.

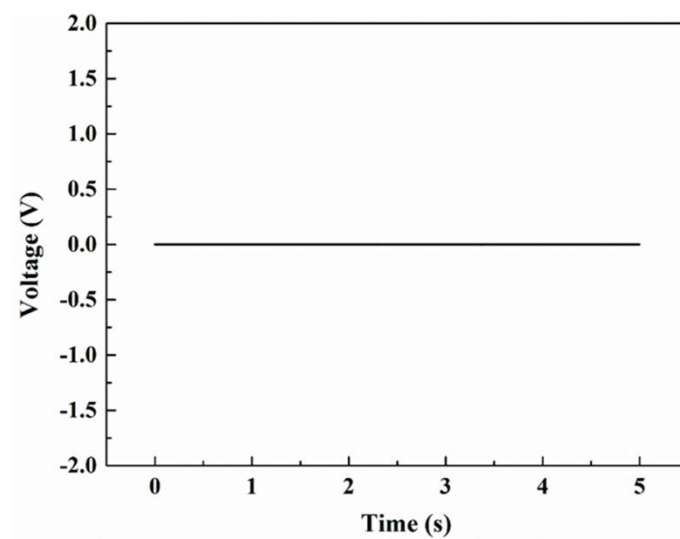


Fig. I.2 The generated output voltage for reference nanogenerator under human finger tapping mode.

**I.3 Output current values produced from talc nanosheets/PVDF nanofabrics based nanogenerator under tapping mode.**

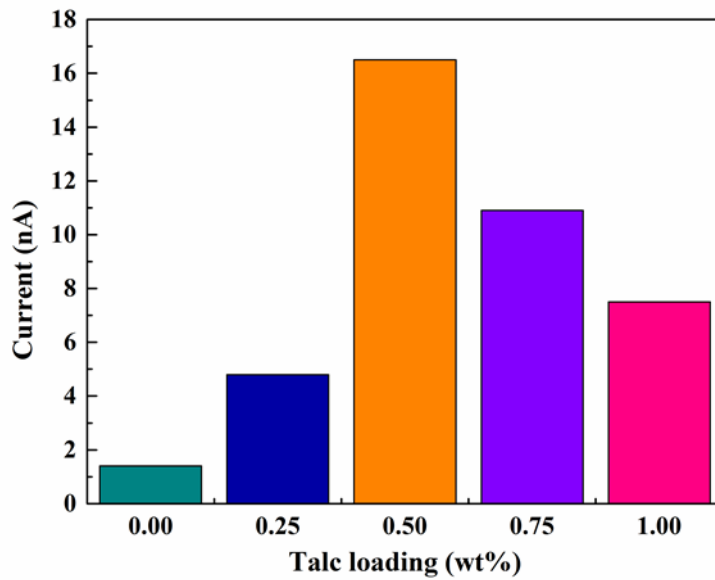


Fig. I.3 The output current response of talc/PVDF nanofabrics based nanogenerator under repetitive tapping mode.

**I.4 TEM and SAED image of talc nanosheets.**

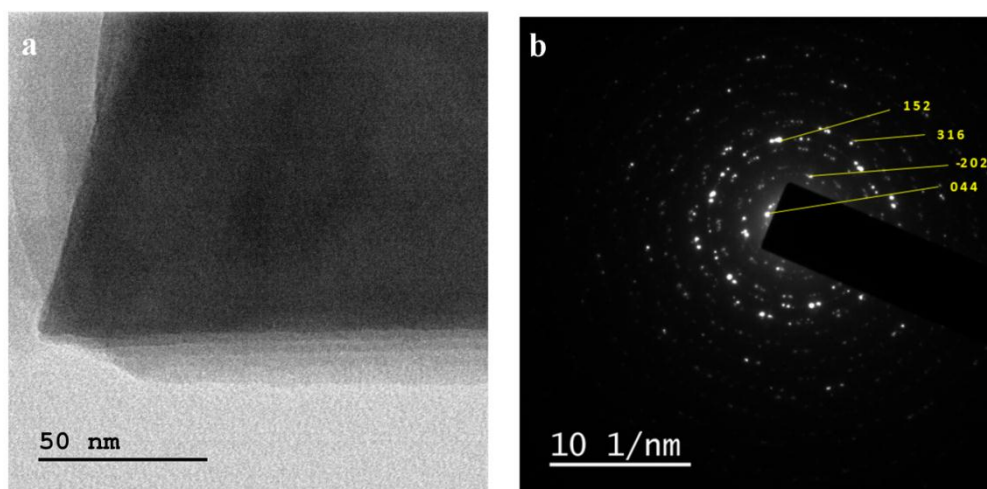


Fig. I.4 a) TEM image; and b) SAED pattern of talc nanosheets.

### I.5 Tensile testing of talc nanosheets/PVDF composite nanofabrics.



Fig. I.5 Tensile test specimen and testing stages of the talc nanosheets/PVDF nanofabrics.

Table I.1 Piezoelectric performance comparison between the fabricated nanogenerator and those of PVDF based nanogenerator reported in the literature.

| Type of materials  | Output Voltage | Output Current | Power Density | Reference |
|--|----------------|----------------|---------------|-----------|
| (0.50 wt%) Carbon nanofiber/PVDF nanofibers                      | 5.8 V          | 1.2 $\mu$ A    | -             | 1         |
| (5 wt%) Potassium sodium niobate/PVDF nanofibers                 | 1.9 V          | -              | -             | 2         |
| (0.1 wt%) Graphene/PVDF nanofibers                               | 7.9 V          | 4.5 $\mu$ A    | -             | 3         |
| Zinc oxide nanorods*/PVDF nanofibers                             | 356 mV         | 456 nA         | -             | 4         |
| (10 wt%) Potassium sodium niobate/PVDF nanocomposite films       | 3.4 V          | 0.1 $\mu$ A    | -             | 5         |
| (20 vol%) Barium titanate/PVDF nanocomposite films               | 6.7 V          | 2.4 $\mu$ A    | -             | 6         |
| (2 wt%) Fe-doped reduced graphene oxide/PVDF nanocomposite films | 5.1 V          | 0.254 $\mu$ A  | -             | 7         |

|   |              |                    |  |                  |
|---|--------------|--------------------|--|------------------|
| (16 wt%) Bismuth oxide/PVDF nanocomposite films                     | 3.6 V        | 2.4 $\mu\text{A}$  | 1 $\mu\text{W}^{**}$                             | <sup>8</sup>     |
| (17.5 wt%) Polyaniline/(10 wt%) halloysite nanotube/PVDF nanofibers | 7.2 V        | 0.75 $\mu\text{A}$ | 0.25 $\mu\text{W}/\text{cm}^2$                   | <sup>9</sup>     |
| Zinc oxide*/PVDF composite fiber membrane                           | 1.12 V       | 1.6 $\mu\text{A}$  | 0.2 $\mu\text{W}/\text{cm}^2$                    | <sup>10</sup>    |
| (0.50 wt%) Laponite nanoclay/PVDF nanocomposite films               | 6 V          | 70 nA              | 0.63 $\mu\text{W}/\text{cm}^2$                   | <sup>11</sup>    |
| <b>(0.50 wt%) talc/PVDF electrospun fabrics</b>                     | <b>9.1 V</b> | <b>16.5 nA</b>     | <b>1.12 <math>\mu\text{W}/\text{cm}^2</math></b> | <b>This work</b> |

\*Film; \*\*Power

Table I.2 Comparison of piezoelectric coefficient ( $d_{33}$ ) values obtained from PFM for some electrospun materials in literature.

| <b>Material (nanofiber)</b>               | <b><math>d_{33}</math> (pm/V)</b> | <b>Reference</b> |
|---|-----------------------------------|------------------|
| PVDF/carbon nanotubes (CNT)               | $35 \pm 5$                        | [29]             |
| PVDF/graphene oxide (GO)                  | 40                                | [25]             |
| PVDF/barium titanate ( $\text{BaTiO}_3$ ) | 50                                | [28]             |
| PVDF                                      | $27.4 \pm 1.5$                    | [8]              |
| $\text{BaTiO}_3$                          | 40                                | [30]             |
| <b>PVDF/talc nanosheets</b>               | <b><math>43.3 \pm 2</math></b>    | <b>This work</b> |

## I.6 Damping coefficient for TGP based composite nanofabrics

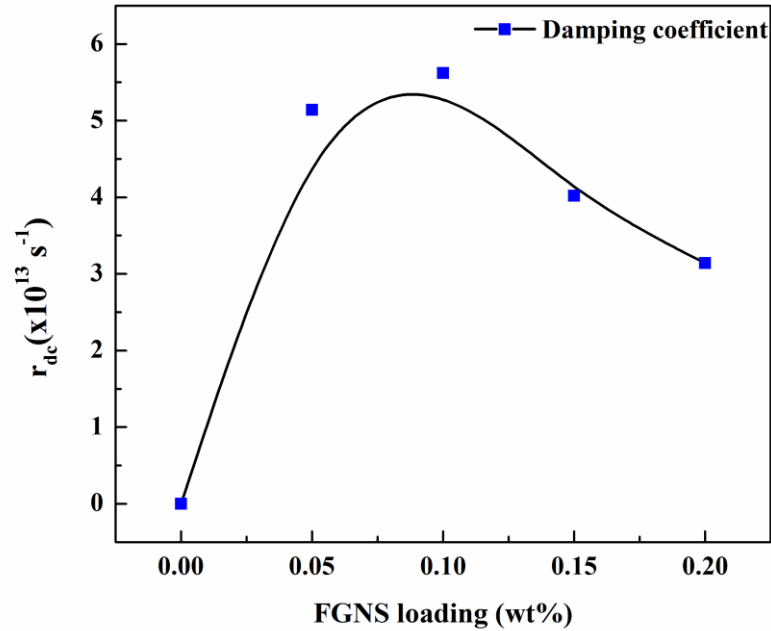


Fig. I.6 Variation of damping coefficient values of TGP nanofabrics as a function of FGNS loading.

## I.7 Electrical conductivity measurements of TGP based composite nanofabrics.

The electrical conductivity of the samples was calculated after obtaining the I-V readings. The electrospun fabrics of E-PVDF and TGP were formed into pellets of 13 mm diameter using 15 Tons Manual Laboratory Press (Table Top) (Kimaya engineers, Thane, India). The formed pellets were subjected to voltage sweep of -5 V to +5 V, and corresponding current variation was recorded via Keithley 2400 source meter. The electrical conductivity ( $\sigma$ ) was calculated using following equation.

$$\sigma = (\rho)^{-1} = \left(\frac{RA}{L}\right)^{-1}$$

Where R is the resistance, A is the electrode area, and L is the pellet thickness.

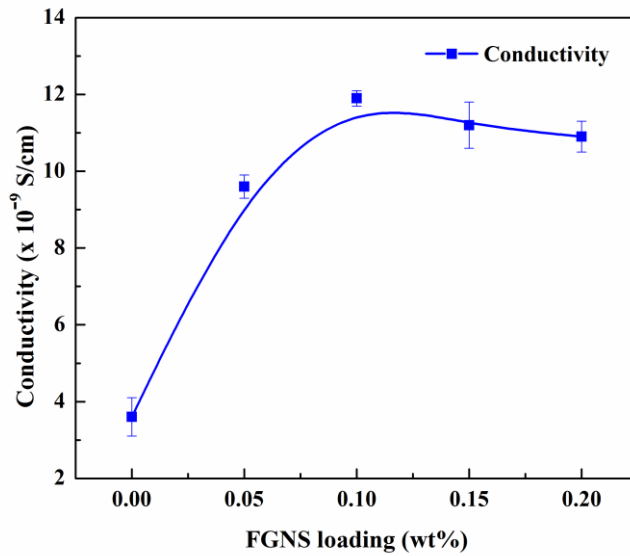


Fig. I.7 Variation of electrical conductivity values of TGP composite nanofabrics as a function of FGNS loading.

### I.8 FESEM images of 0.50 wt% TNS/PVDF, 0.10 wt% FGNS/PVDF, and TGP-0.10 nanofibers.

Fig. I.8a and b show the high magnification FESEM image of 0.50 wt% TNS/PVDF and 0.10 wt%/PVDF nanofibers, respectively. With the introduction of 0.50 wt% TNS and 0.10 wt%/ FGNS in the PVDF matrix, the surface morphology of resultant nanofibers became rough and porous, as evident from the FESEM images (Fig.I.8 (c, d)). The rough surface morphology of nanofibers has been demonstrated to enhance the scavenging energy devices' electrical output due to increased friction areas [Zaarour et al. 2018]. Moreover, porous nanofibers have been shown to improve the voltage response of piezoelectric nanogenerators by efficiently transferring energy from mechanical to electrical domains [Ganeshkumar et al. 2017]. Thus the surface morphology of TGP-0.10 based nanofibers possibly contributes to its improved piezoelectric response.

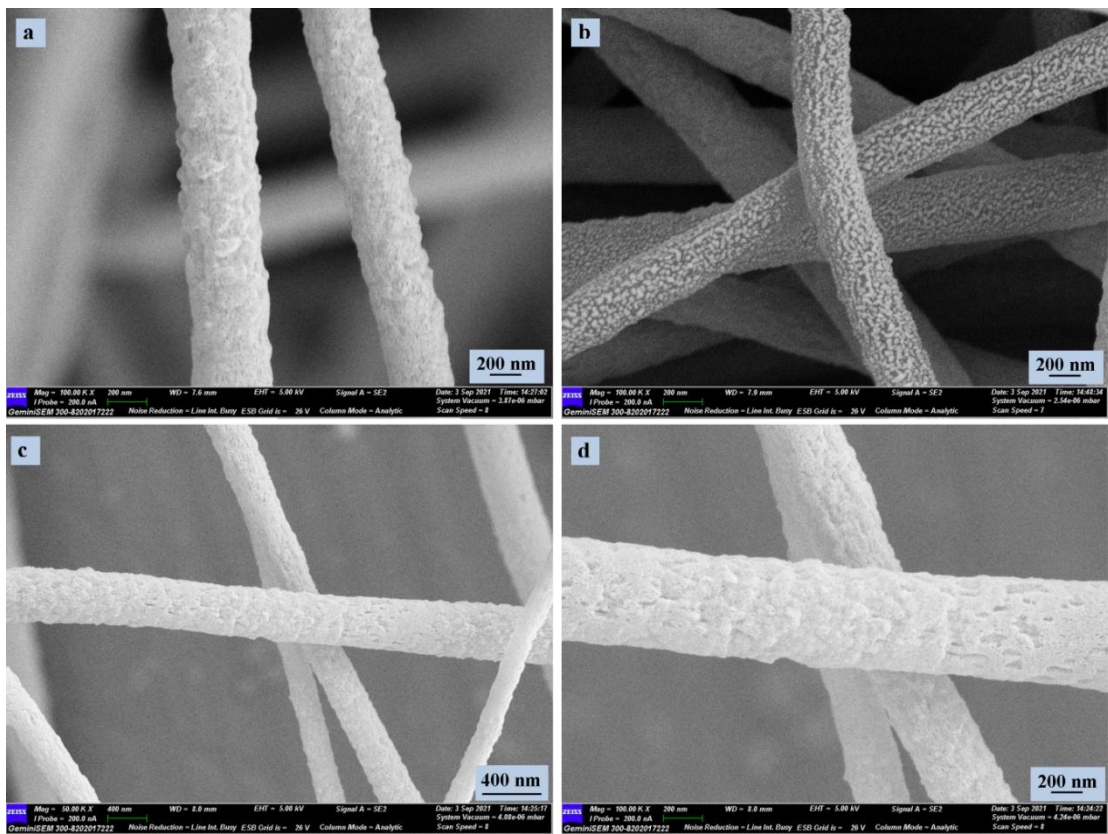


Fig. I.8 FESEM images of: a) 0.50 wt% TNS/PVDF, b) 0.10 wt% FGNS/PVDF, and (c, d) TGP-0.10 nanofibers at 50,000 and 100,000 magnifications, respectively.





## REFERENCES

---

- Abbasipour, M., Khajavi, R., Yousefi, A.A., Yazdanshenas, M.E. and Razaghian, F. (2017). "The piezoelectric response of electrospun PVDF nanofibers with graphene oxide, graphene, and halloysite nanofillers: a comparative study." *J. Mater. Sci. Mater. Electron.*, 28 (21), 15942–15952.
- Abdalla, S., Obaid, A. and Al-Marzouki, F.M. (2016). "Preparation and characterization of poly(vinylidene fluoride): A high dielectric performance nanocomposite for electrical storage." *Results Phys.*, 6, 617–626.
- Abolhasani, M.M., Shirvanimoghaddam, K. and Naebe, M. (2017a). "PVDF/graphene composite nanofibers with enhanced piezoelectric performance for development of robust nanogenerators." *Compos. Sci. Technol.*, 138, 49–56.
- Acosta, M., Novak, N., Rojas, V., Patel, S., Vaish, R., Koruza, J., Rossetti, G.A. and Rödel, J. (2017). "BaTiO<sub>3</sub>-based piezoelectrics: Fundamentals, current status, and perspectives." *Appl. Phys. Rev.*, 4 (4), 041305.
- Adhikary, P. and Mandal, D. (2017). "Enhanced electro-active phase in a luminescent P(VDF-HFP)/Zn<sup>2+</sup> flexible composite film for piezoelectric based energy harvesting applications and self-powered UV light detection." *Phys. Chem. Chem. Phys.*, 19 (27), 17789–17798.
- Al-Saygh, A., Ponnamma, D., AlMaadeed, M.A.A., Poornima Vijayan, P., Karim, A. and Hassan, M.K. (2017). "Flexible pressure sensor based on PVDF nanocomposites containing reduced graphene oxide-titania hybrid nanolayers." *Polymers (Basel)*, 9 (2), 33.
- Alam, M.M., Sultana, A. and Mandal, D. (2018). "Biomechanical and Acoustic Energy Harvesting from TiO<sub>2</sub> Nanoparticle Modulated PVDF Nanofiber Made High Performance Nanogenerator." *ACS Appl. Energy Mater.*, 1 (7), 3103–3112.
- Andrady, A.L. (2009). Introduction. In *Science and Technology of Polymer Nanofibers*, (Hoboken, NJ, USA: John Wiley & Sons, Inc.), 1–26.

Andrew, J.S. and Clarke, D.R. (2008). "Effect of Electrospinning on the Ferroelectric Phase Content of." *Langmuir*, (7), 670–672.

Angamma, C.J. (2011). "A Study of the Effects of Solution and Process Parameters on the Electrospinning Process and Nanofibre Morphology." *Ieee Trans. Ind. Appl.*, 47 (3), 1109–1117.

Anithakumari, P., Mandal, B.P., Abdelhamid, E., Naik, R. and Tyagi, A.K. (2016). "Enhancement of dielectric, ferroelectric and magneto-dielectric properties in PVDF-BaFe<sub>12</sub>O<sub>19</sub>composites: A step towards miniaturized electronic devices." *RSC Adv.*, 6 (19), 16073–16080.

Athanasekou, C., Sapalidis, A., Katris, I., Savopoulou, E., Beltsios, K., Tsoufis, T., Kaltzoglou, A., Falaras, P., Bounos, G., Antoniou, M., Boutikos, P. and Romanos, G.E. (2019). "Mixed Matrix PVDF/Graphene and Composite-Skin PVDF/Graphene Oxide Membranes Applied in Membrane Distillation." *Polym. Eng. Sci.*, 59 (S1), E262–E278.

Bairagi, S. and Ali, S.W. (2019a). "Influence of High Aspect Ratio Lead-Free Piezoelectric Fillers in Designing Flexible Fibrous Nanogenerators: Demonstration of Significant High Output Voltage." *Energy Technol.*, 7 (10), 1–10.

Bairagi, S. and Ali, S.W. (2019b). "Poly (vinylidene fluoride) (PVDF)/Potassium Sodium Niobate (KNN) nanorods based flexible nanocomposite film: Influence of KNN concentration in the performance of nanogenerator." *Org. Electron.*, 105547.

Bairagi, S. and Ali, S.W. (2020). "Flexible lead-free PVDF/SM-KNN electrospun nanocomposite based piezoelectric materials: Significant enhancement of energy harvesting efficiency of the nanogenerator." *Energy*, 198 117385.

Baji, A., Mai, Y.W., Li, Q. and Liu, Y. (2011a). "Electrospinning induced ferroelectricity in poly(vinylidene fluoride) fibers." *Nanoscale*, 3 (8), 3068–3071.

Baji, A., Mai, Y.W., Li, Q. and Liu, Y. (2011b). "Nanoscale investigation of ferroelectric properties in electrospun barium titanate/polyvinylidene fluoride

composite fibers using piezoresponse force microscopy." *Compos. Sci. Technol.*, 71 (11), 1435–1440.

Barstugan, R., Barstugan, M. and Ozaytekin, I. (2019). "PBO/graphene added  $\beta$ -PVDF piezoelectric composite nanofiber production." *Compos. Part B Eng.*, 158 (August 2018), 141–148.

Barua, B. and Saha, M.C. (2015). "Investigation on jet stability, fiber diameter, and tensile properties of electrospun polyacrylonitrile nanofibrous yarns." *J. Appl. Polym. Sci.*, 132 (18), 41918.

Beattie, D.A., Addai-Mensah, J., Beaussart, A., Franks, G. V. and Yeap, K.Y. (2014). "In situ particle film ATR FTIR spectroscopy of poly (N-isopropyl acrylamide) (PNIPAM) adsorption onto talc." *Phys. Chem. Chem. Phys.*, 16 (45), 25143–25151.

Behzadi, M., Mahmoodi Hashemi, M., Rognizadeh, M., Nasiri, S. and Ramazani Saadatabadi, A. (2021). "Copper(ii) ions supported on functionalized graphene oxide: an organometallic nanocatalyst for oxidative amination of azoles via C-H/C-N bond activation." *New J. Chem.*, 45 (6), 3242–3251.

Benz, M., Euler, W.B. and Gregory, O.J. (2002). "The role of solution phase water on the deposition of thin films of poly(vinylidene fluoride)." *Macromolecules*, 35 (7), 2682–2688.

Bhardwaj, N. and Kundu, S.C. (2010). "Electrospinning: A fascinating fiber fabrication technique." *Biotechnol. Adv.*, 28 (3), 325–347.

Bhimireddi, R., Ponraj, B. and Varma, K.B.R. (2016). "Structural, Optical, and Piezoelectric Response of Lead-Free  $\text{Ba}_{0.95}\text{Mg}_{0.05}\text{Zr}_{0.1}\text{Ti}_{0.9}\text{O}_3$  Nanocrystalline Powder." *J. Am. Ceram. Soc.*, 99 (3), 896–904.

Biswas, A., Garain, S., Maity, K., Henkel, K., Schmeißer, D. and Mandal, D. (2019). "Influence of *in situ* synthesized bismuth oxide nanostructures in self-poled PVDF-based nanogenerator for mechanical energy harvesting application." *Polym. Compos.*, 40 (S1), E265–E274.

Botelho, G., Lanceros-Mendez, S., Gonçalves, A.M., Sencadas, V. and Rocha, J.G. (2008). "Relationship between processing conditions, defects and thermal degradation of poly(vinylidene fluoride) in the  $\beta$ -phase." *J. Non. Cryst. Solids*, 354 (1), 72–78.

Cai, X., Lei, T., Sun, D. and Lin, L. (2017a). "A critical analysis of the  $\alpha$ ,  $\beta$  and  $\gamma$  phases in poly(vinylidene fluoride) using FTIR." *RSC Adv.*, 7 (25), 15382–15389.

Caliò, R., Rongala, U.B., Camboni, D., Milazzo, M., Stefanini, C., Petris, G. de and Oddo, C.M. (2014). "Piezoelectric energy harvesting solutions." *Sensors (Switzerland)*, 14 (3), 4755–4790.

Chhetri, S., Kuila, T. and Murmu, N.C. (2016). Graphene Composites. In *Graphene Technology: From Laboratory to Fabrication*, (wiley), 63–111.

Chi, Q., Zhou, Y., Yin, C., Zhang, Y., Zhang, C., Zhang, T., Feng, Y., Zhang, Y. and Chen, Q. (2019). "A blended binary composite of poly(vinylidene fluoride) and poly(methyl methacrylate) exhibiting excellent energy storage performances." *J. Mater. Chem. C*, 7 (45), 14148–14158.

Coates, J. (2006). Interpretation of Infrared Spectra, A Practical Approach. In *Encyclopedia of Analytical Chemistry*, (John Wiley & Sons, Ltd), 1-23.

Costa, C.M., Sencadas, V., Pelicano, I., Martins, F., Rocha, J.G. and Lanceros-Mendez, S. (2008a). "Microscopic origin of the high-strain mechanical response of poled and non-poled poly(vinylidene fluoride) in the  $\beta$ -phase." *J. Non. Cryst. Solids*, 354 (32), 3871–3876.

Costa, F.R., Leuteritz, A., Wagenknecht, U., Jehnichen, D., Häußler, L. and Heinrich, G. (2008b). "Intercalation of Mg-Al layered double hydroxide by anionic surfactants: Preparation and characterization." *Appl. Clay Sci.*, 38 (3–4), 153–164.

Cozza, E.S., Monticelli, O., Marsano, E. and Cebe, P. (2013). "On the electrospinning of PVDF: influence of the experimental conditions on the nanofiber properties." *Polym. Int.*, 62 (1), 41–48.

Davis, G.T., McKinney, J.E., Broadhurst, M.G. and Roth, S.C. (1978). "Electric-field-

induced phase changes in poly(vinylidene fluoride)." *J. Appl. Phys.*, 49 (10), 4998–5002.

Deitzel, J.M., Kleinmeyer, J., Harris, D. and Beck Tan, N.C. (2001). "The effect of processing variables on the morphology of electrospun nanofibers and textiles." *Polymer (Guildf.)*, 42 (1), 261–272.

Demir, M.M., Yilgor, I., Yilgor, E. and Erman, B. (2002). "Electrospinning of polyurethane fibers." *Polymer (Guildf.)*, 43 (11), 3303–3309.

Denishev, K. (2016). "Some metal oxides and their applications for creation of Microsystems (MEMS) and Energy Harvesting Devices (EHD)." *J. Phys. Conf. Ser.*, 764 (1), 012003.

Dhakras, D., Borkar, V., Ogale, S. and Jog, J. (2012). "Enhanced piezoresponse of electrospun PVDF mats with a touch of nickel chloride hexahydrate salt." *Nanoscale*, 4 (3), 752–756.

Ding, R., Liu, H., Zhang, X., Xiao, J., Kishor, R., Sun, H., Zhu, B., Chen, G., Gao, F., Feng, X., Chen, J., Chen, X., Sun, X. and Zheng, Y. (2016). "Flexible Piezoelectric Nanocomposite Generators Based on Formamidinium Lead Halide Perovskite Nanoparticles." *Adv. Funct. Mater.*, 26 (42), 7708–7716.

Dutta, B., Kar, E., Bose, N. and Mukherjee, S. (2015). "Significant enhancement of the electroactive  $\beta$ -phase of PVDF by incorporating hydrothermally synthesized copper oxide nanoparticles." *RSC Adv.*, 5 (127), 105422–105434.

Egusa, S., Wang, Z., Chocat, N., Ruff, Z.M., Stolyarov, A.M., Shemuly, D., Sorin, F., Rakich, P.T., Joannopoulos, J.D. and Fink, Y. (2010). "Multimaterial piezoelectric fibres." *Nat. Mater.*, 9 (8), 643–648.

Esterly, D.M. and Love, B.J. (2004). "Phase transformation to  $\beta$ -poly(vinylidene fluoride) by milling." *J. Polym. Sci. Part B Polym. Phys.*, 42 (1), 91–97.

Fakhri, P., Amini, B., Bagherzadeh, R., Kashfi, M., Latifi, M., Yavari, N., Asadi Kani, S. and Kong, L. (2019). "Flexible hybrid structure piezoelectric nanogenerator

based on ZnO nanorod/PVDF nanofibers with improved output." *RSC Adv.*, 9 (18), 10117–10123.

Fong, H., Chun, I. and Reneker, D.H. (1999). Beaded nanofibers formed during electrospinning. In *Polymer*, (Elsevier Science Ltd), 4585–4592.

Frenot, A. and Chronakis, I.S. (2003). "Polymer nanofibers assembled by electrospinning." *Curr. Opin. Colloid Interface Sci.*, 8 (1), 64–75.

Fu, C., Zhao, G., Zhang, H. and Li, S. (2013). "Evaluation and characterization of reduced graphene oxide nanosheets as anode materials for lithium-ion batteries." *Int. J. Electrochem. Sci.*, 8, 6269 – 6280.

Gaur, A., Rana, D. and Maiti, P. (2019). "Mechanical and wear behaviour of poly(vinylidene fluoride)/clay nanocomposite." *J. Mater. Res. Technol.*, 8 (6), 5874–5881.

Ganeshkumar, R., Cheah, C.W., Xu, R., Kim, S.-G. and Zhao, R. (2017). "A high output voltage flexible piezoelectric nanogenerator using porous lead-free KNbO<sub>3</sub> nanofibers." *Appl. Phys. Lett.*, 111 (1), 13905.

Gebrekrstos, A., Madras, G. and Bose, S. (2018). "Piezoelectric Response in Electrospun Poly(vinylidene fluoride) Fibers Containing Fluoro-Doped Graphene Derivatives." *ACS Omega*, 3 (5), 5317–5326.

Ghosh, S.K. and Mandal, D. (2018). "Synergistically enhanced piezoelectric output in highly aligned 1D polymer nanofibers integrated all-fiber nanogenerator for wearable nano-tactile sensor." *Nano Energy*, 53, 245–257.

Ghosh, S.K., Sinha, T.K., Mahanty, B. and Mandal, D. (2015). "Self-poled Efficient Flexible 'Ferroelectric' Nanogenerator: A New Class of Piezoelectric Energy Harvester." *Energy Technol.*, 3 (12), 1190–1197.

Gong, X., Chen, Y., Tang, C.-Y., Law, W.-C., Chen, L., Wu, C., Hu, T. and Tsui, G.C.P. (2018). "Crystallinity and morphology of barium titanate filled poly(vinylidene fluoride) nanocomposites." *J. Appl. Polym. Sci.*, 135 (48), 46877.

Gregorio, Jr., R. and Cestari, M. (1994). "Effect of crystallization temperature on the crystalline phase content and morphology of poly(vinylidene fluoride)." *J. Polym. Sci. Part B Polym. Phys.*, 32 (5), 859–870.

Gregorio, R. (2006). "Determination of the  $\alpha$ ,  $\beta$ , and  $\gamma$  crystalline phases of poly(vinylidene fluoride) films prepared at different conditions." *J. Appl. Polym. Sci.*, 100 (4), 3272–3279.

Griffete, N., Dechézelles, J.F. and Scheffold, F. (2012). "Dense covalent attachment of magnetic iron oxide nanoparticles onto silica particles using a diazonium salt chemistry approach." *Chem. Commun.*, 48 (92), 11364–11366.

Guo, R., Qi, L., Mo, Z., Wu, Q. and Yang, S. (2017). "A new route to synthesize polyaniline-grafted carboxyl-functionalized graphene composite materials with excellent electrochemical performance." *Iran. Polym. J. (English Ed.)*, 26 (6), 423–430.

Han, J.K., Jeon, D.H., Cho, S.Y., Kang, S.W., Yang, S.A., Bu, S.D., Myung, S., Lim, J., Choi, M., Lee, M. and Lee, M.K. (2016). "Nanogenerators consisting of direct-grown piezoelectrics on multi-walled carbon nanotubes using flexoelectric effects." *Sci. Rep.*, 6 (1), 1–8.

He, X. and Yao, K. (2006). "Crystallization mechanism and piezoelectric properties of solution-derived ferroelectric poly(vinylidene fluoride) thin films." *Appl. Phys. Lett.*, 89 (11), 1–4.

Hosseini, S.M. and Yousefi, A.A. (2017). "Piezoelectric sensor based on electrospun PVDF-MWCNT-Cloisite 30B hybrid nanocomposites." *Org. Electron.*, 50 121–129.

Hu, P., Yan, L., Zhao, C., Zhang, Y. and Niu, J. (2018). "Double-layer structured PVDF nanocomposite film designed for flexible nanogenerator exhibiting enhanced piezoelectric output and mechanical property." *Compos. Sci. Technol.*, 168 327–335.

Huang, Z.M., Zhang, Y.Z., Kotaki, M. and Ramakrishna, S. (2003). "A review on polymer nanofibers by electrospinning and their applications in nanocomposites."

*Compos. Sci. Technol.*, 63 (15), 2223–2253.

Hummers, W.S. and Offeman, R.E. (1958). "Preparation of Graphitic Oxide." *J. Am. Chem. Soc.*, 80 (6), 1339.

Ico, G., Showalter, A., Bosze, W., Gott, S.C., Kim, B.S., Rao, M.P., Myung, N. V. and Nam, J. (2016). "Size-dependent piezoelectric and mechanical properties of electrospun P(VDF-TrFE) nanofibers for enhanced energy harvesting." *J. Mater. Chem. A*, 4 (6), 2293–2304.

Islam, A., Khan, A.N., Shakir, M.F. and Islam, K. (2019). "Strengthening of  $\beta$  polymorph in PVDF/FLG and PVDF/GO nanocomposites." *Mater. Res. Express*, 7 (1), 15017.

Ismail, A.M., Mohammed, M.I. and Fouad, S.S. (2018). "Optical and structural properties of polyvinylidene fluoride (PVDF) / reduced graphene oxide (RGO) nanocomposites." *J. Mol. Struct.*, 1170 51–59.

Issa, A., Al-Maadeed, M., Luyt, A., Ponnamma, D. and Hassan, M. (2017). "Physico-Mechanical, Dielectric, and Piezoelectric Properties of PVDF Electrospun Mats Containing Silver Nanoparticles." *C*, 3 (4), 30.

Jahan, N., Mighri, F., Rodrigue, D. and Ajji, A. (2018). "Synergistic improvement of piezoelectric properties of PVDF/ CaCO<sub>3</sub>/montmorillonite hybrid nanocomposites." *Appl. Clay Sci.*, 152 (October 2017), 93–100.

Jayakumar, O.D., Mandal, B.P., Majeed, J., Lawes, G., Naik, R. and Tyagi, A.K. (2013). "Inorganic–organic multiferroic hybrid films of Fe<sub>3</sub>O<sub>4</sub> and PVDF with significant magneto-dielectric coupling." *J. Mater. Chem. C*, 1 (23), 3710.

Jiang, Y., Ye, Y., Yu, J., Wu, Z., Li, W., Xu, J. and Xie, G. (2007). "Study of thermally poled and corona charged poly(vinylidene fluoride) films." *Polym. Eng. Sci.*, 47 (9), 1344–1350.

Jiao, X., Qiu, Y., Zhang, L. and Zhang, X. (2017). "Comparison of the characteristic properties of reduced graphene oxides synthesized from natural graphites with



different graphitization degrees." *RSC Adv.*, 7 (82), 52337–52344.

Jiyong, H., Yinda, Z., Hele, Z., Yuanyuan, G. and Xudong, Y. (2017). " Mixed effect of main electrospinning parameters on the  $\beta$ -phase crystallinity of electrospun PVDF nanofibers ." *Smart Mater. Struct.*, 26 (8), 85019.

Kar, E., Bose, N., Das, S., Mukherjee, N. and Mukherjee, S. (2015). "Enhancement of electroactive  $\beta$  phase crystallization and dielectric constant of PVDF by incorporating  $\text{GeO}_2$  and  $\text{SiO}_2$  nanoparticles." *Phys. Chem. Chem. Phys.*, 17 (35), 22784–22798.

Karan, S.K., Mandal, D. and Khatua, B.B. (2015). "Self-powered flexible Fe-doped RGO/PVDF nanocomposite: An excellent material for a piezoelectric energy harvester." *Nanoscale*, 7 (24), 10655–10666.

Kenry and Lim, C.T. (2017). "Nanofiber technology: current status and emerging developments." *Prog. Polym. Sci.*, 70, 1–17.

Khalifa, M. and Anandhan, S. (2019). "PVDF Nanofibers with Embedded Polyaniline-Graphitic Carbon Nitride Nanosheet Composites for Piezoelectric Energy Conversion." *ACS Appl. Nano Mater.*, 2 (11), 7328–7339.

Khalifa, M., Mahendran, A. and Anandhan, S. (2016). "Probing the synergism of halloysite nanotubes and electrospinning on crystallinity, polymorphism and piezoelectric performance of poly(vinylidene fluoride)." *RSC Adv.*, 6 (115), 114052–114060.

Khalifa, M., Mahendran, A. and Anandhan, S. (2019). "Durable, efficient, and flexible piezoelectric nanogenerator from electrospun PANi/HNT/PVDF blend nanocomposite." *Polym. Compos.*, 40 (4), 1663–1675.

Khalili, D. (2016). "Graphene oxide: A promising carbocatalyst for the regioselective thiocyanation of aromatic amines, phenols, anisols and enolizable ketones by hydrogen peroxide/KSCN in water." *New J. Chem.*, 40 (3), 2547–2553.

Kim, H.S., Kim, J.H. and Kim, J. (2011a). "A review of piezoelectric energy harvesting based on vibration." *Int. J. Precis. Eng. Manuf.*, 12 (6), 1129–1141.

Kim, S.H., Park, S.J., Cho, C.Y., Kang, H.S., Sohn, E.H., Park, I.J., Ha, J.W. and Lee, S.G. (2019). "Preparation and electroactive phase adjustment of Ag-doped poly(vinylidene fluoride) (PVDF) films." *RSC Adv.*, 9 (69), 40286–40291.

Kim, Y.J., Ahn, C.H., Lee, M.B. and Choi, M.S. (2011b). "Characteristics of electrospun PVDF/SiO<sub>2</sub> composite nanofiber membranes as polymer electrolyte." *Mater. Chem. Phys.*, 127 (1–2), 137–142.

Kosmynin, B.P. and Gal'perin, E.L. (1973). "Effect of gamma radiation on the mechanical properties of polyvinylidene fluoride." *Polym. Mech.*, 9 (1), 126–129.

Lee, C., Wood, D., Edmondson, D., Yao, D., Erickson, A.E., Tsao, C.T., Revia, R.A., Kim, H. and Zhang, M. (2016). "Electrospun uniaxially-aligned composite nanofibers as highly-efficient piezoelectric material." *Ceram. Int.*, 42 (2), 2734–2740.

Lee, H., Nagaishi, T., Phan, D.N., Kim, M., Zhang, K.Q., Wei, K. and Kim, I.S. (2017). "Effect of graphene incorporation in carbon nanofiber decorated with TiO<sub>2</sub> for photoanode applications." *RSC Adv.*, 7 (11), 6574–6582.

Lee, J.S., Choi, K.H., Ghim, H. Do, Kim, S.S., Chun, D.H., Kim, H.Y. and Lyoo, W.S. (2004). "Role of molecular weight of atactic poly(vinyl alcohol) (PVA) in the structure and properties of PVA nanofabric prepared by electrospinning." *J. Appl. Polym. Sci.*, 93 (4), 1638–1646.

Li, H., Tian, C. and Deng, Z.D. (2014). "Energy harvesting from low frequency applications using piezoelectric materials." *Appl. Phys. Rev.*, 1 (4), 0–20.

Li, J., Chen, S., Liu, W., Fu, R., Tu, S., Zhao, Y., Dong, L., Yan, B. and Gu, Y. (2019). "High Performance Piezoelectric Nanogenerators Based on Electrospun ZnO Nanorods/Poly(vinylidene fluoride) Composite Membranes." *J. Phys. Chem. C*, 123 (18), 11378–11387.

Li, J., Khanchaitit, P., Han, K. and Wang, Q. (2010). "New Route Toward High-Energy-Density Nanocomposites Based on Chain-End Functionalized Ferroelectric Polymers." *Chem. Mater.*, 22 (18), 5350–5357.

Li, M., Stingelin, N., Michels, J.J., Spijkman, M.J., Asadi, K., Feldman, K., Blom, P.W.M. and Leeuw, D.M. De (2012). "Ferroelectric phase diagram of PVDF:PMMA." *Macromolecules*, 45 (18), 7477–7485.

Li, R., Hu, Z., Shao, X., Cheng, P., Li, S., Yu, W., Lin, W. and Yuan, D. (2016). "Large scale synthesis of NiCo layered double hydroxides for superior asymmetric electrochemical capacitor." *Sci. Rep.*, 6, 1–9.

Lin, J., Ding, B., Jianyong, Y. and Hsieh, Y. (2010). "Direct fabrication of highly nanoporous polystyrene fibers via electrospinning." *ACS Appl. Mater. Interfaces*, 2 (2), 521–528.

Liu, H., Zhong, J., Lee, C., Lee, S.W. and Lin, L. (2018). "A comprehensive review on piezoelectric energy harvesting technology: Materials, mechanisms, and applications." *Appl. Phys. Rev.*, 5 (4), 04136.

Liu, J., Lu, X. and Wu, C. (2013). "Effect of preparation methods on crystallization behavior and tensile strength of poly(vinylidene fluoride) membranes." *Membranes (Basel)*, 3 (4), 389–405.

Lopes, A.C., Carabineiro, S.A.C., Pereira, M.F.R., Botelho, G. and Lanceros-Mendez, S. (2013). "Nanoparticle Size and Concentration Dependence of the Electroactive Phase Content and Electrical and Optical Properties of Ag/Poly(vinylidene fluoride) Composites." *ChemPhysChem*, 14 (9), 1926–1933.

López Guerra, E., Shanmugaraj, A.M., Choi, W.S. and Ryu, S.H. (2013). "Thermally reduced graphene oxide-supported nickel catalyst for hydrogen production by propane steam reforming." *Appl. Catal. A Gen.*, 468, 467–474.

Lovinger, A.J. (1980). "Crystallization and morphology of melt-solidified poly(vinylidene fluoride)." *J. Polym. Sci. Part A-2, Polym. Phys.*, 18 (4), 793–809.

Lovinger, A.J. (1981). "Conformational defects and associated molecular motions in crystalline poly(vinylidene fluoride)." *J. Appl. Phys.*, 52 (10), 5934–5938.

Lovinger, A.J. (1982). "Annealing of Poly(vinylidene fluoride) and Formation of a

Fifth Phase." *Macromolecules*, 15 (1), 40–44.

Lovinger, A.J. (1983). "Ferroelectric polymers." *Science* (80), 220 (4602), 1115–1121.

Lund, A. and Hagström, B. (2011). "Melt spinning of  $\beta$ -phase poly(vinylidene fluoride) yarns with and without a conductive core." *J. Appl. Polym. Sci.*, 120 (2), 1080–1089.

Mahdavi Varposhti, A., Yousefzadeh, M., Kowsari, E. and Latifi, M. (2020). "Enhancement of  $\beta$ -Phase Crystalline Structure and Piezoelectric Properties of Flexible PVDF/Ionic Liquid Surfactant Composite Nanofibers for Potential Application in Sensing and Self-Powering." *Macromol. Mater. Eng.*, 305 (3), 1900796.

Maity, K., Mahanty, B., Sinha, T.K., Garain, S., Biswas, A., Ghosh, S.K., Manna, S., Ray, S.K. and Mandal, D. (2017). "Two-Dimensional Piezoelectric MoS<sub>2</sub>-Modulated Nanogenerator and Nanosensor Made of Poly(vinylidene Fluoride) Nanofiber Webs for Self-Powered Electronics and Robotics." *Energy Technol.*, 5 (2), 234–243.

Mandal, A. and Nandi, A.K. (2013). "Ionic liquid integrated multiwalled carbon nanotube in a poly(vinylidene fluoride) matrix: Formation of a piezoelectric  $\beta$ -polymorph with significant reinforcement and conductivity improvement." *ACS Appl. Mater. Interfaces*, 5 (3), 747–760.

Mansouri, S., Sheikholeslami, T.F. and Behzadmehr, A. (2019). "Investigation on the electrospun PVDF/NP-ZnO nanofibers for application in environmental energy harvesting." *J. Mater. Res. Technol.*, 8 (2), 1608–1615.

Martins, P., Lopes, A.C. and Lanceros-Mendez, S. (2014). "Electroactive phases of poly(vinylidene fluoride): Determination, processing and applications." *Prog. Polym. Sci.*, 39 (4), 683–706.

Matsushige, K. and Takemura, T. (1978). "Melting and crystallization of poly(vinylidene fluoride) under high pressure." *J Polym Sci Polym Phys Ed*, 16 (5),

921–934.

Matsushige, K. and Takemura, T. (1980). "Crystallization of macromolecules under high pressure." *J. Cryst. Growth*, 48 (2), 343–354.

Matthews, J.A., Wnek, G.E., Simpson, D.G. and Bowlin, G.L. (2002). "Electrospinning of collagen nanofibers." *Biomacromolecules*, 3 (2), 232–238.

Mazinani, S., Aji, A. and Dubois, C. (2009). "Morphology, structure and properties of conductive PS/CNT nanocomposite electrospun mat." *Polymer (Guildf.)*, 50 (14), 3329–3342.

McGrath, J.C. and Ward, I.M. (1980). "High effective draw as a route to increased stiffness and electrical response in poly(vinylidene fluoride)." *Polym. (United Kingdom)*, 21 (8), 855–857.

McKee, M.G., Wilkes, G.L., Colby, R.H. and Long, T.E. (2004). "Correlations of Solution Rheology with Electrospun Fiber Formation of Linear and Branched Polyesters." *Macromolecules*, 37 (5), 1760–1767.

Mirjalili, M. and Zohoori, S. (2016). "Review for application of electrospinning and electrospun nanofibers technology in textile industry." *J. Nanostructure Chem.*, 6 (3), 207–213.

Mirza-Aghayan, M., Molaee Tavana, M. and Boukherroub, R. (2016). "Sulfonated reduced graphene oxide as a highly efficient catalyst for direct amidation of carboxylic acids with amines using ultrasonic irradiation." *Ultrason. Sonochem.*, 29 371–379.

Mishra, S., Unnikrishnan, L., Nayak, S.K. and Mohanty, S. (2019). "Advances in Piezoelectric Polymer Composites for Energy Harvesting Applications: A Systematic Review." *Macromol. Mater. Eng.*, 304 (1), 1–25.

Mokhtari, F., Shamshirsaz, M. and Latifi, M. (2016). "Investigation of  $\beta$  phase formation in piezoelectric response of electrospun polyvinylidene fluoride nanofibers: LiCl additive and increasing fibers tension." *Polym. Eng. Sci.*, 56 (1), 61–70.

- Morsy, A.M.A. (2017). "Performance of magnetic talc titanium oxide composite for thorium ions adsorption from acidic solution." *Environ. Technol. Innov.*, 8 399–410.
- Na, H., Chen, P., Wong, S.C., Hague, S. and Li, Q. (2012). "Fabrication of PVDF/PVA microtubules by coaxial electrospinning." *Polymer (Guildf)*., 53 (13), 2736–2743.
- Naegele, D., Yoon, D.Y. and Broadhurst, M.G. (1978). "Formation of a New Crystal Form ( $\alpha_p$ ) of Poly(vinylidene fluoride) under Electric Field." *Macromolecules*, 11 (6), 1297–1298.
- Nayak, R., Padhye, R., Kyratzis, I.L., Truong, Y.B. and Arnold, L. (2012). "Recent advances in nanofibre fabrication techniques." *Text. Res. J.*, 82 (2), 129–147.
- Nethravathi, C. and Rajamathi, M. (2008). "Chemically modified graphene sheets produced by the solvothermal reduction of colloidal dispersions of graphite oxide." *Carbon N. Y.*, 46 (14), 1994–1998.
- Newman, B.A. and Scheinbeim, J.I. (1983). "Polarization Mechanisms in Phase II Poly(vinylidene fluoride) Films." *Macromolecules*, 16 (1), 60–68.
- Parangusan, H., Ponnamma, D. and Ali Almaadeed, M. Al (2019). "Toward High Power Generating Piezoelectric Nanofibers: Influence of Particle Size and Surface Electrostatic Interaction of Ce-Fe<sub>2</sub>O<sub>3</sub> and Ce-Co<sub>3</sub>O<sub>4</sub> on PVDF." *ACS Omega*, 4 (4), 6312–6323.
- Park, S., An, J., Jung, I., Piner, R.D., An, S.J., Li, X., Velamakanni, A. and Ruoff, R.S. (2009). "Colloidal suspensions of highly reduced graphene oxide in a wide variety of organic solvents." *Nano Lett.*, 9 (4), 1593–1597.
- Patro, T.U., Mhalgi, M. V., Khakhar, D.V. and Misra, A. (2008). "Studies on poly(vinylidene fluoride)–clay nanocomposites: Effect of different clay modifiers." *Polymer (Guildf)*., 49 (16), 3486–3499.
- Pavlič, J., Malič, B. and Rojac, T. (2014). "Small reduction of the piezoelectric  $d_{33}$  response in potassium sodium niobate thick films." *J. Am. Ceram. Soc.*, 97 (5), 1497–

1503.

Peng, Q.-Y., Cong, P.-H., Liu, X.-J., Liu, T.-X., Huang, S. and Li, T.-S. (2009). "The preparation of PVDF/clay nanocomposites and the investigation of their tribological properties." *Wear*, 266 (7–8), 713–720.

Persano, L., Dagdeviren, C., Su, Y., Zhang, Y., Girardo, S., Pisignano, D., Huang, Y. and Rogers, J.A. (2013). "High performance piezoelectric devices based on aligned arrays of nanofibers of poly(vinylidene fluoride-co-trifluoroethylene)." *Nat. Commun.*, 4 (1), 1–10.

Pickford, T., Gu, X., Heeley, E.L. and Wan, C. (2019). "Effects of an ionic liquid and processing conditions on the  $\beta$ -polymorph crystal formation in poly(vinylidene fluoride)." *CrystEngComm*, 21 (36), 5418–5428.

Prado, M.A., Dias, G., Carone, C., Ligabue, R., Dumas, A., Roux, C. Le, Micoud, P., Martin, F. and Einloft, S. (2015). "Synthetic Ni-talc as filler for producing polyurethane nanocomposites." *J. Appl. Polym. Sci.*, 132 (16), 41854.

Pramoda, K.P., Mohamed, A., Phang, I.Y. and Liu, T. (2005). "Crystal transformation and thermomechanical properties of poly(vinylidene fluoride)/clay nanocomposites." *Polym. Int.*, 54 (1), 226–232.

Prest, W.M. and Luca, D.J. (1978). "The formation of the  $\gamma$  phase from the  $\alpha$  and  $\beta$  polymorphs of polyvinylidene fluoride." *J. Appl. Phys.*, 49 (10), 5042–5047.

Qi, Y. and McAlpine, M.C. (2010). "Nanotechnology-enabled flexible and biocompatible energy harvesting." *Energy Environ. Sci.*, 3 (9), 1275–1285.

Qiu, F., Wang, M., Hao, Y. and Guo, S. (2014). "The effect of talc orientation and transcrystallization on mechanical properties and thermal stability of the polypropylene/talc composites." *Compos. Part A Appl. Sci. Manuf.*, 58, 7–15.

Rahman, W., Ghosh, S.K., Middy, T.R. and Mandal, D. (2017). "Highly durable piezo-electric energy harvester by a super toughened and flexible nanocomposite: Effect of laponite nano-clay in poly(vinylidene fluoride)." *Mater. Res. Express*, 4 (9),

095305.

Ramasundaram, S., Yoon, S., Kim, K.J. and Lee, J.S. (2008a). "Direct preparation of nanoscale thin films of poly(vinylidene fluoride) containing  $\beta$ -crystalline phase by heat-controlled spin coating." *Macromol. Chem. Phys.*, 209 (24), 2516–2526.

Ramasundaram, S., Yoon, S., Kim, K.J. and Park, C. (2008b). "Preferential formation of electroactive crystalline phases in poly(vinylidene fluoride)/organically modified silicate nanocomposites." *J. Polym. Sci. Part B Polym. Phys.*, 46 (20), 2173–2187.

Ren, X., Fan, H., Zhao, Y. and Liu, Z. (2016). "Flexible Lead-Free BiFeO<sub>3</sub>/PDMS-Based Nanogenerator as Piezoelectric Energy Harvester." *ACS Appl. Mater. Interfaces*, 8 (39), 26190–26197.

Ribeiro, C., Sencadas, V., Luís, J., Ribelles, G., Ribeiro, C., Sencadas, V., Luís, J. and Ribelles, G. (2010). "Influence of Processing Conditions on Polymorphism and Nanofiber Morphology of Electroactive Poly(vinylidene fluoride) Electrospun Membranes." *Soft Materials*, 8(3), 274-287.

Rieger, K.A., Birch, N.P. and Schiffman, J.D. (2013). "Designing electrospun nanofiber mats to promote wound healing-a review." *J. Mater. Chem. B*, 1 (36), 4531–4541.

Ryu, S.H., Sin, J.H. and Shanmugaraj, A.M. (2014). "Study on the effect of hexamethylene diamine functionalized graphene oxide on the curing kinetics of epoxy nanocomposites." *Eur. Polym. J.*, 52 (1), 88–97.

Salimi, A. and Yousefi, A.A. (2003). "FTIR studies of  $\beta$ -phase crystal formation in stretched PVDF films." *Polym. Test.*, 22 (6), 699–704.

Samadi, A., Ahmadi, R. and Hosseini, S.M. (2019). "Influence of TiO<sub>2</sub>-Fe<sub>3</sub>O<sub>4</sub>-MWCNT hybrid nanotubes on piezoelectric and electromagnetic wave absorption properties of electrospun PVDF nanocomposites." *Org. Electron.*, 75, 105405.

Samadi, A., Hosseini, S.M. and Mohseni, M. (2018). "Investigation of the electromagnetic microwaves absorption and piezoelectric properties of electrospun



Fe<sub>3</sub>O<sub>4</sub>-GO/PVDF hybrid nanocomposites." *Org. Electron.*, 59, 149–155.

Samsonowicz, M., Hrynaskiewicz, T., Świsłocka, R., Regulska, E. and Lewandowski, W. (2005). "Experimental and theoretical IR, Raman, NMR spectra of 2-, 3- and 4-aminobenzoic acids." *In Journal of Molecular Structure*, (Elsevier), 345–352.

Schlaberg, H.I. and Duffy, J.S. (1994). "Piezoelectric polymer composite arrays for ultrasonic medical imaging applications." *Sensors Actuators A. Phys.*, 44 (2), 111–117.

Schneider, J.J., Engstler, J., Franzka, S., Hofmann, K., Albert, B., Ensling, J., Gütlich, P., Hildebrandt, P., Döpner, S., Pfleging, W., Günther, B. and Müller, G. (2001). "Carbon nanotube bags: Catalytic formation, physical properties, two-dimensional alignment and geometric structuring of densely filled carbon tubes." *Chem. - A Eur. J.*, 7 (13), 2888–2895.

Sencadas, V., Gregorio, R. and Lanceros-Méndez, S. (2009). " $\alpha$  to  $\beta$  Phase Transformation and Microstructural Changes of PVDF Films Induced by Uniaxial Stretch." *J. Macromol. Sci. Part B*, 48 (3), 514–525.

Senthil Kumar, R., Sarathi, T., Venkataraman, K.K. and Bhattacharyya, A. (2019). "Enhanced piezoelectric properties of polyvinylidene fluoride nanofibers using carbon nanofiber and electrical poling." *Mater. Lett.*, 255 126515.

Shamitha, C., Mahendran, A. and Anandhan, S. (2020). "Effect of polarization switching on piezoelectric and dielectric performance of electrospun nanofabrics of poly(vinylidene fluoride)/Ca–Al LDH nanocomposite." *J. Appl. Polym. Sci.*, 137 (20), 1–12.

Shan, C., Wang, Y., Xie, S., Guan, H.Y., Argueta, M. and Yue, Y. (2019). "Free-standing nitrogen-doped graphene-carbon nanofiber composite mats: electrospinning synthesis and application as anode material for lithium-ion batteries." *J. Chem. Technol. Biotechnol.*, 94 (12), 3793–3799.

Shao, H., Fang, J., Wang, H. and Lin, T. (2015). "Effect of electrospinning parameters and polymer concentrations on mechanical-to-electrical energy conversion of randomly-oriented electrospun poly(vinylidene fluoride) nanofiber mats." *RSC Adv.*, 5 (19), 14345–14350.

Sharma, M., Madras, G. and Bose, S. (2015). "Contrasting Effects of Graphene Oxide and Poly(ethylenimine) on the Polymorphism in Poly(vinylidene fluoride)." *Cryst. Growth Des.*, 15 (7), 3345–3355.

Sharma, M., Srinivas, V., Madras, G. and Bose, S. (2016). "Outstanding dielectric constant and piezoelectric coefficient in electrospun nanofiber mats of PVDF containing silver decorated multiwall carbon nanotubes: Assessing through piezoresponse force microscopy." *RSC Adv.*, 6 (8), 6251–6258.

Shetty, S., Mahendran, A. and Anandhan, S. (2020). "Development of a new flexible nanogenerator from electrospun nanofabric based on PVDF/talc nanosheet composites." *Soft Matter*, 16 (24), 5679–5688.

Shi, K., Sun, B., Huang, X. and Jiang, P. (2018). "Synergistic effect of graphene nanosheet and BaTiO<sub>3</sub> nanoparticles on performance enhancement of electrospun PVDF nanofiber mat for flexible piezoelectric nanogenerators." *Nano Energy*, 52, 153–162.

Sultana, A., Alam, M.M., Sadhukhan, P., Ghorai, U.K., Das, S., Middy, T.R. and Mandal, D. (2018). "Organo-lead halide perovskite regulated green light emitting poly(vinylidene fluoride) electrospun nanofiber mat and its potential utility for ambient mechanical energy harvesting application." *Nano Energy*, 49, 380–392.

Sun, B., Li, X., Zhao, R., Ji, H., Qiu, J., Zhang, N., He, D. and Wang, C. (2019). "Electrospun poly(vinylidene fluoride)-zinc oxide hierarchical composite fiber membrane as piezoelectric acoustoelectric nanogenerator." *J. Mater. Sci.*, 54 (3), 2754–2762.

Taylor, G. (1969). "Electrically Driven Jets." *Proc. R. Soc. A Math. Phys. Eng. Sci.*, 313 (1515), 453–475.

Teka, A., Bairagi, S., Shahadat, M., Joshi, M., Ziauddin Ahammad, S. and Wazed Ali, S. (2018). "Poly(vinylidene fluoride) (PVDF)/potassium sodium niobate (KNN)-based nanofibrous web: A unique nanogenerator for renewable energy harvesting and investigating the role of KNN nanostructures." *Polym. Adv. Technol.*, 29 (9), 2537–2544.

Tian, R., Xu, Q., Lu, C., Duan, X. and Xiong, R.G. (2017). "Spontaneous polarization switching and piezoelectric enhancement of PVDF through strong hydrogen bonds induced by layered double hydroxides." *Chem. Commun.*, 53 (56), 7933–7936.

Tiwari, S., Gaur, A., Kumar, C. and Maiti, P. (2019). "Enhanced piezoelectric response in nanoclay induced electrospun PVDF nanofibers for energy harvesting." *Energy*, 171, 485–492.

Trolier-McKinstry, S., Zhang, S., Bell, A.J. and Tan, X. (2018). "High-Performance Piezoelectric Crystals, Ceramics, and Films." *Annu. Rev. Mater. Res.*, 48 (1), 191–217.

Ulaganathan, M. and Rajendran, S. (2010). "Preparation and characterizations of PVAc/P(VdF-HFP)-based polymer blend electrolytes." *Ionics (Kiel)*, 16 (6), 515–521.

Ünsal, Ö.F., Altın, Y. and Çelik Bedeloğlu, A. (2020). "Poly(vinylidene fluoride) nanofiber-based piezoelectric nanogenerators using reduced graphene oxide/polyaniline." *J. Appl. Polym. Sci.*, 137 (13), 1–14.

Wan, C. and Bowen, C.R. (2017). "Multiscale-structuring of polyvinylidene fluoride for energy harvesting: the impact of molecular-, micro- and macro-structure." *J. Mater. Chem. A*, 5 (7), 3091–3128.

Wang, D. yi, Leuteritz, A., Wagenknecht, U. and Heinrich, G. (2009). "Self-assembling organomodified Co/Al based layered double hydroxides (LDH) via one-step route." *Trans. Nonferrous Met. Soc. China (English Ed.)*, 19 (6), 1479–1482.

Wang, F., Mai, Y.W., Wang, D., Ding, R. and Shi, W. (2015). "High quality barium

titanate nanofibers for flexible piezoelectric device applications." *Sensors Actuators, A Phys.*, 233, 195–201.

Wang, W., Zhang, S., Srisombat, L., Lee, T.R. and Advincula, R.C. (2011). "Gold-Nanoparticle and Gold-Nanoshell-Induced Polymorphism in Poly(vinylidene fluoride)." *Macromol. Mater. Eng.*, 296 (2), 178–184.

Wu, C.M., Chou, M.H. and Zeng, W.Y. (2018). "Piezoelectric response of aligned electrospun polyvinylidene fluoride/carbon nanotube nanofibrous membranes." *Nanomaterials*, 8 (6), 1–13.

Xing, C., Guan, J., Li, Y. and Li, J. (2014). "Effect of a room-temperature ionic liquid on the structure and properties of electrospun poly(vinylidene fluoride) nanofibers." *ACS Appl. Mater. Interfaces*, 6 (6), 4447–4457.

Xu, Z.P. and Braterman, P.S. (2003). "High affinity of dodecylbenzene sulfonate for layered double hydroxide and resulting morphological changes." *J. Mater. Chem.*, 13 (2), 268–273.

Xue, W., Lv, C., Jing, Y., Chen, F. and Fu, Q. (2017). "Fabrication of electrospun PVDF nanofibers with higher content of polar  $\beta$  phase and smaller diameter by adding a small amount of dioctadecyl dimethyl ammonium chloride." *Chinese J. Polym. Sci.*, 35 (8), 992–1000.

Yan, J., Liu, M., Jeong, Y.G., Kang, W., Li, L., Zhao, Y., Deng, N., Cheng, B. and Yang, G. (2019). "Performance enhancements in poly(vinylidene fluoride)-based piezoelectric nanogenerators for efficient energy harvesting." *Nano Energy*, 56, 662–692.

Yang, L., Ji, H., Qiu, J., Zhu, K. and Shao, B. (2014). "Effect of temperature on the crystalline phase and dielectric and ferroelectric properties of poly(vinylidene fluoride) film." *J. Intell. Mater. Syst. Struct.*, 25 (7), 858–864.

Yang, Z., Zhou, S., Zu, J. and Inman, D. (2018). "High-Performance Piezoelectric Energy Harvesters and Their Applications." *Joule*, 2 (4), 642–697.

- Ye, H.-J., Shao, W.-Z. and Zhen, L. (2013). "Crystallization kinetics and phase transformation of poly(vinylidene fluoride) films incorporated with functionalized baTiO<sub>3</sub> nanoparticles." *J. Appl. Polym. Sci.*, 129 (5), 2940–2949.
- Yee, W.A., Kotaki, M., Liu, Y. and Lu, X. (2007). "Morphology, polymorphism behavior and molecular orientation of electrospun poly(vinylidene fluoride) fibers." *Polymer (Guildf)*., 48 (2), 512–521.
- Yu, H., Huang, T., Lu, M., Mao, M., Zhang, Q. and Wang, H. (2013). "Enhanced power output of an electrospun PVDF/MWCNTs-based nanogenerator by tuning its conductivity." *Nanotechnology*, 24 (40), 405401.
- Yu, S., Zheng, W., Yu, W., Zhang, Y., Jiang, Q. and Zhao, Z. (2009). "Formation Mechanism of  $\beta$ -Phase in PVDF/CNT Composite Prepared by the Sonication Method." *Macromolecules*, 42 (22), 8870–8874.
- Yuan, X., Zhang, Y., Dong, C. and Sheng, J. (2004). "Morphology of ultrafine polysulfone fibers prepared by electrospinning." *Polym. Int.*, 53 (11), 1704–1710.
- Yun, J.S., Park, C.K., Jeong, Y.H., Cho, J.H., Paik, J.H., Yoon, S.H. and Hwang, K.R. (2016). "The fabrication and characterization of piezoelectric PZT/PVDF electrospun nanofiber composites." *Nanomater. Nanotechnol.*, 6 (1), 1–5.
- Zaarour, B., Zhu, L., Huang, C. and Jin, X. (2018). "Controlling the Secondary Surface Morphology of Electrospun PVDF Nanofibers by Regulating the Solvent and Relative Humidity." *Nanoscale Res. Lett.*, 13 (1), 1–11.
- Zhang, B., Chen, Y., Liu, G., Xu, L.Q., Chen, J., Zhu, C.X., Neoh, K.G. and Kang, E.T. (2012). "Push-Pull archetype of reduced graphene oxide functionalized with polyfluorene for nonvolatile rewritable memory." *J. Polym. Sci. Part A Polym. Chem.*, 50 (2), 378–387.
- Zhang, C., Yuan, X., Wu, L., Han, Y. and Sheng, J. (2005). "Study on morphology of electrospun poly(vinyl alcohol) mats." *Eur. Polym. J.*, 41 (3), 423–432.
- Zhang, H., Zhu, Y. and Li, L. (2020). "Fabrication of PVDF/graphene composites

with enhanced  $\beta$  phase: Via conventional melt processing assisted by solid state shear milling technology." *RSC Adv.*, 10 (6), 3391–3401.

Zhao, X., Zhang, Q., Chen, D. and Lu, P. (2010). "Enhanced mechanical properties of graphene-based polyvinyl alcohol composites." *Macromolecules*, 43 (5), 2357–2363.

Zhao, Y., Fan, H., Ren, X., Long, C., Liu, G. and Liu, Z. (2016). "Lead-free  $\text{Bi}_{5-x}\text{La}_x\text{Ti}_3\text{FeO}_{15}$  ( $x=0,1$ ) nanofibers toward wool keratin-based biocompatible piezoelectric nanogenerators." *J. Mater. Chem. C*, 4 (30), 7324–7331.

Zheng, J., He, A., Li, J. and Han, C.C. (2007). "Polymorphism control of poly(vinylidene fluoride) through electrospinning." *Macromol. Rapid Commun.*, 28 (22), 2159–2162.

Zi, Y. and Wang, Z.L. (2017). "Nanogenerators: An emerging technology towards nanoenergy." *APL Mater.*, 5 (7), 074103 .

Zong, X., Kim, K., Fang, D., Ran, S., Hsiao, B.S. and Chu, B. (2002). "Structure and process relationship of electrospun bioabsorbable nanofiber membranes." *Polymer (Guildf.)*, 43 (16), 4403–4412.

Zuo, W., Zhu, M., Yang, W., Yu, H., Chen, Y. and Zhang, Y. (2005). "Experimental study on relationship between jet instability and formation of beaded fibers during electrospinning." *Polym. Eng. Sci.*, 45 (5), 704–709.

## BIO-DATA

---

### SAWAN SHETTY

*Permanent address:*

3-64/3, OMKARA,  
Manjalike, Alape, Padil  
Mangaluru-575007  
Karnataka, INDIA.



*Contact Details:*

Email ✉: [sawanshetty@gmail.com](mailto:sawanshetty@gmail.com)

Phone : +91-8951036626

*Academic Qualifications:*

Master of Technology in Manufacturing Engineering from Manipal Institute of Technology (Manipal Academy of Higher Education (Deemed university)), Manipal, Karnataka, India.

Bachelor of Engineering in Mechanical Engineering from Manipal Institute of Technology (Manipal Academy of Higher Education (Deemed university)), Manipal, Karnataka, India.

*Research publications:*

Articles in International Journals: 03

Articles in Conference Proceedings: 02

Chapters in Book: 01





### ***List of publications based on Ph.D Research Work***

#### ***In peer-reviewed journals:***

- Shetty, S., Ekbote, G.S., Mahendran, A. and Anandhan, S. (2019). "Polymorphism, dielectric and piezoelectric response of organo-modified Ni-Co layered double hydroxide nanosheets dispersed electrospun PVDF nanofabrics." *J. Mater. Sci. Mater. Electron.*, 30 (23), 20703–20715.
- Shetty, S., Mahendran, A. and Anandhan, S. (2020). "Development of a new flexible nanogenerator from electrospun nanofabric based on PVDF/talc nanosheet composites." *Soft Matter*, 16 (24), 5679–5688.
- Shetty, S., Shanmugaraj, A., and Anandhan, S. (2021). "Physico-chemical and piezoelectric characterization of electroactive nanofabrics based on functionalized graphene/talc nanolayers/PVDF for energy harvesting." *J. Polym. Res.*, 28, 419.
- Shetty, S., Murugesan, S., Salehi, S., Pellert, A., Scheibel, M., Scheibel, T., and Anandhan, S. "Evaluation of piezoelectric behavior and biocompatibility of PVDF ultrafine fibers with incorporated talc nanosheets." *ACS Applied Biomaterials (in review)*.

#### ***In conference proceedings:***

- Shetty, S., Ekbote, G.S., Mahendran, A. and Anandhan, S. (2019). "Enhanced electro-active phase content and piezoelectric response of electrospun Ni-Co Layered double hydroxide/poly(vinylidene fluoride) (PVDF) nanocomposite non-woven webs", *International Conference on 'Advancements in Polymeric Materials APM-2019', CIPET-Chennai, India*.
- Shetty, S., Mahendran, A. and Anandhan, S. (2019). "Promotion of electroactive crystalline phase in talc/ poly(vinylidene fluoride) (PVDF) based nanofibrous webs", *International Conference on Advances in Polymeric Materials & Human Healthcare, Goa, India*.

Book chapter

- Shetty, S., and Anandhan, S. (2021). "Electrospun PVDF based composite nanofabrics : An emerging trend towards energy harvesting", Ch. 10, in '*Nano Tools & Devices for Enhanced Renewable Energy*', ISBN: 9780128217092, S. Devasahayam, C. Hussain, Eds., *Elsevier*, UK, 2021, DOI: 10.1016/B978-0-12-821709-2.

: